

2015-09-24

Sensor Error Analysis of Superconductive Angular Gradiometer

Mokhtari, Elaheh

Mokhtari, E. (2015). Sensor Error Analysis of Superconductive Angular Gradiometer (Doctoral thesis, University of Calgary, Calgary, Canada). Retrieved from <https://prism.ucalgary.ca>. doi:10.11575/PRISM/27755
<http://hdl.handle.net/11023/2493>

Downloaded from PRISM Repository, University of Calgary

UNIVERSITY OF CALGARY

Sensor Error Analysis of Superconductive Angular Gradiometer

by

Elaheh Mokhtari

A THESIS

SUBMITTED TO THE FACULTY OF GRADUATE STUDIES
IN PARTIAL FULFILMENT OF THE REQUIREMENTS FOR THE
DEGREE OF DOCTOR OF PHILOSOPHY

GRADUATE PROGRAM IN GEOMATICS ENGINEERING

CALGARY, ALBERTA

SEPTEMBER, 2015

© Elaheh Mokhtari 2015

Abstract

A superconductive angular gradiometer is a pair of superconductive angular accelerometers that pivot about a common axis. The output of the sensor corresponds to gradients. The gradients are effective not only in explorations of ore bodies and oil fields, but also in a complete modeling of the gravity field of the Earth. The superconductive angular gradiometer typically carries by a mobile platform to collect the measurements. Therefore, the instrument senses not only gravity gradients, but also various effects of an accelerated coordinate frame (introducing errors). The errors in the gradiometer channel are technically removed through some electrical, mechanical, and empirical approaches. A major effort in this study is given to an efficient and a cost effective post processing approach to deal with only the effect of angular velocities squared.

A superconductive angular accelerometer is an important sensor that often supplements a mobile superconductive angular gradiometer during data acquisition operations. While the angular accelerations are measured, the angular velocities squared are computed by integration. However, the angular accelerations are noisy because of translational accelerations of the platform and temperature fluctuations of the environment during the operation. Wavelet de-noising and de-trending techniques have been implemented in order to mitigate these errors. The results indicate that more than 66% of the noise level was efficiently reduced in comparison to the empirical approach by the company for the static x angular accelerations. This improvement was achieved without knowledge of the temperature and other error effects.

Furthermore, the effect of angular velocities squared, which is about -20 Eötvös, is removed from the gradiometer output. Then, the performance of the gradiometer is evaluated through a simulation study by error propagation in a single-input-single-output system. The standard deviations of the static x angular acceleration, y angular acceleration, and differential mode after the wavelet analysis are $3.08e-05 \text{ rad/s}^2$, $3.55e-05 \text{ rad/s}^2$, and $3.21e-08 \text{ rad/s}^2$, respectively. So, the the final accuracy of the true gradient in this research work is 0.06 Eötvös, which makes the system suitable for variety exploration applications that require the gradients to be known with an accuracy of 1 Eötvös or better.

Acknowledgements

I'm so glad that finally I could find a time to express my gratitude to whom their support, guidance, and encouragement made a lot of contribution to this thesis.

I would like to thank my supervisor Dr. M. G. Sideris, for his guidance and constructive criticisms in the course of my research. His remarkable patience and knowledge while answering my questions is appreciated, which helped me to see the BIG PICTURE. Many thanks to Dr. M. Elhabiby for his vision and ideas during this challenging period.

I wish to extend my appreciation to one of my supervisory committee members Dr. N. El-Sheimy for being supportive during the defense oral exam.

I am thankful to my internal examiner, Dr. L. Lines, for him staying positive and energetic during the exam, which made me to feel more confident while answering the questions.

I wish to thank my external examiner, Dr. J. Skaloud, for adding bandpass filtering to my thesis work, which I really gained a useful experience with this extra work.

I also would like to thank all the faculty and staff members of the Geomatics Department, particularly J. A. Yeung, M. Freeman, and C. Canivet for being such a great asset in creating a helpful and friendly educational environment during these years.

Thanks to Gedex Company for providing data and information for this research work.

I am deeply grateful to Dr. A. Mohamed Moussa for his continuous support and his stimulating suggestions in many aspect of my thesis. Mainly, he helped me overcome some major obstacles during the preparation of Chapter 4. Words simply fail to express how thankful I am for him being available all the time to come to my office and discuss a thousand questions with me.

I wish to thank R. K. Harvey who did proof reading of my thesis. Special thanks to both IT support technologist J. Lin and R. K. Harvey for saving my time and my computer during the last year.

Special thanks to Dr. R. Tarani, my psychiatrist, for her continuous support and guidance. She helped me to manage my stress and to improve my communication skills with my supervisor during the last year of my thesis work.

I am thankful to my friends: D. Piretzidis, M. Abdizadeh, and A. Shafaati who helped me to improve my knowledge in programming and signal processing.

Many many thanks to my friends, to name a few, M. Amini, H. Alemasoom, V. S. Nasrabadi, who were really really there for me and supported me during the different stages of this program.

Last but not least, I would like to express my appreciation to my family, particularly my mom and my sister. Thank you so much for having faith in me, and for your unconditional love and support during the last four years, which helped me to fulfill my dreams.

To my parents:

Khadijeh & Hojjat

To my sister:

Samaneh

Table of Contents

Abstract	ii
Acknowledgements	iii
List of Tables	ix
List of Figures and Illustrations	xii
List of Abbreviations	xviii
CHAPTER 1: INTRODUCTION.....	1
1.1 Background and problem statement	1
1.2 Thesis objectives.....	6
1.3 Thesis outline.....	7
CHAPTER 2: PRINCIPLES AND SYSTEMS OF AIRBORNE GRAVITY GRADIOMETRY	9
2.1 Theoretical background	10
2.1.1 Gravity gradients	10
2.1.2 Force and torque experienced by a test mass in a gravity field (stationary operation)	12
2.1.3 Force and torque experienced by a test mass in a gravity field (dynamic operation)	15
2.2 Principles of different types of accelerometers and gradiometers	18
2.2.1 Principle of superconductive translational accelerometers	18
2.2.2 Principle of superconductive angular accelerometers	20
2.2.3 Principle of specific force gravity gradiometers	22
2.2.4 Principle of torque gravity gradiometers	23
2.3 OQR type superconducting gravity gradiometer	24
2.3.1 Principle and measurement of OQR type superconducting gravity gradiometer	25
2.3.2 Errors in the output of OQR type superconducting gravity gradiometer	27
2.3.3 Configuration of OQR type superconductive gravity gradiometer in a moving platform.....	30
2.4 Review of current industrial airborne gravity gradiometer systems.....	31
2.4.1 Falcon® Airborne Gravity Gradiometer	31
2.4.2 Air-FTG airborne gravity gradiometer	31
2.4.3 The University of Western Australia Superconductive Gravity Gradiometer (UWA-SGG).....	33
2.4.4 The Gedex High-Definition Airborne Gravity Gradiometer (Gedex HD-AGG™)	34
2.5 Summary.....	34
CHAPTER 3: GEDEX HIGH-DEFINITION AIRBORNE GRAVITY GRADIOMETER (GEDEX HD-AGG™).....	35
3.1 Working principle of the Gedex HD-AGG™	35
3.1.1 Gedex HD-AGG™ configuration with auxiliary sensors	39
3.1.2 Reference frames used in the Gedex system	40

3.2	OQR measurements in the Gedex system.....	42
3.2.1	Measurement of a single superconductive angular accelerometer	42
3.2.2	Measurements of a pair of superconductive angular accelerometers	43
3.3	Noise terms definition in the Gedex HD-AGG™ system	46
3.4	Noise terms definition in the superconductive translational accelerometer	47
3.5	Noise terms definition in the superconductive angular accelerometer	50
3.6	Empirical approaches to remove the errors in the superconductive translational and angular accelerometers.....	53
3.7	Summary	60
CHAPTER 4: ERROR ANALYSIS OF SUPERCONDUCTIVE ANGULAR ACCELEROMETER AND SUPERCONDUCTIVE ANGULAR GRADIOMETER DATA USING STATIC OBSERVATIONS.....		61
4.1	Data set available for this research	61
4.2	Removing outliers from observations using 3σ rule	62
4.3	Wavelet de-noising of x angular acceleration.....	63
4.3.1	Wavelet base function	64
4.3.2	Optimization criterion	65
4.3.3	Thresholding procedure.....	65
4.3.4	Level of decomposition.....	69
4.3.5	Results of de-noising: first approach	71
4.3.6	Results of de-noising: second approach.....	75
4.3.7	Results of de-noising: third approach	78
4.4	Butterworth and Wiener low pass filtering results	78
4.5	Wavelet de-trending and de-noising of x angular acceleration	80
4.6	Wavelet de-trending and de-noising of x angular acceleration in comparison to empirical linear regression approach	83
4.7	Wavelet de-trending and de-noising of y angular acceleration	86
4.8	Wavelet de-trending and de-noising of raw gradient.....	88
4.9	Summary	90
CHAPTER 5: QUALITY ASSESSMENT OF THE GRADIOMETER OUTPUT		93
5.1	Removing angular velocities squared from angular gradiometer measurements ..	93
5.2	Performance of the superconductive angular gradiometer	100
5.2.1	Simulating the true gradient.....	103
5.2.2	Error propagation in a single-input, single-output system of the gradiometer channel	107
5.3	Summary.....	113
CHAPTER 6: CONCLUSIONS AND RECOMMENDATIONS.....		114
6.1	Conclusions.....	114
6.2	Recommendations.....	117
REFERENCES.....		119

APPENDIX A: AN INTRODUCTION TO WAVELET ANALYSIS AND WIENER

LOW PASS FILTERING127

- A.1 Wavelet spectral analysis128
 - A.1.1 Wavelets properties128
 - A.1.2 Continuous Wavelet Transform (CWT).....130
 - A.1.3 Discrete Wavelet Transform (DWT).....133
 - A.1.4 Multiresolution analysis (MRA).....134
- A.2 Wavelet de-noising137
 - A.2.1 Soft or hard thresholding ($\delta\lambda()$).....138
 - A.2.2 Noise estimation procedure (σ^{\wedge}).....140
 - A.2.3 Threshold selection rules (λ)141
- A.3 Wavelet de-trending143
- A.4 Wiener low pass filtering144

APPENDIX B: BANDPASS FILTERING OF X ANGULAR ACCELERATION.....

.....147

- B.1 Bandpass filtering.....147
 - B. 1. 1 Bandpass filtering of x angular acceleration using window design functions..
.....150
 - B. 1. 2 Bandpass filtering of x angular acceleration using minimum least-squares error
criterion153

List of Tables

Table 1-1: Typical wavelengths and amplitude in salt domes and ore bodies' explorations plus required sampling rate and measuring accuracy of a gradiometer system for detecting these structures (Schwarz and Vassiliou 1986)	2
Table 1-2: Error contribution to the output of the superconductive angular gradiometer on a mobile platform (Moody 2011).....	4
Table 1-3: Major thesis objectives covered in each chapter	8
Table 2-1: Data processing of Air-FTG data	33
Table 2-2: Dynamic error contributions to the gradient sensitivity in the OQR for responder A (Matthews 2002)	34
Table 3-1: Four major sensors used in the Gedex multiple linear regression approach	54
Table 3-2: Regression coefficients estimated as a result of multiple linear regression with filtered measurements	57
Table 4-1: List of data available for this research for both dynamic and static system operation	62
Table 4-2: Various wavelets used in this chapter	64
Table 4-3: Threshold magnitudes computed by four different threshold estimators considering the unit noise and white noise assumptions	66
Table 4-4: Threshold magnitudes computed by four different threshold estimators with the non-white noise assumption.....	66
Table 4-5: Selected wavelet families that generated the minimum RMS result by rescaling the detail coefficients with global thresholding scheme (de-noising first approach)	71
Table 4-6: Selected wavelet families that generated the minimum RMS results by rescaling the detail coefficients with level-dependent thresholding scheme (de-noising first approach)..	73
Table 4-7: Selected wavelet families that generated the minimum RMS results with global threshold rescaling (de-noising second approach)	75
Table 4-8: Selected wavelet families that generated the minimum RMS results with level-dependent threshold rescaling (de-noising second approach).....	76
Table 4-9: Selected wavelet families that generate the minimum RMS results reconstructed with only approximation coefficients at the 7 th LOD	78

Table 4-10: Wavelet candidates that produce the best trends for the x angular acceleration	81
Table 4-11: Selected wavelet families that generate the minimum RMS results for the x angular acceleration (Results for the de-trending approach at the 8 th LOD)	81
Table 4-12: Selected wavelet families that generate the minimum RMS results for the x angular acceleration (Results for de-trending approach at the 9 th and the 10 th LODs).....	83
Table 4-13: Wavelet candidates that produce the best trends for the y angular acceleration	86
Table 4-14: Selected wavelet families that generate the minimum RMS results for the y angular acceleration	87
Table 4-15: Wavelet candidates that produces the best trends in gradiometer channel	88
Table 4-16: Selected wavelet families that generate the minimum RMS results for the gradient measurement	89
Table 4-17: The RMS value achieved by wavelet de-noising of the x angular acceleration with the Coif5 wavelet and the Minimax threshold estimator in comparison to the RMS value achieved by the Wiener and Butterworth low pass filtering methods	91
Table 4-18: Filtering approaches that produced the minimum RMS results for the differential mode, x and y angular accelerations	92
Table 5-1: Noise colors (Carter 2008)	101
Table 5-2: Mean and standard deviation of the x and y angular accelerations Ω_x , Ω_y and differential mode observation dm from the static data before and after wavelet filtering .	104
Table 5-3: Different Sds for creating different realizations (<i>rad/s²</i>)	104
Table 5-4: Accuracy of the filtered simulated true gradient with equal weight noise assumption	109
Table 5-5: Accuracy of the filtered simulated true gradient when the noise Sd of the differential mode is smaller than angular accelerations.....	110
Table 5-6: Accuracy of the filtered simulated true gradient when the noise Sd of the differential mode is bigger than angular accelerations	111
Table A-1: Wavelet families and their properties (Misiti et al., 2014).....	130
Table A-2: Pseudo frequencies associated with each decomposition level at 195.32 Hz sampling rate computed with Coif5 wavelet	135
Table B-1: Comparison of bandpass FIR filtering methods, bandpass IIR filtering, and wavelet de-trending and de-noising applied to the x angular acceleration. The bandpass of interest is 0.53 to 1.01 Hz	151

Table B-2: The RMS values achieved for the x angular acceleration after applying the least-squared bandpass filtering of order 900	153
--	-----

List of Figures and Illustrations

Figure 2-1: Some of the components of the gravity gradient tensor in Eötvös calculated for a 100 tonne spherical mass of radius 2 m, density contrast 1500 kg/m ³ and depth of 1000 m	11
Figure 2-2: Torque and force experience by a test mass	12
Figure 2-3: A mass body with density ρr in a gravity field of the Earth in a Cartesian coordinate frame	14
Figure 2-4: Superconducting translational accelerometer sensing circuit (Moody and Paik 2004)	19
Figure 2-5: Mechanical component of the superconductive translational accelerometer (Moody and Paik 2004)	19
Figure 2-6: Superconductive angular accelerometer sensing circuit (Moody 2011).....	20
Figure 2-7: Mechanical component of the superconductive angular accelerometer (Moody 2011)	21
Figure 2-8: Principle of specific force measurement gradiometer.....	22
Figure 2-9: Principle of torque measurement gradiometer	24
Figure 2-10: Basic structure of the OQR type superconductive angular gradiometer (Provided by Gedex).....	25
Figure 2-11: Schematic circuit for a pair of coupled superconductive angular accelerometers (Moody and Paik 2007)	26
Figure 2-12: Bar distortion (induced dipole) (Matthews 2002).....	28
Figure 2-13: Pivot distortion (mass dipole) (Matthews 2002).....	29
Figure 2-14: Three-axis superconductive angular gradiometer inside the SQUID holder plus superconductive translational and angular accelerometers (Moody 2011).....	30
Figure 2-15: Air-FTG instrument (Murphy 2004).....	32
Figure 3-1: General principle of the Gedex HD-AGG TM instrument: (a) differential mode acceleration and (b) common mode acceleration (Matthews 2002)	36
Figure 3-2: Configuration of the Gedex HD-AGG TM with superconductive translational and angular accelerometers (Carroll et al., 2010a)	36

Figure 3-3: The Gedex HD-AGG TM measurements in practice.....	38
Figure 3-4: Major components of the Gedex HD-AGG TM . (a) Motion isolation instrument plus the cryostat. (b) Inertial instruments including Applanix IMU and Qflex accelerometers on the top of the instrument. (c) Gedex HD-AGG TM cube configuration with inertial instruments on the top (provided by Gedex).....	40
Figure 3-5: Different reference frames used in the Gedex system	41
Figure 3-6: A single superconductive angular accelerometer in standard and principal axes views	42
Figure 3-7: A coupled superconductive angular accelerometers (x-axis OQR).....	43
Figure 3-8: Configuration of the x-axis OQR gradiometer with its coupled z-axis angular accelerometers.....	45
Figure 3-9: Gedex superconductive translational accelerometer output.....	48
Figure 3-10: Gedex superconductive angular accelerometer output	51
Figure 3-11: Raw (red line) and filtered (blue line) temperature data in K along with their PSD (Provided by Gedex).....	55
Figure 3-12: Raw (red line) and filtered (blue line) x, y, and z translational accelerations from Qflex accelerometer along with their PSD (Provided by Gedex).....	55
Figure 3-13: Raw x angular velocity from Applanix solution and derived x angular acceleration using spline derivative function (Provided by Gedex)	56
Figure 3-14: Raw (red line) and filtered (blue line) x angular acceleration derived from the Applanix solution along with its PSD (Provided by Gedex)	56
Figure 3-15: Raw (red line) and filtered (blue line) x angular acceleration from the superconductive angular accelerometer along with its PSD (Provided by Gedex)	57
Figure 3-16: The top figure is raw angular acceleration (red line) and detected low frequency error (green line). The bottom figure is angular acceleration after removing the low frequency error (Provided by Gedex)	58
Figure 3-17: Raw (red line) and corrected (blue line) x angular acceleration in comparison to filtered Applanix derived x angular accelerations (green line) both in time domain (top plot) and frequency domain (bottom plot) (Provided by Gedex)	59
Figure 4-1: Differential mode (raw angular gradiometer output), x and y angular accelerations before removing the outliers (blue line) and after removing the outliers (red line) (all data from static run of the system)	63

Figure 4-2: Noise level calculated for x and y angular acceleration based on the robust median absolute deviation and rescaled noise level from the first LOD by the $1f2$ rule	67
Figure 4-3: Noise level calculated for differential mode observation based on the robust median absolute deviation and rescaled noise level from the first LOD by the $1f2$ rule	68
Figure 4-4: Variation of energy for original and shrunk coefficients (Coif5 with Minimax threshold estimator)	70
Figure 4-5: Original (red line) and de-noised (green line) signals along with their original and shrunk coefficients. Computed with the Bior1.1 wavelet and global thresholding scheme (de-noising first approach)	72
Figure 4-6: Reconstructed signal rad/s^2 with original detail coefficients (blue line) and modified details (red line) using Bior1.1 wavelet from the 1 st to the 8 th LOD. Coefficients have been shrunk with the Median threshold and the white noise assumption	73
Figure 4-7: Original (red line) and de-noised (green line) signals with shrunk coefficients. Computed with the Coif3 wavelet and the level-dependent thresholding scheme (de-noising first approach)	74
Figure 4-8: Reconstructed signal rad/s^2 with original detail coefficients (blue line) and modified details (red line) using the Coif3 wavelet from the 1 st to the 8 th LOD. Coefficients have been shrunk with the Median threshold estimator and the non-white noise assumption	74
Figure 4-9: Original (red line) and de-noised (green line) signals with shrunk coefficients. Computed with Coif5 and level-dependent thresholding scheme (de-noising second approach)	77
Figure 4-10: (A) Reconstructed signal with the original approximation coefficient at the 7 th LOD. (B) Reconstructed signal (non-white noise assumption) with the original detail coefficient (blue line) and modified detail coefficient with the Minimax threshold (red line) at 7 th LOD. (C) Reconstructed signal (white noise assumption) with original detail coefficient (blue line) and modified detail coefficient with the Median threshold (red line) at 7 th LOD. The Coif5 wavelet was used in all reconstruction	77
Figure 4-11: Wiener filter's frequency response (calculated for x angular acceleration)	79
Figure 4-12: Comparison between the de-noised x angular acceleration with the frequency domain filters: Butterworth and Wiener	80
Figure 4-13: De-trended and de-noised x angular acceleration in comparison to the de-noised and raw signals	82
Figure 4-14: Trend computed as a result of linear regression in comparison to the trend computed by wavelet (approximation at 8 th LOD with Coif5)	84

Figure 4-15: The x angular acceleration after applying the linear regression and Butterworth low pass filtering (blue line) in comparison to the signal after wavelet de-trending and de-noising with Bior1.3 wavelet (green line).....	85
Figure 4-16: The y angular acceleration (blue line), detected trend (red line), and the de-noised and de-trended signal (green line) in rad/s^2 along with their PSDs (bottom plot) in $db...$	87
Figure 4-17: The raw differential mode (blue line), detected trend (red line), and the de-noised and de-trended signal (green line) in rad/s^2 along with their PSDs (bottom plot) in $db...$	89
Figure 5-1: Configuration of the z-axis OQR gradiometer with its coupled z-axis angular accelerometers.....	94
Figure 5-2: A three-input, single-output system with noises for the OQR type gradiometer.....	95
Figure 5-3: Raw and filtered x angular accelerations along with their PSDs using dynamic data	96
Figure 5-4: Raw and filtered y angular accelerations along with their PSDs using dynamic data	97
Figure 5-5: X angular velocities squared derived from raw and filtered angular accelerations ...	97
Figure 5-6: Y angular velocities squared derived from raw and filtered angular accelerations ...	98
Figure 5-7: Raw gradient, raw gradient after removing the angular velocities squared derived from raw data, raw gradient after removing the angular velocities squared derived from filtered data in time and frequency domains.....	99
Figure 5-8: True gradient after removing both the angular velocities squared and the rest of the errors by the wavelet filtering in time and frequency domains.....	99
Figure 5-9: PSD of the different kinds of noise.....	102
Figure 5-10: PSD of the raw differential mode and the raw y angular accelerations after de-trending along with the PSD of the different noise types (white noise (gray line), pink noise (pink line), and red noise (red line)).....	102
Figure 5-11: Simulated true gradient with equal standard deviation assumption (white noise assumption). Sd of all terms in rad/s^2 : (A) $3e-01$, (B) $3e-03$, (C) $3e-06$, and (D) $3e-09$.	105
Figure 5-12: Simulated true gradient with equal standard deviation assumption (red noise assumption). Sd of all terms in rad/s^2 : (A) $3e-01$, (B) $3e-03$, (C) $3e-06$, and (D) $3e-09$.	106
Figure 5-13: Simulated true gradient with the second noise assumption (pink noise assumption). Sd of the accelerations in all cases is $3e-3 rad/s^2$. Sd of the differential mode in rad/s^2 : (A) $3e-5$, (B) $3e-6$, (C) $3e-7$, and (D) $3e-8$	106

Figure 5-14: Simulated true gradient with the third noise assumption. Sd of the differntial mode in all cases is $3e-3 \text{ rad/s}^2$. Sd of the angular acceleration is $3e-5$ in rad/s^2 . The noise type: (A) white (B) pink, and (C) red	107
Figure 5-15: Propagation of error in a single-input, single-output system in gradiometer channel	108
Figure 5-16: True gradient in comparison to estimated true gradeint when the Sd of the observations and the Sd of the filtered observations are used to calculate the accuracy of the system output. Left plots: the accuracy of the system output is 10.47 Eötvös. The right plots: the accuracy of the system output is 0.06 Eötvös	112
Figure A-1: Mean and variance of x angular acceleration (static data set)	129
Figure A-2: Different kind of mother wavelets	129
Figure A-3: Energy variation of the x angular acceleration as a function of scale in power of rad/s^2 using Db8 wavelet base function from 1 to 60 scales	132
Figure A-4: The contour plot of the scalogram for x angular accelerations (using Coif5 as a wavelet base function)	133
Figure A-5: A two-level decomposition of the signal as a wavelet tree	135
Figure A-6: Reconstructed x angular acceleration with detail and approximation coefficients with Coif5 wavelet from the 1 st to the 8 th LOD	136
Figure A-7: Detail coefficient at the 5 th LOD computed by Coif5 wavelet for the x angular acceleration (threshold magnitude is depicted with red line)	139
Figure A-8: Detail coefficients at the 5 th LOD after applying hard and soft thresholding on the x angular acceleration	139
Figure A-9: The x and y angular accelerations in time and frequency domains	141
Figure A-10: Thresholds magnitudes computed by four different threshold estimators: Median (green line), Minimax (black line) and both SURE and Heuristic (red line).....	142
Figure A-11: Different trends computed for the x angular acceleration at the 8 th , 9 th , and 10 th LODs with Coif5 wavelet	144
Figure A-12: Principle of Wiener filtering	144
Figure B-1: Basic structure of a bandpass filter.....	148
Figure B-2: Frequency responses of a low pass filter showing good and poor filter parameters (Smith 1999)	149

Figure B-3: Frequency response of an FIR bandpass filter with four popular windowing functions in comparison to the frequency response of an IIR Butterworth bandpass filter	150
Figure B-4: PSDs of the raw and filtered x angular acceleration after wavelet, Butterworth, and Bartlett filtering methods	152
Figure B-5: PSDs of the raw and filtered x angular acceleration after Blackman, Hamming, and Han filtering methods.....	152
Figure B-6: Worst (blue line) and best (green line) frequency responses of the bandpass least-squares.....	154
Figure B-7: PSDs of the best case (bottom plot) and worst case (top plot) results for the least-squares bandpass filtering	155

List of Abbreviations

Symbol	Definition
Bior	Biorthogonal
Coif	Coiflet
CMRR	Common mode rejection ratio
Db	Daubechy
dm	Differential mode
FIR	Finite Impulse Response
FTG	Full Gradient Tensor
GGI	Gravity Gradient Instruments
GPS	Global Positioning System
HD-AGG	High-Definition Airborne Gravity Gradiometer
IIR	Infinite Impulse Response
LARR	Linear Acceleration Rejection Ratio
LOD	Level of Decomposition
MRA	Multiresolution Analysis
OQR	Orthogonal Quadrupole Responder
PSD	Power Spectral Density
RMS	Root Mean Squared
Sd	Standard deviation
SQUID	Superconducting Quantum Interference Device
Sym	Symlet
UWA	University of Western Australia
w.r.t	With respect to

Chapter 1: Introduction

1.1 Background and problem statement

Gravity accelerations and gradient components are measured by gravimeters and gravity gradiometers, respectively. Both gravimeters and gradiometers use accelerometers for taking measurements: one accelerometer for gravimeters and two accelerometers for gradiometers. Both systems can provide valuable information regarding the near surface density fluctuations, though gravity gradiometers are able to give shorter wavelength information about the gravity field of the Earth in comparison to gravimeters (Dransfield 2007). Additionally, they provide good images of north-south and east-west edges of the geological target (Murphy 2004). The major advantage of gradiometry in comparison to gravimetry is providing redundant information, which can enhance the signal to noise ratio of interest. However, since gravity gradient field power is reduced rapidly with cubic distance from the target anomaly, the signals produced with gradiometers are less sensitive to detect objects deeper than 3000m (Biegert et al., 2001, Lumley et al., 2004). Gravity gradient along with gravity accelerations can increase our confidence regarding the exploration decisions (Murphy 2004, Lumley et al., 2004). Both systems have a variety of applications in geodesy and geophysics. For example, in geodesy this data can be used for determination of Earth models, geoid determination, and determination of heights by using GPS and precise geoid data (Hein 1995). And in geophysics, they can contribute to discovering many mineral deposits such as coal, base metals in iron-oxide-copper-gold deposits, porphyries, Broken-Hill type deposits and volcanogenic massive sulphides, iron in massive haematite, nickel sulphides and gold. They are very affective in the search for oil and gas, as well (Dransfield 2007).

Typical wavelengths and amplitudes in mapping salt dome, for oil exploration, and ore bodies are given in Table 1-1. The required sampling rate and measuring accuracy of a gradiometer system is mentioned in this table, as well.

Table 1-1: Typical wavelengths and amplitude in salt domes and ore bodies' explorations plus required sampling rate and measuring accuracy of a gradiometer system for detecting these structures (Schwarz and Vassiliou 1986)

Structure	Wavelength (km)	Amplitude (Eötvös)	Sampling Rate	Measuring Accuracy (Eötvös)
Salt domes	3-10	5-30	(300-1500 m) or (6-30 s)	4-7
Ore bodies	0.3-0.5	0.5-100	(100-500 m) or (2-10 s)	0.3-0.5

Measuring the short wavelengths of gravity field of the Earth was traditionally carried out by terrestrial gravimetry. It was taken point by point, which was a tedious task especially in remote areas such as mountains and oceans. There was an economic, accurate and efficient method which could help filling the gaps in the knowledge of the Earth gravity field in terrestrial gravimetry. In this method, the gravimeter was carried by a moving platform such as an airplane to take the measurements. This technique was also generalized to gradiometry case when airborne gradiometry was invented. A major concern in both airborne systems is the equivalence principle that makes it hard to identify the gravity accelerations and gravity gradient components from the translational and angular accelerations of the platform. One way to reject these unwanted accelerations, which are called common mode accelerations, was to measure the platform accelerations during the operation. In case of airborne gravimetry, it can be measured by a GPS sensor, which has its own limitations in accuracy. Since airborne gravimetry is not a major topic of this thesis, time will not be spent explaining the problems associated with it. Interested readers are directed to Schwarz and Li (1996), Li (2000), and Bruton (2000). In airborne gradiometry, the major focus of this research, since the instrument consists of pairs of accelerometers and the output measurement is determined from the difference between the outputs of each accelerometer, some parts of the platform accelerations will be automatically removed from the measurements. Thus, separation of the gravity signal from inertial effects can be achieved efficiently. However, there will still be some remaining noise, which needs to be modeled and removed from the gradiometer output. Similarly to airborne gravimetry, one way to eliminate the residual effects of noise in airborne gradiometry is by measuring the dynamics of the flight during the operation with the help of some auxiliary sensors, such as translational and angular accelerometers.

A special case of the gravity gradiometer was invented around 1900, and development was continued into torsion balanced gradiometers around 1940. Other systems have been developed since 1970 (Torge 1989). Different types of accelerometers can provide different kinds of gradiometers. Two types of accelerometers are common in literature: translational accelerometers and angular accelerometers. The former measures specific force (deriving translational accelerations in m/s^2) and the latter measures torque (deriving angular accelerations in rad/s^2). A pair of translational accelerometers make a force gradiometer while a pair of angular accelerometers make a torque gradiometer (Matthews 2002).

This thesis involved a specific kind of torque gradiometer that consists of two superconductive angular accelerometers pivoting about a common axis. This instrument has the basic design structure of an orthogonal quadrupole responder (OQR) that was developed by Dr. Frank van Kann around 1900 to measure off-diagonal components of the gradient tensor (Moody and Paik 2007). This gradiometer takes advantage of the superconductive material used in its design because the superconductive materials lose their electrical resistance at very low temperatures (5k to 9k) and become perfect conductors. In this state they can provide better instrument sensitivity, scale factor stability, and common mode rejection (Paik et al., 1997, Chan and Paik 1987). The target resolution for a superconductive angular gradiometer is at 1 Eötvös at 1 sample per second in airborne applications (Tryggvason et al., 2004). This OQR type gradiometer has been extensively studied and analyzed at the University of Western Australia (UWA) by Matthews (2000) (see also Anstie et al., (2010)). The Gedex High Definition Airborne Gravity Gradiometer (Gedex HD-AGGTM), which is the subject of this thesis, uses the same instrument. However, both groups (UWA and Gedex) are trying to come up with their own solutions for meeting the specified claimed resolution.

The OQR target resolution is affected by many errors. These errors can be divided into three major groups: the first group is related to inherent noise of the instrument, the second group is related to the operation of the instrument in a dynamic condition, and the third one is the effect of nonlinearities on the gradiometer output (Matthews 2002). The inherent noise of the instrument depends on the mechanical and electrical design of the sensor and can be negatively affected by temperature fluctuations. The dynamic noise of the instrument comes from two major sources, the

angular acceleration and the translational acceleration of the platform. The sensitivity of the gradiometer to angular accelerations of the platform can be reflected as angular misalignment, angular acceleration, angular velocity, and angular velocity squared in the gradiometer output. The sensitivity of the gradiometer output to translational acceleration of the platform can be produced due to two effects. The first one is when the center of mass is not at the center of pivot, which is called the residual mass dipole moment. The second one is called the induced dipole moments and that happens when the two test masses and their pivot axes are deformed over time. The third error source comes from the fact that there are some non-linearities in the magnetic and mechanical springs of the instrument, which cause the two responders to have different resonant frequencies during the operation. To achieve the target precision of the gradiometer, pairs of accelerometers with identical resonant frequencies should be designed.

Table 1-2 shows the different error sources affecting the gradiometer output. Results showed in this table indicate that the claimed target resolution over a bandwidth of 0.001 to 1 Hz is possible to happen in laboratory situation. As can be seen in this table, the translational accelerations has the largest error contribution.

Table 1-2: Error contribution to the output of the superconductive angular gradiometer on a mobile platform (Moody 2011)

Error source	Magnitude (Eötvös RMS 0.001-1.0 Hz)
Thermal noise	0.10
Translational acceleration	0.69
Angular acceleration	0.18
Angular velocity (centrifugal acceleration)	0.12
Non-linear response to angular acceleration	0.20
Non-linear response to translational acceleration	0.14
Temperature fluctuations	0.40
Total	0.88

To minimize the effect of mentioned errors in the output of the gradiometer, there are three approaches: mechanical, electrical and post processing. The first approach is to mechanically stabilize the rotational motion of the gradiometer about all three axes. In the second approach, two rejection ratios, named linear acceleration rejection ratio (LARR) and common mode rejection

ratio (CMRR), are computed through the sensing circuits and applied to the voltage measurements during the real time operation. The LARR and CMRR are used to minimize the translational and angular accelerations of the platform while amplifying the wanted signal, which is the gradient. In the third approach, the rotational and translational motions of the platform are measured during the operation with the help of superconductive translational and angular accelerometers. Then the gradiometer output is post processed along with the output of these two auxiliary superconductive sensors. The post processing of the data can easily eliminate the error terms due to angular orientation, angular acceleration, and residual first order terms. But the post processing is not able to remove the complete effects of the angular velocities and/or angular velocities squared. That is why the first and second approaches are highly recommended to reduce this effect before doing any post processing analysis (Matthews 2002, Moody and Paik 2007, Moody 2011).

The OQR type superconductive angular gradiometer, as explained before, is influenced by many errors. As is published in Matthews (2002), all these errors have their own analytical expressions and can be removed from the gradiometer channel through electrical, mechanical, and empirical procedures. Among all these systematic contributions, the effect of angular velocities squared is the main subject of this thesis. Angular velocities were not directly measured during the operation. Whereas angular accelerations are measured during the operation, the angular velocity squared can be computed by integration. However, a major difficulty arises when the measured angular accelerations are noisy because of translational accelerations of the platform and temporal fluctuations of the environment during the operation. These errors are a source of low and high frequency errors in the accelerometer output. Therefore, filtering of angular accelerations is necessary before integrating them to produce angular velocities. There is an empirical approach that has been applied by the industry to the angular accelerations to compensate for the mentioned major error sources. Based on this empirical approach, multiple linear regression and Butterworth low pass filtering were applied to mitigate the low and high frequency errors in the angular accelerations, respectively. As a result of this regression approach, the low frequency errors are not fully removed while the high frequency errors are minimized to some extent. The multiple linear regression approach engages the output of the three sensors to model the low frequency errors of the angular accelerations. This approach is quite expensive, complicated, and not able to

remove the low frequency errors. Therefore, a main objective of this thesis is to test if there is an alternative method to deal with the mentioned errors in the angular gradiometer output, particularly in the angular velocities squared, rather than the mechanical, electrical, and empirical approaches that companies employ for this purpose. Ultimately, we would like to answer the fundamental question of what the quality of the gradiometer output is after removing the angular velocities squared. The proposed methodologies in this thesis are wavelet de-trending and de-noising to cope with low and high frequency errors of the available data, respectively. Additionally, another frequency domain filter, namely a Wiener low pass filter, will be applied to the data. Finally, the gradiometer output accuracy will be evaluated through a simulation analysis.

1.2 Thesis objectives

The main objective of this research is to find an alternative signal processing approach to deal with the errors in the output of the superconductive angular accelerometer other than the electronic and mechanical compensation for errors. This method can be considered as cost-effective and less complex method in comparison to old empirical and mechanical approaches. It can also successfully remove the low and high frequency portion of the errors in the angular accelerometer output. Once the high quality angular accelerations are obtained, the angular velocities squared can be calculated. Angular velocity squared is one of the major error contributions in the gradiometer channel. Ultimately, the gradiometer output can be cleaned from the angular velocities squared contribution. The sub-objectives of this thesis are listed below:

- i. Investigating the error sources of superconductive angular and translational accelerometers and superconductive angular gradiometer.
- ii. Determining the best filtering approach to remove high frequency errors in the angular acceleration data using wavelet de-noising and Wiener low pass filtering.
- iii. Removing the low frequency error in the angular acceleration data through a wavelet multiresolution technique.

- iv. Apply the best filtering approach to angular accelerations and provide high quality angular velocities squared. Then, remove the effect of angular velocities squared from the gradiometer output.
- v. Evaluate the performance of the angular gradiometer output after removing the angular velocities squared from the raw gradient. I.e., try to assess how good the gradient is at the end of all these processes, and make this quality control procedure part of the suggested workflow.

1.3 Thesis outline

After this introductory chapter, five more chapters constitute the main body of this thesis as follows:

In chapter 2, principles and theories related to gravimeters and gradiometers will be discussed. The principle of different kind of superconductive accelerometers along with their system equations both in stationary and dynamic operations will be introduced. The OQR type gradiometer (the major focus of this research), its measurements and corresponding error sources will be discussed in details. Moreover, some current industrial airborne gradiometer systems will be reviewed.

Chapter 3 describes the Gedex HD-AGGTM instrument, which is the OQR typed gradiometer, used in this thesis. How the system is mechanized in theory and its measurement equations will be discussed. In addition, different data sets from the output of the gradiometer along with different auxiliary inertial sensors will be introduced. A full description regarding the error characteristics of the superconductive angular and translational accelerometers will be given. Furthermore, the empirical approach used by Gedex in the error analysis of the superconductive angular accelerometer will be explained.

Chapter 4 focuses on the wavelet spectral technique and Wiener low pass filtering of the static x angular acceleration data. The static data came from the instruments that was running undisturbed in a lab. Procedures for selecting the optimum wavelet base function, level of decompositions,

threshold type and threshold rescaling will also be discussed. A couple of wavelet de-noising and de-trending procedures will be tested on the static x angular acceleration data. The wavelet filtering techniques will be compared with the results of Wiener low pass filtering and also with the results of the empirical approach in removing the high and low frequency errors from the data. Eventually, the best filtering technique that provides the minimum RMS value for the noise floor will be selected for differential mode, x and y angular accelerations measurements.

Chapter 5 deals with the error analysing of the dynamic data. This data came from the instrument that was operating under sinusoidal rotations in the lab. The best filtering approaches found from analysing the static data in Chapter 4 will be used to reduce the noise level in dynamic x and y angular accelerations. High quality angular accelerations will be integrated and then squared to calculate the angular velocities squared. Angular velocities squared will be removed from the raw dynamic gradient. To evaluate the performance of the gradiometer output, simulations will be done since real control data have not been provided by Gedex.

Conclusions and recommendations for future work will be presented in Chapter 6.

Table 1-3 summarizes the thesis major objectives as outlined in Section 1.2 corresponding to the thesis chapters.

Table 1-3: Major thesis objectives covered in each chapter

Chapter	1	2	3	4	5	6
Objective		(i)		(ii)-(iii)	(iv)-(v)	

Chapter 2: Principles and systems of airborne gravity gradiometry

Both gravimetry and gradiometry instruments can be operated in an Earth-fixed set-up (stationary operation) or a mobile platform (dynamic operation). The dynamic operation refers to airborne application in this thesis, where the instruments are on board an airplane when collecting measurements. In airborne gravimetry, the accelerometer measurement is not only a function of specific force and torque, but also of other unwanted forces, such as the acceleration of the platform and the centrifugal effect. Therefore, the fundamental problem in mobile gravimetry data acquisition is the true separation of the gravity acceleration from unwanted forces (Schwarz and Li 1996). One way to reject these unwanted accelerations (common mode acceleration) is to use gravity gradiometers instead of gravimeters (Dransfield and Lee 2004, Matthews 2002, Moody et al. 2002, Moody and Paik 2007).

Gravity gradiometers consist of pairs of accelerometers, and their measurements are based on the difference between the outputs of each accelerometer. Thus, the separation of the gravity signal from inertial effects can be achieved efficiently. However, some noise still remains, which needs to be modeled and removed from the gradiometer output. The residual effects of the noise in airborne gradiometry can be eliminated by measuring the dynamics of the flight during the operation with the help of auxiliary sensors. As a result, the removal of the dynamic vibration from the output of the gradiometer using auxiliary measurements is possible.

This chapter begins with the theoretical background related to superconductive angular accelerometers and gradiometers. It reviews the basic theories of a test mass that can experience force and torque in the gravity field of the Earth, both in stationary and dynamic operations. The principles and error contributions of the different kinds of accelerometers and gradiometers are discussed. Moreover, a brief review of current industrial gravity gradiometers is presented at the end of the chapter.

2.1 Theoretical background

This section contains information related to the definition of the gradient tensor, force and torque equations, both in stationary and dynamic operations. The basic theory equations can be used in this section to model the output of a superconductive angular accelerometer and, as a result, the output of a superconductive angular gradiometer. Although some basic relations related to translational accelerometers and force measurement gradiometers are provided in this section, the major focus of this thesis is the superconductive angular accelerometer and superconductive angular gradiometer systems.

2.1.1 Gravity gradients

Gravity accelerations and gravity gradients are the direct measurements of gravimeters and gradiometers, respectively. Mathematical expressions for both components come from universal law of gravitation, which is explained below. Based on this law, the vector gravity field of a test mass with a density distribution of $\rho(\mathbf{r}')$ and volume V can be described by a scalar field $\phi(\mathbf{r})$ as (Hofmann-Wellenhof and Moritz 2006):

$$\phi(\mathbf{r}) = -G \int_V \frac{\rho(\mathbf{r}')}{|\mathbf{r}-\mathbf{r}'|} dV \quad (2-1)$$

where

- \mathbf{r} : Position vector from computation point
- \mathbf{r}' : Position vector from integration point
- G : Gravity constant ($6.67 \times 10^{-11} m^3 kg^{-1} s^{-2}$)

The first spatial derivative of the gravity potential field $\phi(\mathbf{r})$ is called the gravity acceleration \mathbf{g} , which can be written in Cartesian coordinates as:

$$\mathbf{g} = \nabla\phi(\mathbf{r}) = \frac{\partial\phi}{\partial x}\hat{i} + \frac{\partial\phi}{\partial y}\hat{j} + \frac{\partial\phi}{\partial z}\hat{k} \quad (2-2)$$

Where ∇ is the gradient operator and \hat{i} , \hat{j} , \hat{k} are the unit vectors in the x, y, and z directions, respectively.

The second spatial derivative of the gravity potential field $\phi(\mathbf{r})$ is called the gravity gradient tensor Γ_{ij} which can be represented in Cartesian coordinates as:

$$\Gamma_{ij} = \nabla^2 \phi(\mathbf{r}) = \frac{\partial^2 \phi}{\partial x_i \partial x_j} = \begin{bmatrix} \frac{\partial^2 \phi}{\partial x^2} & \frac{\partial^2 \phi}{\partial x \partial y} & \frac{\partial^2 \phi}{\partial x \partial z} \\ \frac{\partial^2 \phi}{\partial x \partial y} & \frac{\partial^2 \phi}{\partial y^2} & \frac{\partial^2 \phi}{\partial y \partial z} \\ \frac{\partial^2 \phi}{\partial x \partial z} & \frac{\partial^2 \phi}{\partial y \partial z} & \frac{\partial^2 \phi}{\partial z^2} \end{bmatrix} = \begin{bmatrix} \Gamma_{xx} & \Gamma_{xy} & \Gamma_{xz} \\ \Gamma_{xy} & \Gamma_{yy} & \Gamma_{yz} \\ \Gamma_{xz} & \Gamma_{yz} & \Gamma_{zz} \end{bmatrix} \quad (2-3)$$

It has only five independent elements, Γ_{xx} , Γ_{xy} , Γ_{xz} , Γ_{yy} , and Γ_{yz} , because it is symmetric by construction and it is traceless (the sum of the diagonal components is equal to zero). The gradiometer instruments are designed to measure some or all the components of this tensor or a linear combination of them.

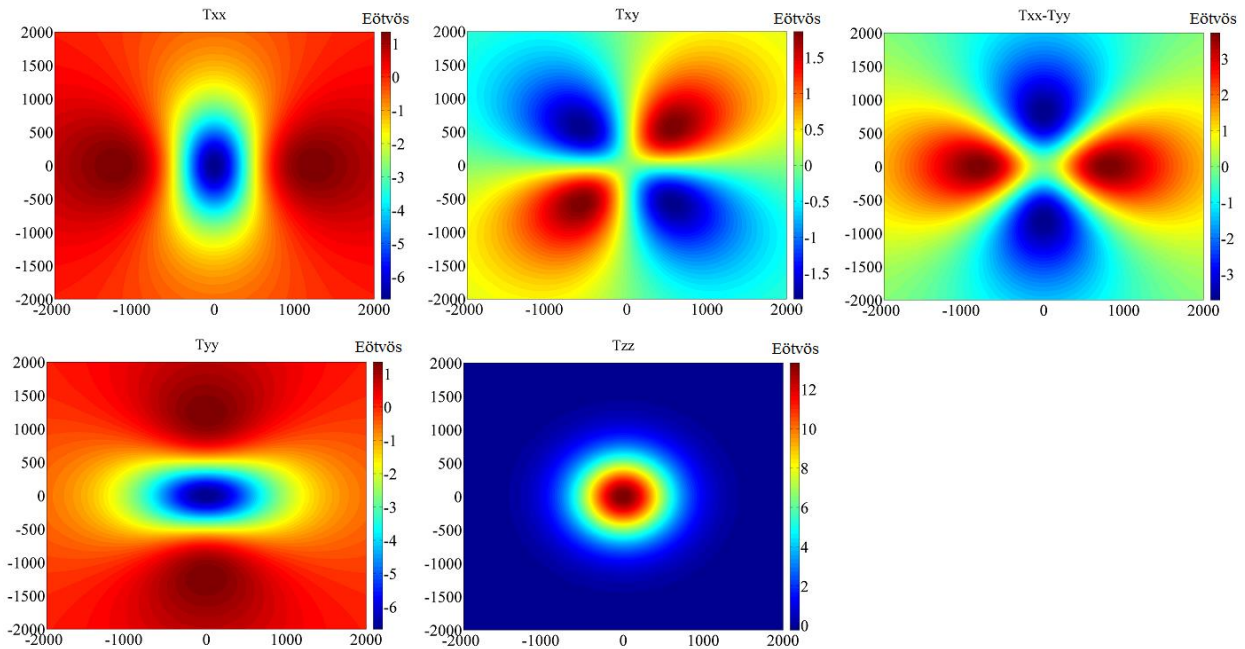


Figure 2-1: Some of the components of the gravity gradient tensor in Eötvös calculated for a 100 tonne spherical mass of radius 2 m, density contrast 1500 kg/m³ and depth of 1000 m

The Γ_{xx} and Γ_{xz} components are useful for imaging north-south edges of geological targets whereas Γ_{yy} and Γ_{yz} are useful for imaging east-west edges of geological features. The Γ_{xy} component can show a quadrupole characteristics of the geophysical target. Finally, the Γ_{xx} and Γ_{yy} magnitudes are useful for imaging the thickness of geological features (Murphy 2004). As an example, the Γ_{zz} ,

Γ_{xy} , Γ_{xx} and Γ_{yy} components of the gravity gradient tensor for a spherical body are depicted in Figure 2-1.

2.1.2 Force and torque experienced by a test mass in a gravity field (stationary operation)

Force and torque parameters are defined as a function of linear and angular momentum in classical mechanics. Since this thesis uses some formulas related to momentum equations, linear and angular momentum equations are first introduced, and, the force and torque equations are then written in terms of these parameters. Considering Figure 2-2, the linear momentum \mathbf{p} of a moving point mass m with velocity \mathbf{v} is written as (Goldstein 1965):

$$\mathbf{p} = m\mathbf{v} \quad (2-4)$$

A total force \mathbf{F} acting on this point mass is defined as the first derivative of the linear momentum \mathbf{p} as:

$$\mathbf{F} = \frac{d\mathbf{p}}{dt} = \frac{d}{dt}(m\mathbf{v}) = m\frac{d\mathbf{v}}{dt} = m\mathbf{a} \quad (2-5)$$

where \mathbf{a} is the acceleration of the test mass. Equation (2-5) is known as Newton's second law.

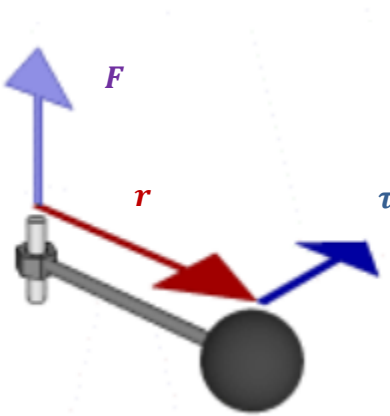


Figure 2-2: Torque and force experience by a test mass
(<http://en.wikipedia.org/wiki/File:Torque-animation.gif>)

The angular momentum \mathbf{L} is defined as a cross product of the radius vector \mathbf{r} and the linear momentum \mathbf{p} as:

$$\mathbf{L} = \mathbf{r} \times \mathbf{p} = \mathbf{r} \times m\mathbf{v} \quad (2-6)$$

The velocity of the rotating body \mathbf{v} is defined as a cross product between the angular velocity of the body $\boldsymbol{\Omega}$ and the radius vector \mathbf{r} as:

$$\mathbf{v} = \boldsymbol{\Omega} \times \mathbf{r} \quad (2-7)$$

Thus, Equation (2-6) can be written as:

$$\mathbf{L} = \sum m(\mathbf{r} \times (\boldsymbol{\Omega} \times \mathbf{r})) = \mathbf{I}\boldsymbol{\Omega} \quad (2-8)$$

where is summation $n\mathbf{I}$ is the moment of inertia tensor and has the following diagonal and off-diagonal components in a Cartesian coordinate frame:

$$\mathbf{I} = m \begin{bmatrix} y^2 + z^2 & -xy & -xz \\ -xy & x^2 + z^2 & -yz \\ -xz & -yz & x^2 + y^2 \end{bmatrix} = \begin{bmatrix} I_{xx} & I_{xy} & I_{xz} \\ I_{xy} & I_{yy} & I_{yz} \\ I_{xz} & I_{yz} & I_{zz} \end{bmatrix} \quad (2-9)$$

Finally, the moment of force or torque applied on a test mass is the cross product between the radius vector \mathbf{r} and the total force \mathbf{F} as:

$$\boldsymbol{\tau} = \mathbf{r} \times \mathbf{F} \quad (2-10)$$

Equation (2-10) can also be written in terms of the first derivative of the angular momentum as follows:

$$\boldsymbol{\tau} = \mathbf{r} \times \frac{d}{dt}(m\mathbf{v}) = \frac{d}{dt}(\mathbf{r} \times m\mathbf{v}) = \frac{d\mathbf{L}}{dt} \quad (2-11)$$

Thus far, the general forms of the torque and force equations were derived without considering the background environment. If the gravity field of the Earth is considered as the background environment, torque and force equations will have a different form which is explained in the following paragraphs.

Using Equation (2-5) and considering Figure 2-3, the force $f(\mathbf{r})$ experienced by the test mass in stationary operation in the gravity field of the Earth is written as:

$$f(\mathbf{r}) = g(\mathbf{r})\rho(\mathbf{r}) \quad (2-12)$$

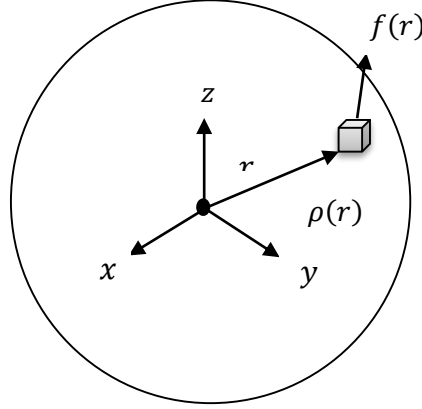


Figure 2-3: A mass body with density $\rho(\mathbf{r})$ in a gravity field of the Earth in a Cartesian coordinate frame

Considering Equation (2-10), the test mass in a gravity field can experience a torque, which is calculated as:

$$\boldsymbol{\tau}_\Gamma = \mathbf{r} \times f(\mathbf{r}) \quad (2-13)$$

There is a relation between the torque vector and off-diagonal component of gradient tensor. It can be proven that the relation in a Cartesian coordinate frame is as shown below (Carroll et al., 2010b):

$$\boldsymbol{\tau}_\Gamma = \int_{Body} \begin{bmatrix} -xz\Gamma_{yx} + xy\Gamma_{zx} - yz\Gamma_{yy} + y^2\Gamma_{zy} - z^2\Gamma_{yz} + yz\Gamma_{zz} \\ -xz\Gamma_{xx} - x^2\Gamma_{zx} + yz\Gamma_{xy} - xy\Gamma_{zy} + z^2\Gamma_{xz} - xz\Gamma_{zz} \\ -xy\Gamma_{xx} + x^2\Gamma_{yx} - y^2\Gamma_{xy} + xy\Gamma_{yy} - yz\Gamma_{xz} + xz\Gamma_{yz} \end{bmatrix} \rho(\mathbf{r})dV \quad (2-14)$$

By considering the pivot axis as the z-axis and by assuming the same axis as the principle axis ($I_{yz} = I_{zx} = 0$), the torque around the z-axis can be written in terms of inertial moment component as:

$$\tau_z = \Gamma_{xy}(I_{yy} - I_{xx}) - I_{xy}(\Gamma_{yy} - \Gamma_{xx}) \quad (2-15)$$

It is clear from Equation (2-15) that the torque vector on a test mass is proportional to both the off-diagonal components of the cross gravity gradient and/or gravity gradient difference and moments of the inertial tensor.

In stationary operation, a translational accelerometer measures the specific force that is mathematically expressed with Equation (2-12) while an angular accelerometer measures the applied torque, which is mathematically expressed with Equation (2-14).

2.1.3 Force and torque experienced by a test mass in a gravity field (dynamic operation)

The force experienced by a test mass, located in a moving platform (non-inertial reference frame) is not only a function of gravity acceleration, but also the platform's acceleration. Goldstein (1965) presented a detailed analysis of this effect; therefore, only a brief explanation is provided in this thesis. The acceleration of the test mass in a dynamic operation relative to an inertial frame is written as (Goldstein 1965):

$$\mathbf{a}_i = \mathbf{a}_b + \dot{\boldsymbol{\Omega}} \times \mathbf{r} + 2(\boldsymbol{\Omega} \times \mathbf{v}_b) + \boldsymbol{\Omega} \times (\boldsymbol{\Omega} \times \mathbf{r}) \quad (2-16)$$

where

$$\begin{aligned} 2\boldsymbol{\Omega} \times \mathbf{v}_b & : \text{Coriolis acceleration} \\ \boldsymbol{\Omega} \times (\boldsymbol{\Omega} \times \mathbf{r}) & : \text{Centrifugal acceleration} \\ \dot{\boldsymbol{\Omega}} \times \mathbf{r} & : \text{Tangential or Euler acceleration} \\ \mathbf{a}_i = \left(\frac{d\mathbf{v}}{dt}\right)_i & : \text{Acceleration in inertial frame} \\ \mathbf{a}_b = \left(\frac{d\mathbf{v}}{dt}\right)_b & : \text{Acceleration in body frame (platform)} \\ \dot{\boldsymbol{\Omega}} = \frac{d\boldsymbol{\Omega}}{dt} & : \text{The angular acceleration of the rotating reference frame w.r.t body frame} \end{aligned}$$

Thus, the total force experienced by the moving particle in a rotating reference frame is written as:

$$\mathbf{f}_b = m(\mathbf{g} + \mathbf{a}_i) = m(\mathbf{g} + \mathbf{a}_b + \dot{\boldsymbol{\Omega}} \times \mathbf{r} + 2\boldsymbol{\Omega} \times \mathbf{v}_b + \boldsymbol{\Omega} \times (\boldsymbol{\Omega} \times \mathbf{r})) \quad (2-17)$$

In dynamic operation, the translational accelerometer measures the specific force, which mathematically expressed with Equation (2-17). It is clear from this equation that except for the gravity vector, which is a wanted term here, there are many unwanted terms due to operation of the sensor in the mobile platform.

The torque experienced by a particle in the gravity field in an inertial frame is the sum of the torque from the platform angular motion $\boldsymbol{\tau}_b$ and the torque as a result of the gravity gradient $\boldsymbol{\tau}_\Gamma$ (Moody et al., 2003):

$$\left(\frac{d\mathbf{L}}{dt}\right)_i = \boldsymbol{\tau}_b + \boldsymbol{\tau}_\Gamma \quad (2-18)$$

where \mathbf{L} is the angular momentum vector. The equation of angular motion for the particle in a moving platform can also be written as follows:

$$\left(\frac{d\mathbf{L}}{dt}\right)_i = \left(\frac{d\mathbf{L}}{dt}\right)_b + \boldsymbol{\Omega}_b \times \mathbf{L} \quad (2-19)$$

Therefore, using both Equations (2-18) and (2-19), we have:

$$\boldsymbol{\tau}_b + \boldsymbol{\tau}_\Gamma = \left(\frac{d\mathbf{L}}{dt}\right)_b + \boldsymbol{\Omega}_b \times \mathbf{L} \quad (2-20)$$

Thus, the torque from the body movement can be written in terms of the torque from the platform movement, the torque from the gravity gradient, and the cross product between the platform angular velocity and the angular momentum vector as:

$$\left(\frac{d\mathbf{L}}{dt}\right)_b = \boldsymbol{\tau}_b + \boldsymbol{\tau}_\Gamma - \boldsymbol{\Omega}_b \times \mathbf{L} \quad (2-21)$$

The only parameter that is expanded in this section is the third term $\boldsymbol{\Omega}_b \times \mathbf{L}$ in Equation (2-20). For this purpose, Levi-Civita per-mutation symbols ε_{ijk} are defined as (Guio 2011):

$$\varepsilon_{ijk} = \begin{cases} +1 & \text{if } ijk = xyz, zxy, \text{ or } yzx \\ -1 & \text{if } ijk = yxz, zyx, \text{ or } xzy \\ 0 & \text{all other cases (any equal indices)} \end{cases} \quad (2-22)$$

Using Levi-Civita symbols, the cross product of two vectors can be written as:

$$(A \times B)_i = \sum_{j=1}^3 \sum_{k=1}^3 \varepsilon_{ijk} A_j B_k \quad (2-23)$$

Therefore, the $\mathbf{\Omega}_b \times \mathbf{L}$ term can be written as:

$$\mathbf{\Omega}_b \times \mathbf{L} = \varepsilon_{ijk} \Omega_j L_k = \varepsilon_{ijk} \Omega_j I_{km} \Omega_m \quad (2-24)$$

Considering the measurement axis as the z-axis, Equation (2-24) can be written as:

$$\mathbf{\Omega}_b \times \mathbf{L} = I_{xy}(\Omega_x^2 - \Omega_y^2) + \Omega_x \Omega_y (I_{yy} - I_{xx}) \quad (2-25)$$

Using Equation (2-8), it is easy to show that:

$$\left(\frac{d\mathbf{L}}{dt}\right)_b = \frac{d(\mathbf{I}\mathbf{\Omega})}{dt} = \mathbf{I} \frac{d\mathbf{\Omega}}{dt} = \mathbf{I}\dot{\mathbf{\Omega}} \quad (2-26)$$

The torque due to the gravity gradient $\boldsymbol{\tau}_\Gamma$ from Equation (2-15), $\mathbf{\Omega}_b \times \mathbf{L}$ from Equation (2-25), and $\left(\frac{d\mathbf{L}}{dt}\right)_b$ from Equation (2-26) can be substituted into Equation (2-21) to derive the general expression for the torque about the z-axis of the rigid body as follows (the subscript b has been dropped):

$$I_{zz}\dot{\Omega}_z = \tau_z + \Gamma_{xy}(I_{yy} - I_{xx}) - I_{xy}(\Gamma_{yy} - \Gamma_{xx}) - I_{xy}(\Omega_x^2 - \Omega_y^2) - \Omega_x \Omega_y (I_{yy} - I_{xx}) \quad (2-27)$$

$$I_{zz}\dot{\Omega}_z = \tau_z - I_{xy}[(\Gamma_{yy} - \Gamma_{xx}) + \Omega_x^2 - \Omega_y^2] + (I_{yy} - I_{xx})(\Gamma_{xy} - \Omega_x \Omega_y) \quad (2-28)$$

Equation (2-28) is Equation (17) in Moody et al., (2003) paper. However, it has been corrected for some sign errors.

In dynamic operation, the angular accelerometer measures the applied torque, which is mathematically expressed with Equation (2-28). Typically, depending on the design of the system, either the second term or the third term can be disappeared in Equation (2-28). For example, when the x- and y-axes of the test mass are parallel to the platform axes, I_{xy} is zero; thus, the second term is omitted from this equation. In this case, the single accelerometer output is generated in principal axis view. When there is a symmetry in the angular accelerometer test mass, then $I_{yy} = I_{xx}$ and the third term can be eliminated from this equation (Moody et al., 2003). In this case, the

single accelerometer output is generated in standard axis view. More detail explanations of the standard and principal axes are presented in Chapter 3.

2.2 Principles of different types of accelerometers and gradiometers

Accelerometers are the major part of any gradiometer. Actually, the type of accelerometer determines how a gradiometer provides its results. There are two common types of accelerometers: translational and angular. The former measures the applied force, which leads to translational acceleration in m/s^2 ; the latter measures applied torque, which leads to angular acceleration in rad/s^2 . Depending on the type of accelerometer used in the gradiometer design, there can be either applied force or torque measurement gradiometers. Since a specific kind of accelerometer from superconductive material is used in this thesis, the major focus of this work is related to this kind of accelerometer. Thus, the following sub-sections explain the principles of superconductive translational and angular accelerometers and gradiometers.

2.2.1 Principle of superconductive translational accelerometers

Superconductive translational accelerometers measure acceleration in three orthogonal directions in units of m/s^2 . The principle of superconductive translational accelerometers follows the vertical spring balance principle as stated in detail in Torge (1989). However, in this research work, the principle of the superconductive translational accelerometer can be explained in terms of its sensing circuitry. Considering Figure 2-4, the spring is stretched (extended) from its equilibrium position when the superconducting proof mass is undergoing acceleration. Consequently, the sensing coil's inductance changes as does the quantized magnetic flux Φ in loop 32. Afterwards, the circulating current must change to keep the original flux in the loop. This new current corresponds to the displacement of the test mass Δx , and is amplified and detected by a superconducting quantum interference device (SQUID) (Moody and Paik 2004).

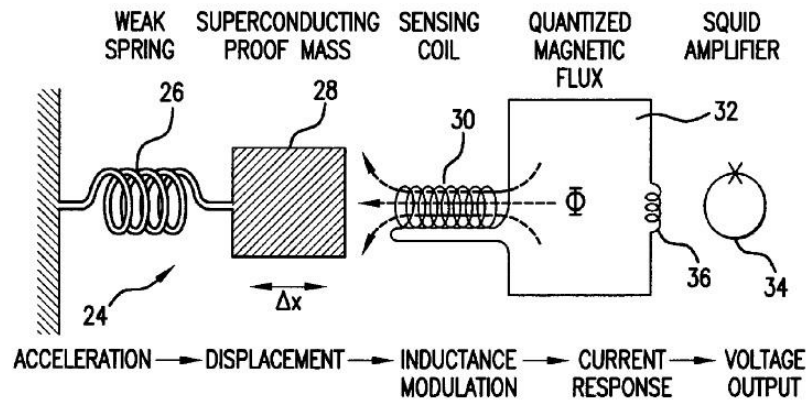


Figure 2-4: Superconducting translational accelerometer sensing circuit (Moody and Paik 2004)

Chapter 3 of this thesis explains how this current or voltage output is converted to test mass displacement in units of m , and ultimately how a quantity in m/s^2 is measured as the output of the instrument. This principle is only valid in theory. In practical situations, there is a sensitivity between the output of the accelerometer and the temperature fluctuations of the environment during operation that affects the accelerometer output. This concept is going to be explored in details in Chapter 3.

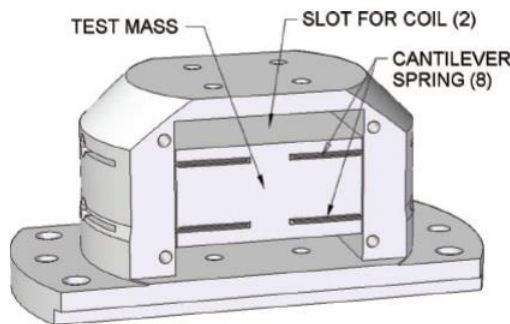


Figure 2-5: Mechanical component of the superconductive translational accelerometer (Moody and Paik 2004)

Figure 2-5 shows the mechanical component of the superconductive translational accelerometer. The explanation related to the translational accelerometer’s mechanical component is quoted from Moody (2011) as “the test mass is supported by eight cantilever springs. Each spring is 11.7 mm

long, 6.4 mm in wide, and 0.2 mm thick. The entire mechanical component is cut from a single block of Nb to attain a well-defined sensitive axis direction.”

2.2.2 Principle of superconductive angular accelerometers

Superconductive angular accelerometers measure the second time derivative of the angular displacement or angular accelerations in rad/s^2 . The principle of superconductive angular accelerometers follows the lever spring balance principle, as stated in detail in Torge (1989). However, in this research work the superconductive angular accelerometer principle can be explained through its sensing circuitry, as illustrated in Figure 2-6.

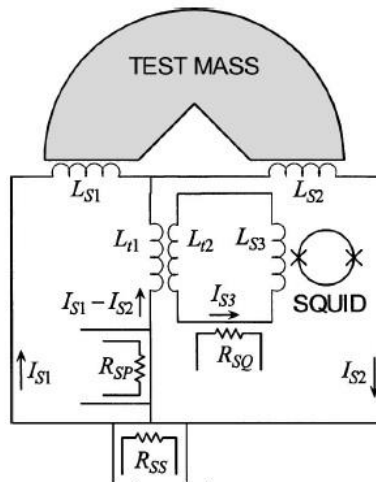


Figure 2-6: Superconductive angular accelerometer sensing circuit (Moody 2011)

Spiral coils labelled as L_{S1} and L_{S2} at the top of the design are responsible for sensing any angular deflection (displacement) of the superconducting test mass. When there is a test mass deflection due to angular acceleration of the platform, the flux is caught in the opposite direction with the help of the heat switch, R_{SP} . In this case, the current flows through transformer L_{t1} and then splits between the two coils. Eventually, the SQUID is able to detect the current, which is proportional to the test mass angular deflection (Moody et al., 2003). Chapter 3 explains how this current or voltage output detected by the SQUID is converted to test mass deflection in units of rad and

ultimately how a quantity in rad/s^2 is measured as the output of the instrument. This principle is also only valid in theory. In practical situations, there are a number of error sources that affect the output of the angular accelerometer, which is explained in detail in Chapter 3, as well.

The mechanical component of the superconductive angular accelerometer is illustrated in Figure 2-7. The explanation related to the angular accelerometer's mechanical component is quoted from Moody (2011) as “the test mass, flexure, and the housing are all made from niobium (Nb), which is a superconducting material at 9.2 K temperature. Dimensions of the angular accelerometer body are 102 cm \times 102 cm \times 2.4 cm.”

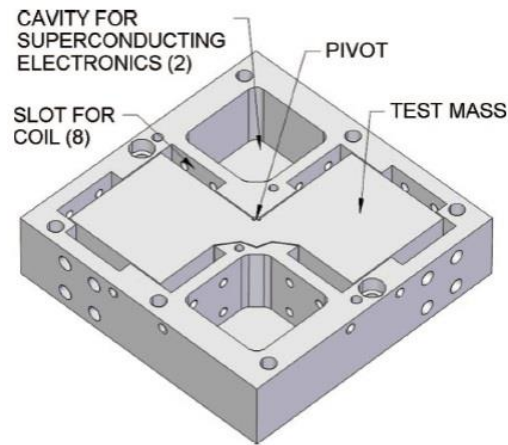


Figure 2-7: Mechanical component of the superconductive angular accelerometer (Moody 2011)

In dynamic operation, the superconductive angular accelerometer is able to measure the angular acceleration of the platform during its operation. That is why this instrument is considered a major component that can accompany an angular gradiometer. The superconductive angular accelerometer's output can help to compensate for the output of the gradiometer due to the sensitivity of the gradiometer output to the angular displacement of the platform. However, this superconductive angular accelerometer is a very sensitive instrument in that the output contains some errors due to the intrinsic noise of the instrument and the dynamic vibration of the platform. The intrinsic noise of the instrument depends on the mechanical and electrical design of the accelerometer and can be minimized by optimizing the mechanical and electrical design of the

system. Since the operating temperature for a superconductive material is 4.3 K , any temperature fluctuations during the operation will affect the optimum mechanical and electrical design of the system over time.

A major error contribution to the output of the superconductive angular accelerometer comes from misalignment errors, the translational movement of the platform and the temperature fluctuations of the environment during the operation (Moody et al., 2003). How these errors enter to the output of the instrument is explained in Chapter 3 and the modeling of these errors is the major focus of Chapter 4.

2.2.3 Principle of specific force gravity gradiometers

Specific force gradiometers are a combination of two translational accelerometers. The simple principle behind this kind of gradiometer is depicted in Figure 2-8.

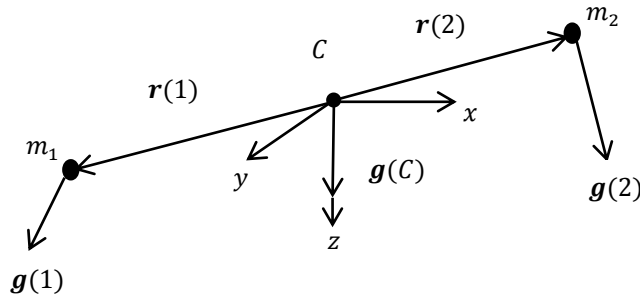


Figure 2-8: Principle of specific force measurement gradiometer

According to this figure, the gravity gradient at point C can be computed from the Taylor expansion of gravity accelerations at points 1 and 2 as:

$$\begin{aligned} g(1) &= g(C) + \Gamma(C)r(1) \\ g(2) &= g(C) + \Gamma(C)r(2) \end{aligned} \tag{2-29}$$

The difference between accelerations at these two points is written as:

$$\mathbf{g}(2) - \mathbf{g}(1) = \mathbf{\Gamma}(C)(\mathbf{r}(2) - \mathbf{r}(1)) \quad (2-30)$$

The gravity gradient can, therefore, be approximated by dividing Equation (2-30) by the distance between the two point masses as:

$$\mathbf{\Gamma} = \frac{\mathbf{g}(2) - \mathbf{g}(1)}{\mathbf{r}(2) - \mathbf{r}(1)} \quad (2-31)$$

If the gradiometer is working in a dynamic operation, the \mathbf{g} term in Equation (2-31) contains platform acceleration as written in Equation (2-16). Even though the output of the accelerometers is subtracted to achieve the gradiometer output, some residual platform acceleration effects remain and need to be modeled in this work; i.e., the output of the system is not only the gradient, but also the residual effects of the platform acceleration. The specific force gradiometer is not the major concern of this thesis work. Interested readers are referred to Matthews (2002) for details. The major focus of this study is torque measurement gradiometers, which are explained in the next sub-section.

2.2.4 Principle of torque gravity gradiometers

Torque measurement gradiometers are a combination of two angular accelerometers that pivot about a common axis. The simple principle of this system is depicted in Figure 2-9. In this figure, angular displacement is shown by Θ , which is approximately proportional to the torque τ acting on the test masses (showed in this figure by Bar A and Bar B).

In operation, there are two resonant modes of the gravity gradiometer: the common mode and the differential mode. The former comes from the platform angular accelerations, which causes the two test masses to rotate in the same direction. The latter comes from a gravity gradient from a nearby mass, which causes the two test masses rotate in opposite directions (Tryggvason et al., 2004). The output of the angular gradiometer (torque measurement gradiometer) is the difference between the angular motions of the two bars. Mathematical equations related to the output of the superconductive angular gradiometer is given in Section 3.2.

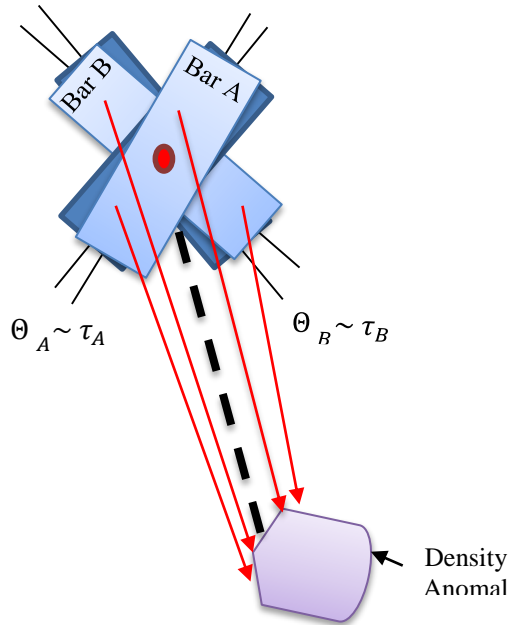


Figure 2-9: Principle of torque measurement gradiometer

In the case of any superconductive angular gradiometer, if the two bars have totally identical resonant frequencies, the SQUID is able to measure the pure gradient. However, in practice, the SQUID measures a produced response function that is not only a function of the gradient, but other unwanted terms. These unwanted terms will be described in Section 2.3.2. A very old example of torque gradiometer is the Eötvös torsion balance and a modern example is the orthogonal quadrupole responder (OQR). The OQR type superconducting gravity gradiometer follows the same principle as stated in this section. Since in this research data from an OQR type gradiometer is used, more details about the instrument and its major error sources are given in the next section.

2.3 OQR type superconducting gravity gradiometer

A superconductive gravity gradiometer includes a pair of superconductive angular accelerometers and measure the second spatial derivative of the gravity potential. A single angular accelerometer output is a function of both platform angular motions and the gravity gradients. However, a pair of angular accelerometers rotating about a common axis can generate a gradiometer, thus the

separation of the angular accelerations from the gravity gradients is possible. In simple terms, this is the principle behind the OQR type superconducting gravity gradiometers, one of which is depicted in Figure 2-10. The superconductive angular accelerometers are mounted on the opposite faces of the cube in this figure.

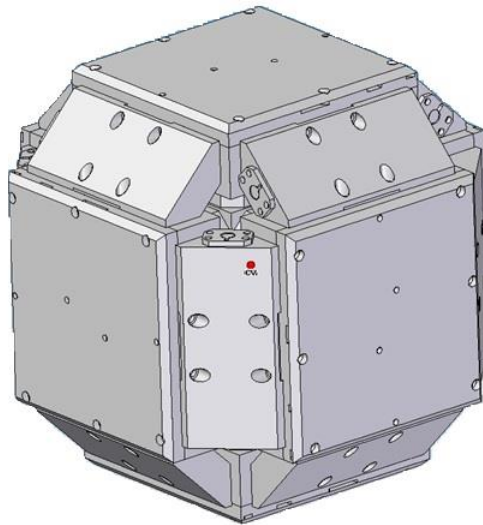


Figure 2-10: Basic structure of the OQR type superconductive angular gradiometer (Provided by Gedex)

The next sub-sections explain the principle of an OQR type superconductive gradiometer through its sensing circuits, the measurements of the gradiometer and the errors introduced in the output of the system. The instrument configuration in a moving platform is also explained.

2.3.1 Principle and measurement of OQR type superconducting gravity gradiometer

The OQR superconductive gradiometer measures either the angular accelerations (common mode) or the gravity gradients (differential mode). This electrically depends on how the persistent currents are accumulated in the sensing circuit (Moody 2011, Moody and Paik 2007). So the system's principle can be explained through its sensing circuitry, as illustrated in Figure 2-11. This figure shows a sensing circuit of a pair of superconductive angular accelerometers that are coupled. Coupling is done with mode-splitting circuitry 44 in this figure, where the coils of the two

accelerometers (inputs number 30) are connected in parallel with the SQUID coil (input number 36). As can be seen from this figure, coils 30 are very close to the test masses. Therefore, their inductance is proportional to the angular displacement of the test masses. There are two currents I_1 and I_2 corresponding to these angular displacements in Figure 2-11. The difference between these two signals is differential mode (gravity gradient), and the sum of the two is common mode (angular acceleration). The two currents are ideally equal if the test masses, springs, coils and the coil spacing (the gap between the test mass and the coil) are equal. As a result, their resonant frequencies are equal and the current difference $I_2 - I_1$ gives the relative angular displacement between the two test masses, which is proportional to the gravity gradient. However, this ideal situation is impossible in reality, and this current difference is a function of many other parameters such as mechanical, electrical, temperature fluctuation and platform accelerations (Moody 2011, Moody and Paik 2007).

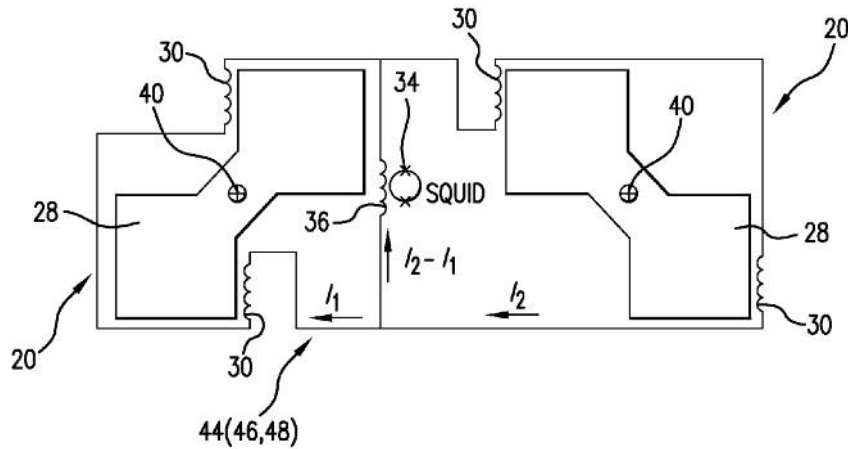


Figure 2-11: Schematic circuit for a pair of coupled superconductive angular accelerometers (Moody and Paik 2007)

In practice, measurements by the SQUID are a function of not only gravity gradient, but angular accelerations, angular velocities, and translational accelerations of the platform. Errors induced by these parameters are significantly larger than the desired gravity gradient signal. The target resolution of OQR type gravity gradiometers for exploration purposes is 1 Eötvös per sample second, which is influenced by these error sources (Tryggvason et al., 2004). This is why studying about the airborne gradiometry is considered a challenging work.

All these errors, as discussed thoroughly in Matthews (2002), have their own analytical expressions and can be removed from the gradiometer channel through electrical, mechanical, and empirical procedures. Because Gedex did not give us access to such information and data for all these error sources, they are not all discussed in this thesis. Studying the effect of angular velocity squared and how this affects the performance of the gradiometer output is the primary objective of this thesis. However, for the sake of completeness, the error sources of the OQR type gradiometer are briefly discussed in the following sub-section.

2.3.2 Errors in the output of OQR type superconducting gravity gradiometer

Errors in the OQR type gravity gradiometer data can be divided into three major groups. The first group is related to the inherent noise of the instrument, the second group is related to the operation of the instrument in a dynamic condition, and the third one is the effect of non-linearities on the gradiometer output. The inherent noise of the instrument's major component, i.e., the superconductive angular accelerometer, depends on the mechanical and electrical design of the superconducting gradiometer. Important mechanical parameters of the gradiometer include the accelerometer mass, radius of gyration, primary moment of inertia, sensing coil moment arm, and the resonance frequency. Important electrical parameters are the sensing coil inner and outer diameter, sensing coil spacing to the test masses, the SQUID energy resolution and dynamic range (Moody 2011). Thus, by optimally selecting the mechanical and electrical design parameters, this error will be minimized. Since the operating temperature for a superconductive material is 4.3 k, any temperature fluctuations during the operation affect the optimum mechanical and electrical design of the system over time. A temperature fluctuation error is a source of low frequency error in the output of the superconductive gradiometer and can be minimized by some passive and active temperature control stages during operation. It is also possible to minimize this error in a post processing mode if the temperatures are recorded during the operation (Matthews 2002). For more details about this errors refer to Matthews (2002).

Dynamic noise of the instrument comes from two major sources: the angular and translational acceleration of the platform. The sensitivity of the gradiometer output to the angular acceleration

of the platform can be reflected as angular accelerations and angular velocities of the moving platform in the gradiometer system equation. The sensitivity of the gradiometer output to translational acceleration of the platform can be produced due to two effects. The first one, residual mass dipole moment, occurs when the center of mass is not at the center of pivot. The second one is called induced dipole moment and happens when the two test masses are deformed and when their pivot axes are deformed over time. Bar and pivot distortion are produced because of the induced dipole moments. These two effects are illustrated in Figure 2-12 and Figure 2-13.

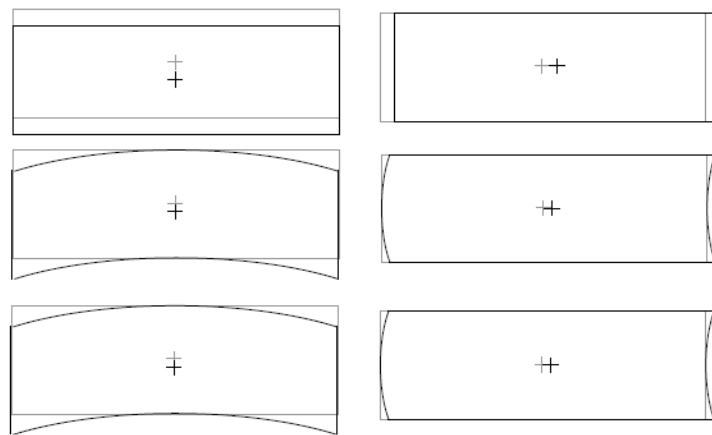


Figure 2-12: Bar distortion (induced dipole) (Matthews 2002)

To minimize the effect of residual dipole terms, the mechanical balance of the responders and superconducting acceleration compensation are needed. One way for decreasing the effects of induced dipole is using the parallel pivots. Another technique is the subtraction of the remaining effects in a post processing step. More detailed explanations can be found in Matthews (2002).

The third error contributing on the gradiometer output is the effect of non-linearities. As mentioned in Section 2.3.1, if the two responders have identical resonant frequencies, the SQUID measures the gravity gradient. However, in reality, non-linearities in the magnetic and mechanical springs limit the frequency matching of the two bars to a desired precision (Moody and Paik 2007).

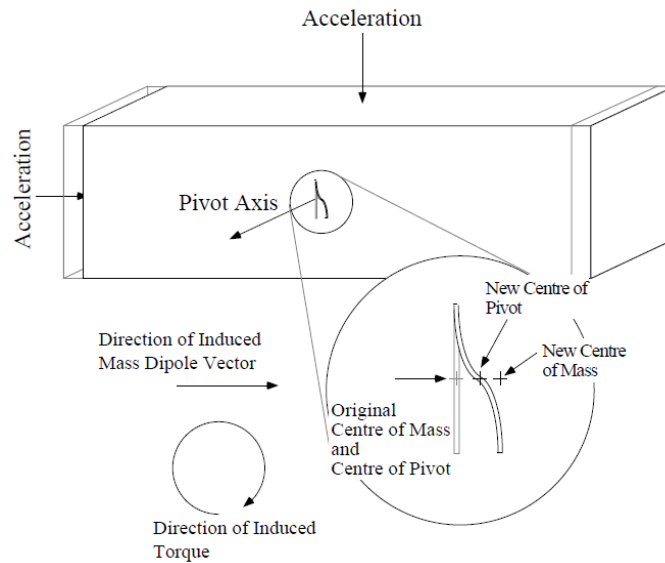


Figure 2-13: Pivot distortion (mass dipole) (Matthews 2002)

To minimize the effect of mentioned errors from the output of the gradiometer there are three approaches: mechanically, electrically and post processing. In the first approach, the rotational motion of the gradiometer is mechanically stabilized about all three axes. In the electrical approach, the linear rejection ratio (LARR) and common mode rejection ratio (CMRR) are indications for minimization of the translational and angular accelerations of the platform. Meanwhile, the wanted current, which is the gradient signal, is amplified. Finally, in the post processing approach, the rotational and translational motions of the platform are measured during the operation with the help of superconductive translational and angular accelerometers. The gradiometer output is then amended, along with the output of two auxiliary superconductive sensors. The post processing of the data can easily eliminate the error terms due to angular orientation, angular acceleration and residual first-order terms. However, due to the presence of a squared angular velocities and/or angular velocities in the gradiometer output, the first and second approaches are strongly recommended for decreasing the effect of the errors before doing any post processing (Matthews 2002, Moody and Paik 2007, Moody 2011).

2.3.3 Configuration of OQR type superconductive gravity gradiometer in a moving platform

In the operation mode, the gravity gradiometer output is measured along with the output of two other superconductive sensors, namely the translational and angular accelerometers. The instrument configuration is depicted in Figure 2-14. The reason for this assembly is that both superconductive translational and angular accelerations can be used to correct for the gravity gradiometer errors, as stated in the previous section. In a three-axes instrument, six superconductive angular accelerometers are coupled and mounted on the opposite faces of the cube, as shown in Figure 2-14.

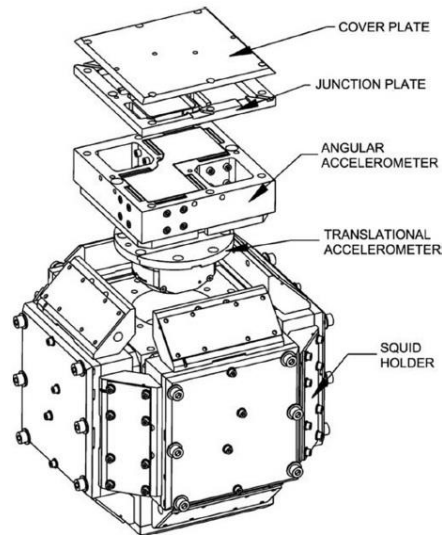


Figure 2-14: Three-axis superconductive angular gradiometer inside the SQUID holder plus superconductive translational and angular accelerometers (Moody 2011)

Three translational accelerometers are also mounted in orthogonal faces of the cube, of which one of is illustrated in the figure. Thus, x , y , and z translational and angular accelerations along with off-diagonal gravity gradient components are measured in this mechanical assembly. Using Laplace's equation, the diagonal components of the gravity gradients can be reconstructed, as well (Moody 2011, Carroll et al., 2010b).

2.4 Review of current industrial airborne gravity gradiometer systems

Four commercial gravity gradiometer systems are described here, namely the Falcon®, the Air FTG, The University of Western Australia Superconductive Gravity Gradiometer (UWA-SGG), and the Gedex High-Definition Airborne Gravity Gradiometer (Gedex HD-AGG™).

2.4.1 Falcon® Airborne Gravity Gradiometer

The Falcon® gravity gradient instrument is a force gradiometer mounted on a rotating platform and consists of four orthogonal translational accelerometers. The outputs of the accelerometers are summed to produce the gravity gradient signal. The Falcon® system additionally includes a laser scanner for creating a digital elevation model of the terrain, a GPS for positioning of the gravity gradient, time synchronization of different data sets, a caesium-vapour magnetometer, and an optional scintillation spectrometer. In post processing mode, all these sensors are integrated to attenuate the system noise. The Falcon® system measures the two horizontal gradient signals, Γ_{xy} and/or $(\Gamma_{yy} - \Gamma_{xx})$. It has been reported that more than 80% of the noise of the Falcon® gravity gradient is non-correlated (Dransfield and Lee 2004). The Falcon® noise is reported as “2.5 Eötvös RMS filtered to a 300 m wavelength” and corresponds to noise density of 6 Eötvös / $\sqrt{\text{Hz}}$ (Dransfield 2007).

2.4.2 Air-FTG airborne gravity gradiometer

The Air-FTG, like the Falcon®, is a kind of force gradiometer, but instead of two horizontal components, it measures the full gradient tensor (FTG). The Air-FTG is a combination of three gravity gradient instruments (GGIs) with two opposing pairs of translational accelerometers, as shown in Figure 2-15. The measurement of each GGI is a function of the corresponding gradients in the plane of the rotating disk, the distance between each accelerometer and the frequency spin of the disk. Therefore, five independent components of gravity gradient tensor, Γ_{xx} ,

Γ_{xy} , Γ_{xz} , Γ_{yy} , and Γ_{yz} , can be produced by the three-GGI configuration (Murphy 2004). The noise of the FTG data was classified in three groups: correlated noise, non-correlated high frequency noise and a shift in the mean level. The correlated noise in this system is produced by temperature and pressure fluctuations during the flight. The non-correlated noise is the residual noise after correction of the linear and angular motions of the aircraft. Finally, the shift in the mean level is due to the aircraft changing its directions and changing its altitude (Barnes and Lumley 2010, Murphy 2004).

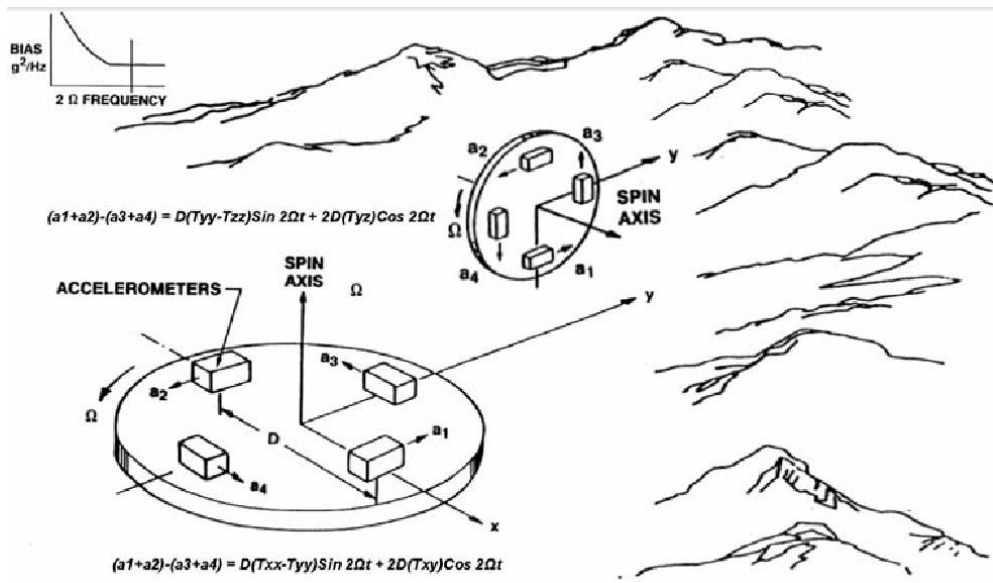


Figure 2-15: Air-FTG instrument (Murphy 2004)

The data processing of the Air-FTG includes five steps, as shown in Table 2-1 (Murphy 2004). The Air-FTG noise has been reported as “3.5 Eötvös RMS filtered to an 800 m wavelength” and corresponds to noise density of $13 \text{ Eötvös}/\sqrt{Hz}$ (Dransfield 2007).

Table 2-1: Data processing of Air-FTG data

Steps	Tasks
Acceleration compensation	<ul style="list-style-type: none">• Correction for centrifugal forces due to spinning disk• Self-gradient correction because of the aircraft motion and drainage of fuel• Correction for acceleration acting on the instrument
Demodulation of data	<ul style="list-style-type: none">• Re-sampling the data to 0.5 Hz• Extraction of individual tensor element• Transformation from body frame to Earth fixed frame
Post mission processing	<ul style="list-style-type: none">• Line correction for GGI drift• Head errors correction by using differential corrected GPS data and inertial navigation data• Levelling and micro levelling procedures• De-noising procedure
Other corrections	<ul style="list-style-type: none">• Terrain correction
Interpretation	<ul style="list-style-type: none">• Interpretation routine

2.4.3 The University of Western Australia Superconductive Gravity Gradiometer (UWA-SGG)

The University of Western Australia superconductive gravity gradiometer (UWA-SGG) is a type of OQR gradiometer designed at the University of Maryland under the supervision of Ho Jung Paik (see Chan and Paik (1987) and Moody and Paik (2007)). A detailed explanation about the mechanical and electrical components of the OQR gradiometer have been reported by Matthews (2002). The sensitivity of the gradiometer output to many error sources due to the operation of the system in a non-inertial reference frame was also discussed comprehensively.

According to the Matthews (2002), angular and translational accelerations of the platform are the two major error contributions in the output of the gradiometer in a non-inertial frame. Additionally, another error source known as sensitivity of the instrument to the temperature fluctuations of the environment was explained. Dynamic error contributions to the gradient sensitivity of the OQR are listed in Table 2-2. As can be seen from this table, the translational effects are larger in magnitude than the angular acceleration effects. Noise performance below the 1 Eötvös level in the laboratory situation was reported. This performance is good for the detection of typical ore bodies such as silver, gold, copper, zinc, iron, and so on (Matthews 2002).

Table 2-2: Dynamic error contributions to the gradient sensitivity in the OQR for responder A (Matthews 2002)

Error terms		Equivalent gradient error (Eötvös)
Angular acceleration effects	Misalignment of axes	2.7
	Angular velocity	-1
	Angular acceleration	-1.25e+04
Translational acceleration effects	Residual dipole mass	6.5e+04
	Induced dipole pivot S-bend	2e+04
	Induced dipole pivot stretch	-810
	Induced dipole bar stretch	7.5
	Induced dipole bar bending	-45.5
	Induced dipole bar shear	10

2.4.4 The Gedex High-Definition Airborne Gravity Gradiometer (Gedex HD-AGGTM)

The Gedex high-definition airborne gravity gradiometer (HD-AGGTM) instrument, similar to the UWA-SGG, is an OQR type gradiometer designed at the University of Maryland. The difference is in the different methodologies used to enhance the signal-to-noise ratio of the gradiometer. The target noise performance for the Gedex HD-AGGTM is 1 Eötvös, which is suitable for detection of geophysical features with 50-100 m spatial resolution (Carroll et al., 2010a). Because this is the system used in this thesis, detailed explanation about the Gedex system is provided separately in Chapter 3.

2.5 Summary

Since the major instruments used for this thesis are both the superconductive angular accelerometer and the superconductive angular gradiometer, it was necessary to discuss the principles, measurements and measurements errors of these instruments in this chapter. The superconductive translational accelerometer and specific force gradiometer were also introduced briefly in this chapter. At the end of the chapter, four industrial airborne gradiometers – Falcon®, Air FTG, UWA-SGG, and Gedex HD-AGGTM – were discussed. However, a more detailed explanation of the Gedex HD-AGGTM system (the major focus of this thesis) will be presented in Chapter 3.

Chapter 3: Gedex High-Definition Airborne Gravity Gradiometer (Gedex HD-AGG™)

Gedex HD-AGG™ instrument is the OQR type responder, which was designed at the University of Maryland. The mechanical and electrical design of the system and the errors introduced in the output of the system are similar to what is stated for the OQR type gradiometer in Chapter 2. Since the focus of this thesis is the Gedex HD-AGG™ instrument along with its auxiliary sensors, and because Gedex provided insufficient written document about this system and its operation the following points for this system needed to be clarified by the author and are discussed in this chapter:

- 1- What is the working principle behind the Gedex HD-AGG™?
- 2- What are the different reference frames used in this work?
- 3- What are the measurements of the Gedex HD-AGG™ and how are they produced?
- 4- What are the noise terms in the output of the Gedex HD-AGG™?
- 5- What are the auxiliary sensors that accompany the Gedex HD-AGG™? What is the role of these auxiliary sensors in error compensation of the gradiometer output?
- 6- What are the error sources of the two major components of the gradiometer: the superconductive translational and angular accelerometers?
- 7- What is the company's proposed method to remove the errors in the output of the superconductive translational and angular accelerometers?

3.1 Working principle of the Gedex HD-AGG™

Gedex's instrument is a type of OQR gradiometer that includes pairs of superconductive angular accelerometers with a common rotation axis. A detailed explanation about the working principles of this kind of system was given in Chapter 2. As can be seen from Figure 3-1, the gradiometer output can be in either common mode acceleration or differential mode acceleration. The former happens when the two test masses are rotating in the same direction because of the platform

acceleration and the latter happens when the two test masses are rotating in opposite direction due to a nearby gravity gradient from a density anomaly (Carroll et al., 2010a).

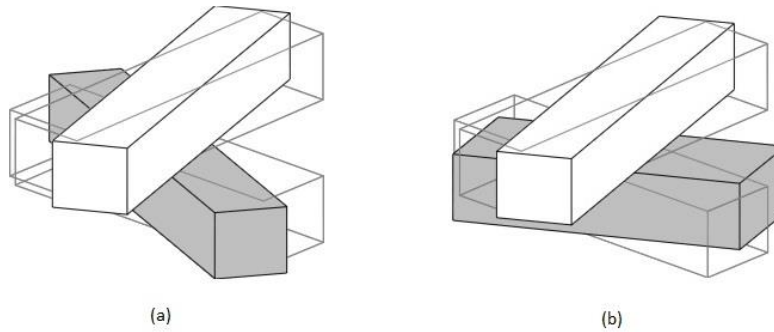


Figure 3-1: General principle of the Gedex HD-AGGTM instrument: (a) differential mode acceleration and (b) common mode acceleration (Matthews 2002)

Similar to the OQR type gradiometer explained in Chapter 2, two superconductive translational and angular accelerometers supplement the Gedex HD-AGGTM system on a moving platform during data acquisition operations. The configuration of the Gedex system with these superconductive sensors is depicted in Figure 3-2.

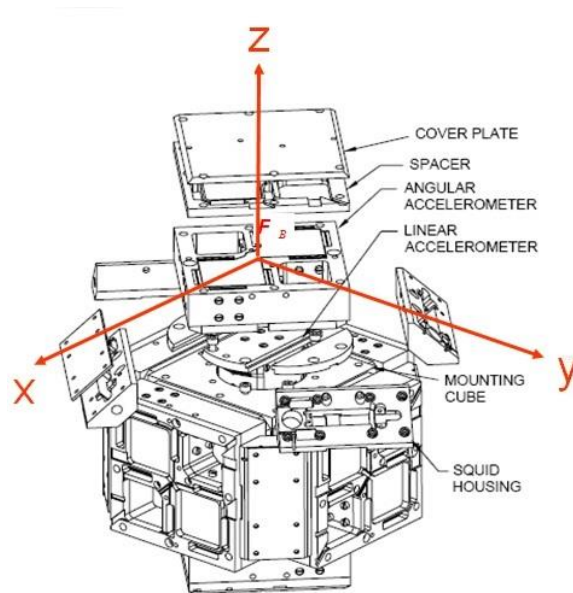


Figure 3-2: Configuration of the Gedex HD-AGGTM with superconductive translational and angular accelerometers (Carroll et al., 2010a)

Available information and data for this thesis is related to a single axis, the z-axis, of the instrument as depicted in Figure 3-2. The visible angular responder is one of the two z-axis OQR responders and the other one is at the bottom of the cube. These two angular accelerometers are coupled through the mode splitting procedure and are responsible to measure the differential mode or common mode accelerations. In the coupled system, the motion of one accelerometer will make torques on the second accelerometer. The mode-splitting is usually a setup that helps the differential mode to remain close to 7 Hz, while the common mode appears at a higher frequency, generally above 10 Hz. As can be seen from Figure 3-2, two other superconductive angular accelerometers are installed on each of the x and y faces of the cube to measure the horizontal angular accelerations. The visible superconductive translational (linear) accelerometer is the z-axis responder, which is placed into the cube, and is shown flipped-over in this figure. Two other superconductive translational accelerometers are also inserted into one of the x and y faces in a similar way for measuring horizontal translational accelerations and are not visible in this figure. All of the superconducting accelerometers and sensing circuitry with SQUID (which is also superconducting) are integrated onto the cube. The voltage signal produced by the SQUID is wired to the outside of the cryogenic vessel for measurement. The gradiometer cube is tightly packaged with all these responders very close to each other and as rigidly as possible. The total output of this tight package are the differential mode accelerations, common mode accelerations, and horizontal angular accelerations, which are all in rad/s^2 . The translational accelerations in z-axis and horizontal axes are measured in m/s^2 . The way that the differential mode accelerations are measured in the Gedex HD-AGGTM are similar to the UWA's gradiometer. That is, the detected currents by the SQUID in case of any anomaly test are proportional to the difference between the angular deflections of each angular accelerometer. However, the way the common mode accelerations are measured is different in the Gedex system. In the UWA system, the detected currents by SQUID are proportional to the summing and/or averaging of the two angular deflections of a coupled angular accelerometers (Matthews 2002, Moody 2011, Moody and Paik 2007). However, for the Gedex gradiometer it was more economical to make a pair of superconductive angular accelerometers coupled and then use only the output of one of them as the common mode acceleration.

What was mentioned in above paragraphs about common and differential mode measurements is valid only in theory. The fact is that differential and common mode accelerations contain other unwanted signals in practice. Figure 3-3 shows the different modes measured in the Gedex system in practice.

It is often the case that the differential mode is contaminated with some portion of the common mode accelerations. In addition, since each individual angular accelerometer includes quadratic non-linearity (squared angular velocity) in their output, the differential mode will be contaminated with this effect, as well. As was mentioned in Chapter 2, it is the duty of CMRR to minimize the interjection of common mode to differential mode to some extent. However, the quadratic non-linearity will remain even after applying the CMRR. Therefore, firstly, it is required to do three-axis rotational stabilisation of the gradiometer and secondly it is necessary to apply some post processing to remove the residual part of this effect (Matthews 2002).

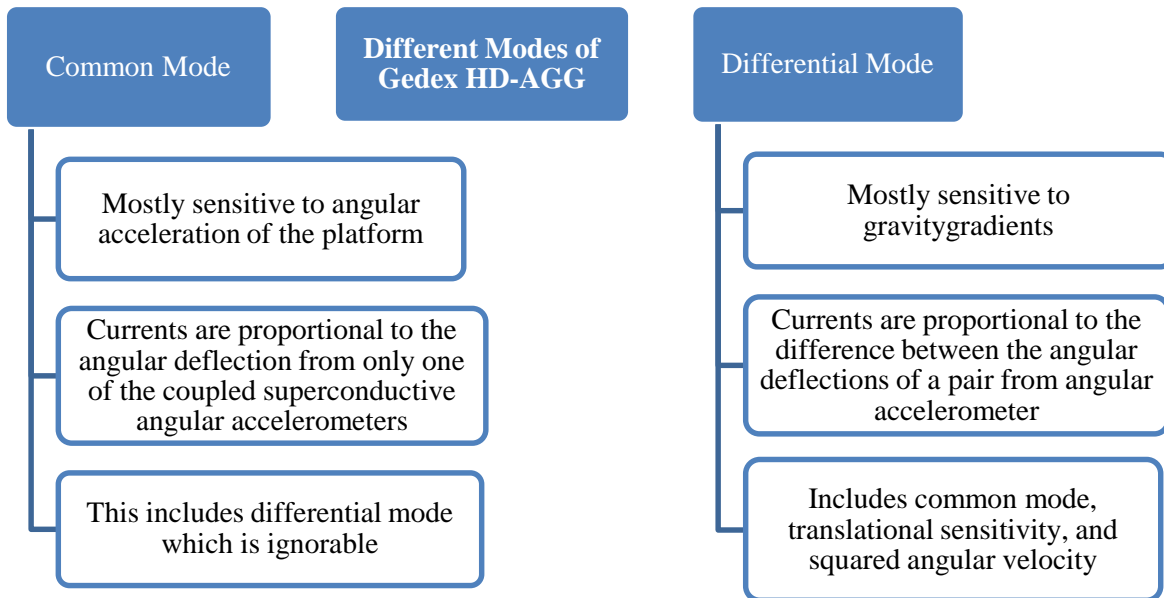


Figure 3-3: The Gedex HD-AGG™ measurements in practice

Furthermore, there are some torques adding to the output of each individual angular accelerometer as a result of the translational movement of the platform. Thus, the angular gradiometer output will not only be contaminated with common mode accelerations and quadratic non-linearities, but also with translational effects. As was mentioned in Chapter 2, it is the duty of LMRR to minimize the effect of translational sensitivities on the gradiometer output. There will also remain some residual contamination due to translational effects, which can be removed in post processing. Just like the gradient mode which is not completely a gradient signal, the common mode output is not only the angular accelerations, but mixed with some portion of the differential mode. However, this differential effect is very small in magnitude and can be ignored from the common mode output.

3.1.1 Gedex HD-AGGTM configuration with auxiliary sensors

Somewhat analogous to other gradiometer systems, the performance of the Gedex system will be limited by aircraft vibrations. In order to improve the signal to noise ratio, Gedex HD-AGGTM is accompanied by some major components during the operation. These components are superconductive angular and translational accelerometers, a Qflex accelerometer, an Applanix IMU, temperature sensitivity recorders, a cryostat, and a motion isolation controller. The instrument configuration is depicted in Figure 3-4. The role of all these auxiliary sensors is to help compensate the gradiometer output for the many error sources that were previously explained for the OQR type gradiometer in Chapter 2. The sources of the errors are mainly temperature, mechanical, electronic and kinematic vibrations. For example, the cryostat is not only used to mechanically support the gradiometer cube, but it is also responsible to preserve a temperature at 5K during the operation. The motion isolation controller is responsible to minimize any translational and angular accelerations of the platform due to airplane movements. Moreover, it is responsible to minimize the effect of angular velocities squared (Carroll et al., 2010a). Temperature fluctuations measured during the operation can also be post processed to remove any residual low frequency error in the output of the gradiometer.

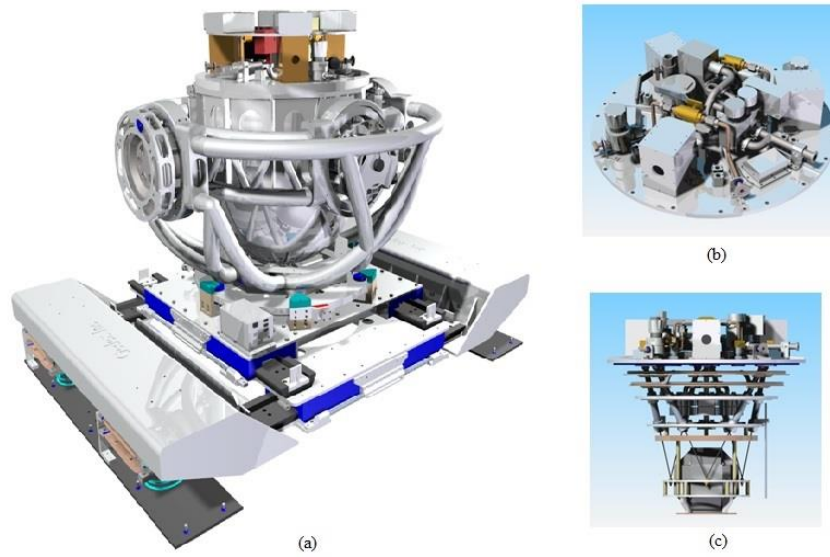


Figure 3-4: Major components of the Gedex HD-AGG™. (a) Motion isolation instrument plus the cryostat. (b) Inertial instruments including Applanix IMU and Qflex accelerometers on the top of the instrument. (c) Gedex HD-AGG™ cube configuration with inertial instruments on the top (provided by Gedex)

Inertial instruments are assumed to provide a bias free output, which can be again used in the post processing mode to compensate for the bias drift in the output of the superconductive angular accelerometers and gradiometer. It will be explained at the end of this chapter how a linear regression is used by Gedex to compensate the angular accelerometer output for the translational and temperature fluctuations using the output of auxiliary sensors.

3.1.2 Reference frames used in the Gedex system

The reference frames used for the Gedex system are divided into three categories: Aircraft frame F_{AC} , platform frame F_{IMU} and gradiometer frame F_G . These reference frames and also the local level frame F_L are illustrated in Figure 3-5. The aircraft frame F_{AC} is defined as a Roll-Pitch-Yaw frame of the aircraft body. The platform frame F_{IMU} is defined as the Applanix IMU frame, which is mounted on the top of the isolation platform. The isolation platform helps separate the gradiometer output from the translational and angular motions of the aircraft during the operation.

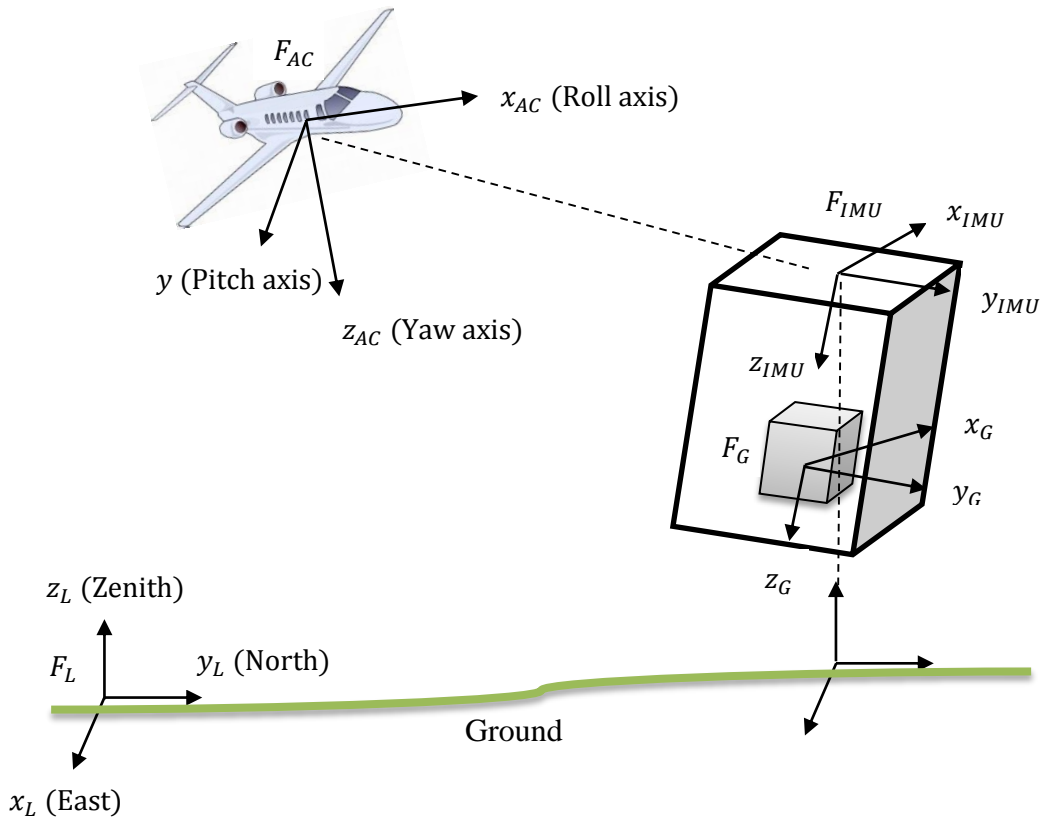


Figure 3-5: Different reference frames used in the Gedex system

Platform position and attitude is essentially the same as the aircraft. That is why the z -axis of F_{IMU} is selected to be downwards. The attitude of the aircraft frame F_{AC} is changing over time whereas the attitude of the platform frame F_{IMU} is controlled to stay constant over time. From the local frame perspective, the aircraft frame rotates with near-constant attitude around the IMU platform. The x and y axes of F_{IMU} are defined along the symmetry axes of the responder. The gradiometer frame F_G is located at the center of the gradiometer cube (the smaller cube in the center of the isolation platform). It is fixed to the platform and its axes are parallel to the platform frame F_{IMU} (McTavish 2014).

3.2 OQR measurements in the Gedex system

The OQR type gradiometers can measure either the differential mode or common mode accelerations. The mathematical expressions for this kind of gradiometer are explained in the following sub-sections. A single angular accelerometer system equation will be written first and then it will be generalized to the equations of a pair of angular accelerometers.

3.2.1 Measurement of a single superconductive angular accelerometer

The output of the superconductive angular accelerometer can be recorded either with respect to standard axis view F or principal axis view F' . The standard axis view F is orthogonal to the gradiometer cube while the principal axis view F' is by design rotated 45 degree with respect to standard axis view. Both of these frames are depicted in Figure 3-6.

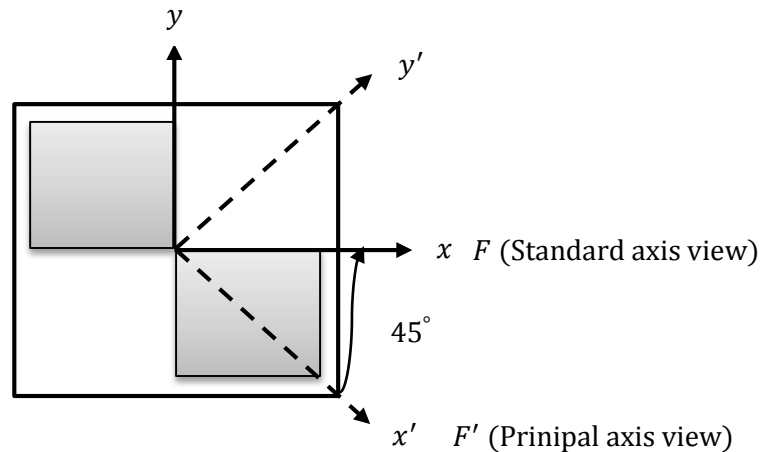


Figure 3-6: A single superconductive angular accelerometer in standard and principal axes views

By considering the equation of the angular motion for a single angular accelerometer, Equation (2-28), the output of the angular accelerometer rotating about the z-axis can be written in standard axis view as follows:

$$I_{zz}\dot{\Omega}_z = \tau_z - I_{xy}[(\Gamma_{yy} - \Gamma_{xx}) + (\Omega_x^2 - \Omega_y^2)] \quad (3-1)$$

And in the principal axis view it can be written as follows:

$$I'_{zz}\dot{\Omega}'_z = \tau'_z + (I'_{yy} - I'_{xx})(\Gamma'_{xy} - \Omega'_x\Omega'_y) \quad (3-2)$$

Either Equation (3-1) or Equation (3-2) can be used to write equations of angular motions for a coupled angular accelerometer.

3.2.2 Measurements of a pair of superconductive angular accelerometers

Figure 3-7 illustrates the pair of superconductive angular accelerometer as seen from the x face of the OQR gradiometer. In this figure, $\tau_{A(G)}$ and $\tau_{B(G)}$ are torques experienced by responders (accelerometers) A and B, respectively, in the gradiometer frame.

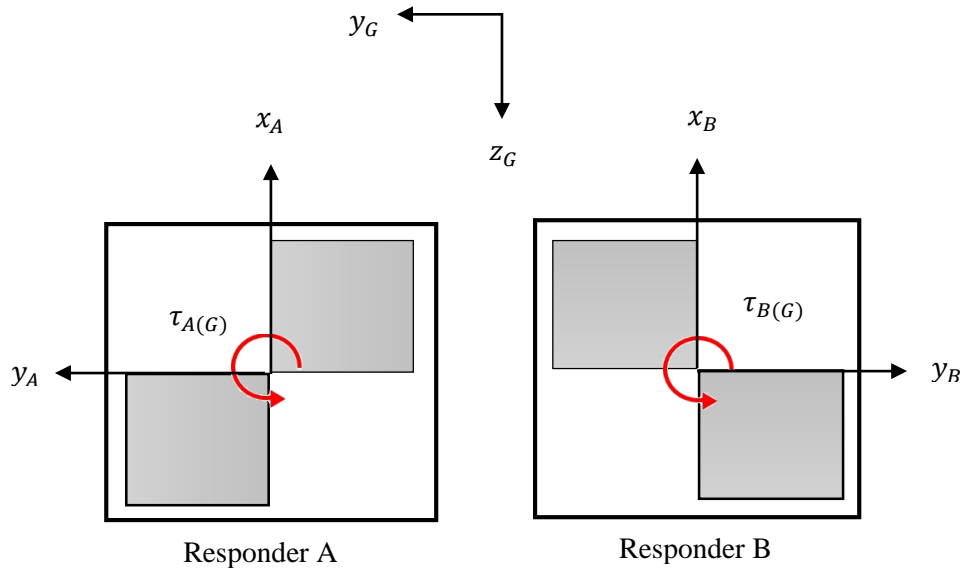


Figure 3-7: A coupled superconductive angular accelerometers (x-axis OQR)

Assuming standard axis view and using Equation (3-1), equations of angular motion for each half of the x-axis OQR gradiometer are written as follows (McTavish 2014):

$$\begin{cases} I_{zz,A}\dot{\Omega}_z(A) = \tau_{z,A(A)} - I_{xy,A}[(\Gamma_{yy(A)} - \Gamma_{xx(A)}) - (\Omega_y^2(A) - \Omega_x^2(A))] \\ I_{zz,B}\dot{\Omega}_z(B) = \tau_{z,B(B)} - I_{xy,B}[(\Gamma_{yy(B)} - \Gamma_{xx(B)}) - (\Omega_y^2(B) - \Omega_x^2(B))] \end{cases} \quad (3-3)$$

The symbols used in this equation, all defined in Chapter 2, are inertial moment I , torque τ , yy and xx components of gradient Γ_{yy} and Γ_{xx} , angular accelerations $\dot{\Omega}$, and angular velocity squared in y and x directions, Ω_y^2 and Ω_x^2 . Subscripts A and B in parenthesis includes measurements from responders A and B, respectively. It is noteworthy that the angular velocities seen in the gradiometer and responders frames are the same.

Before summing or differencing the torques in Equations (3-3), it is required to transform these equations from the responder's A and B frames to the gradiometer's frame. The configuration of the x -axis OQR gradiometer with its coupled z -axis angular accelerometers is depicted in Figure 3-8. It can help define rotation matrices for this transformation. It is obvious from Figure 3-8 that the transformation matrices from the gradiometer frame to each responder frame are as follows:

$$C_{GA} = \begin{bmatrix} 0 & 0 & 1 \\ 0 & 1 & 0 \\ -1 & 0 & 0 \end{bmatrix} \quad (3-4)$$

$$C_{GB} = \begin{bmatrix} 0 & 0 & -1 \\ 0 & -1 & 0 \\ -1 & 0 & 0 \end{bmatrix} \quad (3-5)$$

Using Equation (3-4) and Equation (3-5), all parameters Ω , Γ , $\dot{\Omega}$, and τ in Equations (3-3) can be transformed into the gradiometer frame. Therefore, Equations (3-3) can be rewritten as:

$$\begin{cases} I_{zz,A}\dot{\Omega}_x(G) = \tau_{x,A(G)} - I_{xy,A}[(\Gamma_{yy(G)} - \Gamma_{zz(G)}) - (\Omega_y^2(G) - \Omega_z^2(G))] \\ -I_{zz,B}\dot{\Omega}_x(G) = -\tau_{x,B(G)} - I_{xy,B}[(\Gamma_{yy(G)} - \Gamma_{zz(G)}) - (\Omega_y^2(G) - \Omega_z^2(G))] \end{cases} \quad (3-6)$$

The torque equations can be written as follows:

$$\begin{cases} \tau_{x,A(G)} = I_{zz,A}\dot{\Omega}_x(G) + I_{xy,A}[(\Gamma_{yy(G)} - \Gamma_{zz(G)}) - (\Omega_y^2(G) - \Omega_z^2(G))] \\ \tau_{x,B(G)} = I_{zz,B}\dot{\Omega}_x(G) - I_{xy,B}[(\Gamma_{yy(G)} - \Gamma_{zz(G)}) - (\Omega_y^2(G) - \Omega_z^2(G))] \end{cases} \quad (3-7)$$

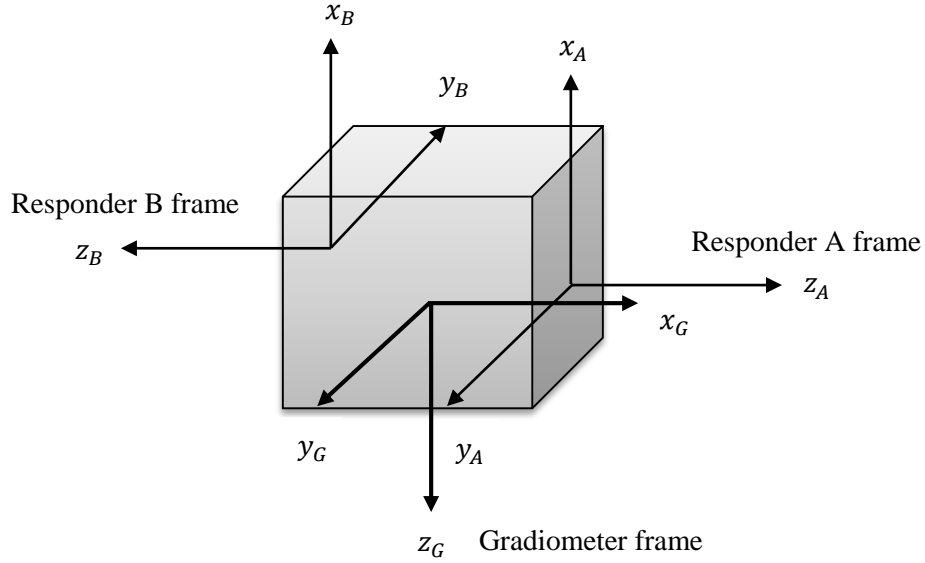


Figure 3-8: Configuration of the x-axis OQR gradiometer with its coupled z-axis angular accelerometers

The gradiometer measures the torque difference $\Delta\tau = \tau_{x,A(G)} - \tau_{x,B(G)}$ given by the equation:

$$\Delta\tau = (I_{xy,A} + I_{xy,B})[(\Gamma_{yy(G)} - \Gamma_{zz(G)}) - (\Omega_{y(G)}^2 - \Omega_{z(G)}^2)] + (I_{zz,A} - I_{zz,B})\dot{\Omega}_{x(G)} \quad (3-8)$$

For an ideal responder, $I_{xy,A} = I_{xy,B}$ and $I_{zz,A} = I_{zz,B}$, the x-axis gradiometer measures the torques difference as:

$$\Delta\tau = (2I_{xy,A})[(\Gamma_{yy(G)} - \Gamma_{zz(G)}) - (\Omega_{y(G)}^2 - \Omega_{z(G)}^2)] \quad (3-9)$$

The gradiometer also measures the sum of torques $\Sigma\tau = \tau_{x,A(G)} + \tau_{x,B(G)}$ as follows:

$$\Sigma\tau = (I_{xy,A} - I_{xy,B})[(\Gamma_{yy(G)} - \Gamma_{zz(G)}) - (\Omega_{y(G)}^2 - \Omega_{z(G)}^2)] + (I_{zz,A} + I_{zz,B})\dot{\Omega}_{x(G)} \quad (3-10)$$

For an ideal responder, $I_{xy,A} = I_{xy,B}$ and $I_{zz,A} = I_{zz,B}$, the x-axis gradiometer measures the torques sum as:

$$\Sigma\tau = 2I_{zz,A}\dot{\Omega}_{x(G)} \quad (3-11)$$

Eventually, gradient components (derived from the torque difference equations) and angular accelerations (derived from the torque sum equations) in standard axes view F can be computed using the following equations:

$$(\Gamma_{yy(G)} - \Gamma_{zz(G)}) = \frac{\Delta\tau}{2I_{xy,A}} - (\Omega_{y(G)}^2 - \Omega_{z(G)}^2) \quad (3-12)$$

$$\dot{\Omega}_{x(G)} = \frac{\sum \tau}{2I_{zz,A}} \quad (3-13)$$

Since the standard axis view will be used throughout the rest of this thesis, deriving the same equations for the principal axis view is ignored.

There are some assumptions underlying the theoretical derivation of all these equations. For example, the two angular accelerometers are identical in their mechanical and electrical design. Most importantly, they have the same frequencies in order for the SQUID to be able to detect the differential displacements of the test masses. However, having identical responders is not possible in practice. That is the inertias are never perfectly balanced, there are different frequencies for each responder, and there is a small rotation of each responder's pivot axis relative to the gradiometer cube. Considering these problems, the theoretical system equation derived for gradiometer output is no longer valid for use in practice (McTavish 2014). Since there is not enough information and data for the OQR measurements in practice, only the theoretical system equations are used in this thesis.

3.3 Noise terms definition in the Gedex HD-AGGTM system

Errors in the output of the Gedex HD-AGGTM are similar to what was mentioned in Section 2.3.2 for the OQR type gradiometer. A different point regarding the Gedex system is its auxiliary sensors that accompany the gradiometer system during operation. As was explained in Section 3.1, the Gedex system is accompanied by superconductive angular and translational accelerometers and by some inertial sensors such as the Qflex accelerometers and the Applanix IMU. The purpose for using the superconductive angular and translational accelerometers is to model the dynamic

vibration of the platform from the gradiometer output. However, both superconductive accelerations are noisy and this can limit the final performance of the gradiometer channel. Therefore, it is required to examine the error sources and error removal procedures of these two sensors before correcting the gradiometer output. This is explained in Sections 3.4 and 3.5.

3.4 Noise terms definition in the superconductive translational accelerometer

By describing the measurement procedure of the superconductive translational accelerometer, it is possible to understand at which stage the errors are introduced into the translational acceleration signal. The way the superconductive translational accelerometer measures acceleration in m/s^2 is depicted in Figure 3-9. Everything begins with the acceleration of the housing a_x in m/s^2 . The first error term, caused by the superconductive temperature fluctuations B_1T_1 , is added to a_x and noisy acceleration \tilde{a}_x is produced. Then \tilde{a}_x is convolved with the system transfer function h_{ax} in s^2 to create the test mass displacement Δx in m . The transfer function h_{ax} is precisely determined by the Gedex team through a calibration test. After that, the displacement signal goes into the electrical part and multiplied by a scale factor A_1 in V/m to create the voltage v in V . At this level, errors due to electrical temperature fluctuations denoted by B_2T_2 and B_3T_3 are adding to the voltage. Then the noisy voltage is multiplied by the inverse scale factor $1/A_1$ in m/V to produce the test mass displacement Δx in m . Finally, the test mass displacement is multiplied by the inverse transfer function h_{ax}^{-1} in $1/s^2$ to generate the output of the superconductive translational accelerometer in m/s^2 .

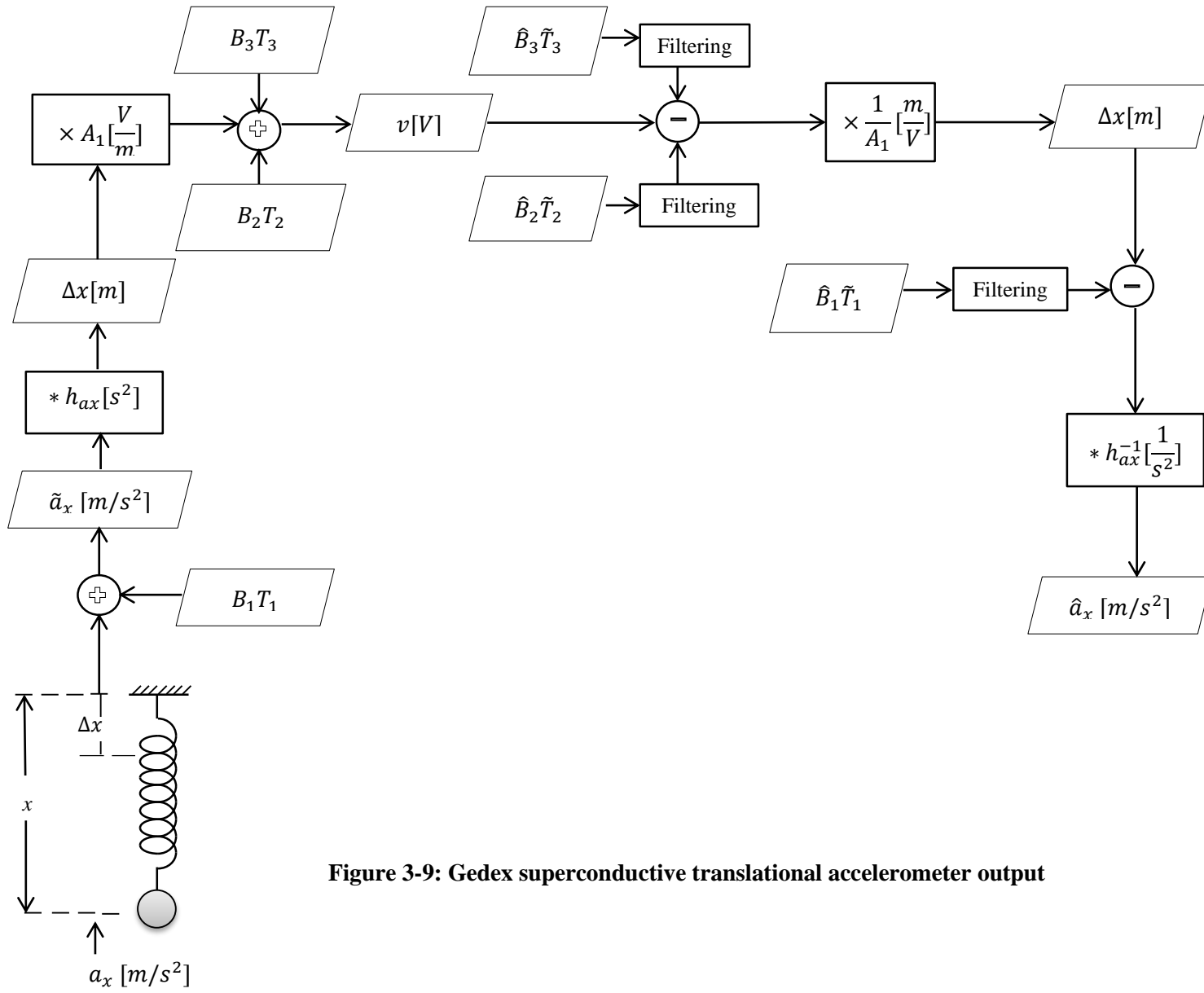


Figure 3-9: Gedex superconductive translational accelerometer output

The following notation was used in Figure 3-9 (rectangle used for function and rhomboid used for measurement):

a_x	: Acceleration of the housing in m/s^2
\tilde{a}_x	: Noisy acceleration due to mechanical error
h_{ax}	: 2 nd order transfer function of the translational accelerometer in s^2
Δx	: Relative displacement of test mass w.r.t instrument housing in m
A_1	: Scale factor in V/m
v	: Voltage in V
B_1T_1	: Mechanical temperature error (B1 is regression coefficient and T1 is mechanical temperature in K)
B_2T_2 & B_3T_3	: Electronic temperature error (B2 and B3 are regression coefficients. T2 and T3 are electronic temperatures in K)
$\hat{B}_1, \hat{B}_2, \& \hat{B}_3$: Estimated sensitivity coefficients through calibration in V/K
$\tilde{T}_1, \tilde{T}_2 \& \tilde{T}_3$: Measured temperatures in K

As can be seen from this figure, there is one main error source in the output of the translational accelerometer including electrical and mechanical temperature fluctuations. These temperature errors can be removed from the translational accelerometer output either during the data acquisition procedure or at the end when the output of the accelerometer is ready in m/s^2 . In the first approach, it is required to have access to voltage data, displacement data, and all temperature data to achieve the corrected acceleration as shown with \hat{a}_x in Figure 3-9. In the second approach, it is required to have access to raw translational acceleration in m/s^2 and all temperature data. It is worth mentioning that temperature data is noisy itself and thus before removing this effect from the translational accelerometer it is required to filter the temperature data. That is why there is some filtering in the rectangle shape in Figure 3-9. The Gedex empirical approach for filtering the translational acceleration is the second approach, where the raw data in m/s^2 is filtered with the Butterworth low pass filtering with 1 Hz cut-off frequency. This is explained in details in Section 3.6.

3.5 Noise terms definition in the superconductive angular accelerometer

The way superconductive angular accelerometer measures angular acceleration in rad/s^2 is depicted in Figure 3-10. Everything starts with the acceleration of the housing $\dot{\Omega}_x$ in rad/s^2 . The first error term $B_{1\dot{\Omega}_x}T_{1\dot{\Omega}_x}$ is the mechanical error corresponding to the temperature fluctuations of the environment adding to the acceleration to create the noisy acceleration $\tilde{\dot{\Omega}}_x$. After that, the noisy acceleration is convolved with transfer function $h_{\dot{\Omega}_x}$ in s^2 to generate angular displacement $\tilde{\Theta}_x$ in rad . This angular displacement not only contains the noise corresponding to mechanical errors, but errors due to the translational acceleration of the platform (static dipole $C_{\dot{\Omega}_x}a_y$ and pivot deformation $E_{\dot{\Omega}_x}\theta_y$) and quadratic non-linearity (angular velocity squared) $D_{\dot{\Omega}_x}\Omega_y^2$. Static dipoles happen when the system center of mass is not at the center of rotation, and pivot deformation happens when the responders are bending over time. These two effects add extra torque to the output of the angular accelerometer. The test mass deformation might be convolved with a transfer function $h'_{\dot{\Omega}_x}$ and then added to displacement. Terms showed with dashed shapes in Figure 3-10 can be ignored in this work. In this figure, the effect of y-axis translational acceleration is only shown. However, all three translational accelerations in x, y, and z directions can contribute to the angular accelerometer output as showed with a_x , a_y and a_z in this figure. After this stage, the noisy angular displacement signal goes in to the electrical part and multiplied by a scale factor $A_{\dot{\Omega}_x}$ in V/rad to create the voltage v in V . At this level, errors due to electrical temperature fluctuations showed by $B_{2\dot{\Omega}_x}T_{2\dot{\Omega}_x}$ and $B_{3\dot{\Omega}_x}T_{3\dot{\Omega}_x}$ are adding to the voltage just like the translational accelerometer case. Then the noisy voltage is multiplied by the inverse scale factor $1/A_{\dot{\Omega}_x}$ in rad/V to produce the angular displacement $\hat{\Theta}_x$ in rad . Finally, the inverse transfer function $h_{\dot{\Omega}_x}^{-1}$ in $1/s^2$ is applied to the angular displacement to generate the output of the superconductive angular accelerometer in rad/s^2 . As can be seen from this Figure 3-10, the output of the superconductive angular accelerometer is sensitive to two major components: temperature fluctuations (both mechanical and electrical) and translational accelerations in the x, y, and z directions. In addition, it is sensitive to the quadratic non-linearity effect (angular velocity squared), which can be ignored in this work.

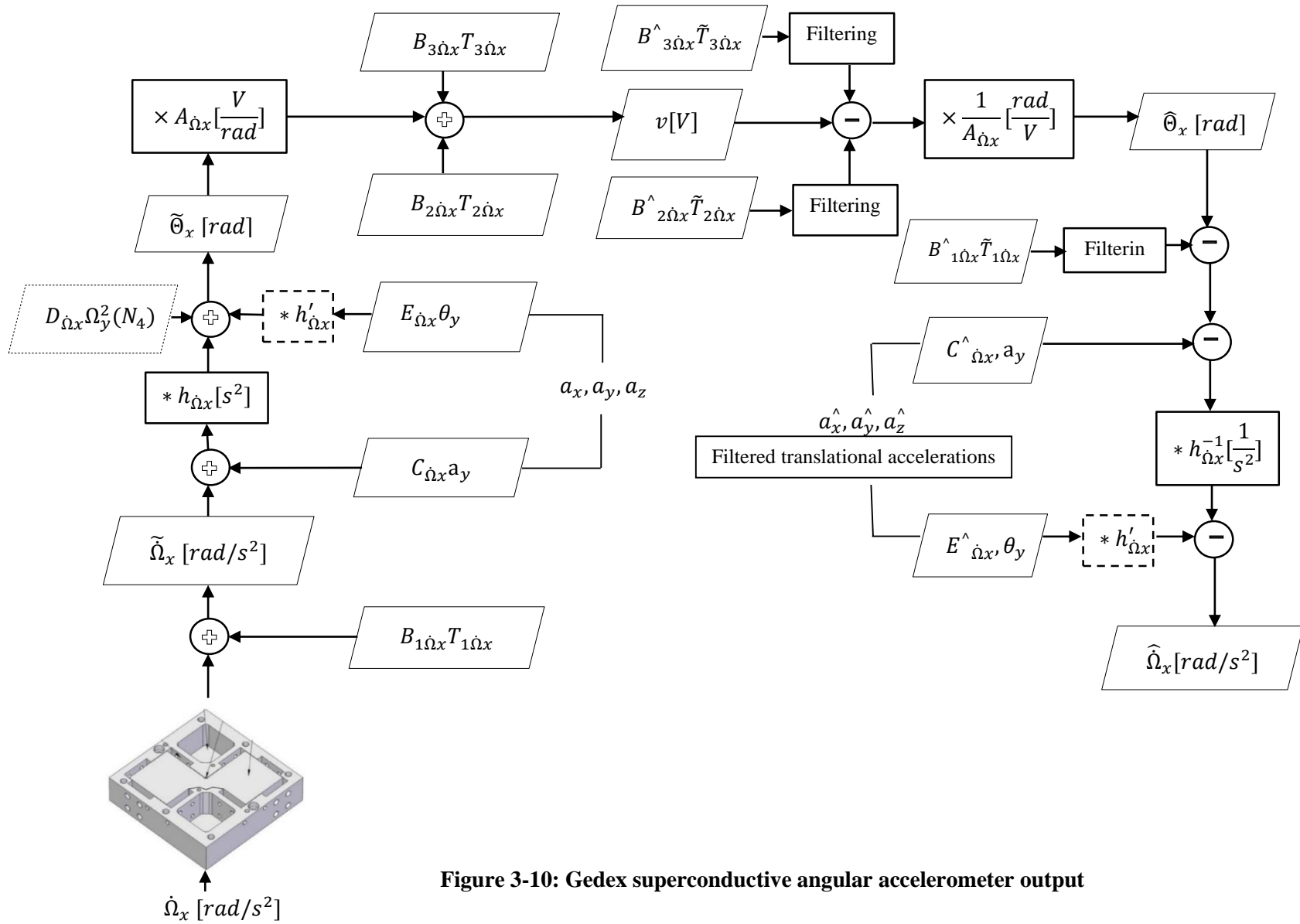


Figure 3-10: Gedex superconductive angular accelerometer output

The following notation was used in Figure 3-10:

$\dot{\Omega}_x$:	Angular acceleration of the housing in rad/s^2
$\tilde{\Omega}_x$:	Noisy acceleration due to mechanical error
$h_{\dot{\Omega}_x}$:	2 nd order transfer function of the angular accelerometer in s^2
$\tilde{\Theta}_x$:	Angular displacement in rad
$A_{\dot{\Omega}_x}$:	Scale factor in V/rad
v	:	Voltage in V
$B_{1\dot{\Omega}_x}T_{1\dot{\Omega}_x}$:	Mechanical temperature error ($B_{1\dot{\Omega}_x}$ is regression coefficient and $T_{1\dot{\Omega}_x}$ is Mechanical temperature in K)
$B_{2\dot{\Omega}_x}T_{2\dot{\Omega}_x}$ & $B_{3\dot{\Omega}_x}T_{3\dot{\Omega}_x}$:	Electronic temperature error ($B_{2\dot{\Omega}_x}$ and $B_{3\dot{\Omega}_x}$ are regression coefficients. $T_{2\dot{\Omega}_x}$ and $T_{3\dot{\Omega}_x}$ are Electronic temperatures in K)
$C_{\dot{\Omega}_x}a_y$:	Static dipole effect ($C_{\dot{\Omega}_x}$ is regression coefficient and a_y static dipole error)
$E_{\dot{\Omega}_x}\theta_y$:	Pivot deformation effect ($E_{\dot{\Omega}_x}$ is regression coefficient and θ_y is pivot deformation error)
$D_{\dot{\Omega}_x}\Omega_y^2$:	Quadratic non-linearity effect ($D_{\dot{\Omega}_x}$ is regression coefficient and Ω_y^2 is quadratic non-linearity error)
$B^{\wedge}_{1\dot{\Omega}_x}, B^{\wedge}_{2\dot{\Omega}_x}$ & $B^{\wedge}_{3\dot{\Omega}_x}$:	Estimated sensitivity coefficients through calibration in V/K
$\tilde{T}_{1\dot{\Omega}_x}, \tilde{T}_{2\dot{\Omega}_x}$ & $\tilde{T}_{3\dot{\Omega}_x}$:	Measured temperatures in K

Similar to the translational accelerometer case these errors can be removed from the angular accelerometer output either during the data acquisition procedure or at the end when the output of the accelerometer is generated in rad/s^2 . In the first approach, it is required to have access to voltage data, angular displacement data, temperature data and translational accelerometer output. The second approach requires access to raw angular acceleration in rad/s^2 , temperature data and translational accelerometer output. It is worth mentioning that both temperature and translational accelerometer output are noisy themselves. Thus, it is necessary to filter these data sets before removing their effect from the angular accelerometer output. That is why the filtering in a rectangle shape is used in Figure 3-10. The temperature and translational sensitivities present themselves as low and high frequency components in the angular accelerometer output. The empirical approaches used by the Gedex team to model these errors are a multiple linear regression and Butterworth low pass filtering procedures, respectively, which are explained in the next section.

3.6 Empirical approaches to remove the errors in the superconductive translational and angular accelerometers

As was stated before, the superconductive angular and translational acceleration are used to compensate for the errors of the angular gradiometer output. However, these superconductive instruments are themselves subject to some error sources, as well. The post processing approach followed by Gedex only focuses on the superconductive angular and translational accelerations rather than the gradiometer channel. In this empirical approach, a multiple linear regression is used to remove low frequency errors in the angular accelerations. Butterworth low pass filtering is applied both to the translational and angular accelerations to reduce the high frequency errors. This assumes that superconductive translational accelerometer output contains only high frequency errors that needed to be removed. However, the superconductive angular accelerometer output contains both low and high frequency errors. This low frequency error, as stated in Section 3.5, is because of three main reasons: sensitivity of the angular accelerometer to translational accelerations (static dipole and pivot deformation), sensitivity of the angular accelerometer to temperature fluctuations inside the cryostat, and sensitivity of the angular accelerometer to quadratic non-linearity (which is ignored in this empirical work). To estimate the low frequency errors of the angular accelerations, the angular accelerometer output is modeled by using six independent parameters in a linear regression equation as follows:

$$\hat{\Omega}_{x,sup} = B_1 \left(\hat{\Omega}_{x,app} \right) + B_2(a_x^{\hat{}}) + B_3(a_y^{\hat{}}) + B_4(a_z^{\hat{}}) + B_5(T_1^{\hat{}}) + B_6(T_2^{\hat{}}) + B_7 \quad (3-14)$$

where in this equation,

- $\hat{\Omega}_{x,sup}$: Filtered superconductive x angular acceleration
- $\hat{\Omega}_{x,app}$: Filtered x angular acceleration derived from the Applanix IMU solution
- $a_x^{\hat{}}$: Filtered x translational acceleration from the Qflex accelerometer
- $a_y^{\hat{}}$: Filtered y translational acceleration from the Qflex accelerometer
- $a_z^{\hat{}}$: Filtered z translational acceleration from the Qflex accelerometer
- $T_1^{\hat{}}$ & $T_2^{\hat{}}$: Filtered mechanical temperatures
- B_1 to B_7 : Regression coefficients

The data sets used for this multiple linear regression came from the four major sensors listed in Table 3-1. The measurements mentioned in Table 3-1 were filtered with the Butterworth low pass filtering at 1 Hz cut-off frequencies and then used in Equation (3-14); they are shown with a hat

upper script in this equation. Also, the Qflex translational accelerometer output was used instead of superconductive translational accelerations because superconductive data was not available for this process. Using all the filtered measurements in Equation (3-14), the regression coefficients can be estimated by linear regression.

Table 3-1: Four major sensors used in the Gedex multiple linear regression approach

Sensor	measurement
Superconducting angular accelerometer	Angular accelerations in x, y, and z directions. Parameter showed by $\dot{\Omega}_{x,sup}$ in Equation (3-14)
Full IMU solution from the Applanix system	Angular velocities in x, y, and z directions in rad/s . Using a spline derivative function, angular accelerations in rad/s^2 were derived from this data set. Parameter showed by $\dot{\Omega}_{x,app}$ in Equation (3-14)
Room-temperature Qflex translational accelerometer	Translational accelerations in x, y, and z directions in m/s^2 . Parameters showed by a_x , a_y and a_z in Equation (3-14)
Cryostat temperature sensor outputs	Two temperature time series in K , showed by T_1 and T_2 in Equation (3-14)

The raw and filtered temperature and translational accelerometer measurements used for this regression are illustrated in Figure 3-11 and Figure 3-12, respectively. Figure 3-13 shows the raw x angular velocity in rad/s and the raw x angular acceleration in rad/s^2 . A spline derivative method is used by the company to derive angular accelerations. Figure 3-14 and Figure 3-15 illustrate both raw and filtered x angular acceleration derived from the Applanix IMU solution and x angular acceleration from the superconductive angular accelerometer with their corresponding PSD.

Regression coefficients as a result of this regression procedure are listed in Table 3-2. Equation (3-14) fit the data with an RMS value of 4.6817e-05.

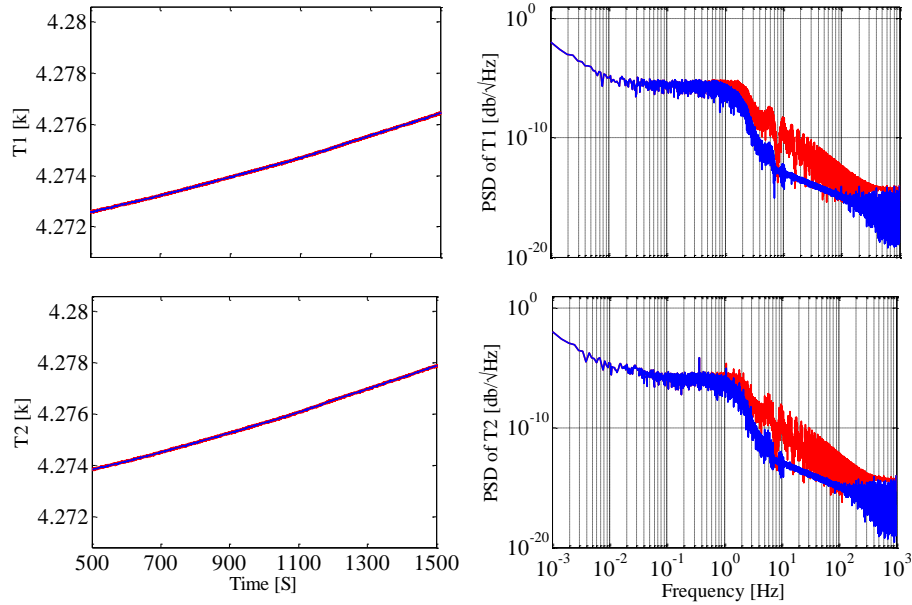


Figure 3-11: Raw (red line) and filtered (blue line) temperature data in K along with their PSD (Provided by Gedex)

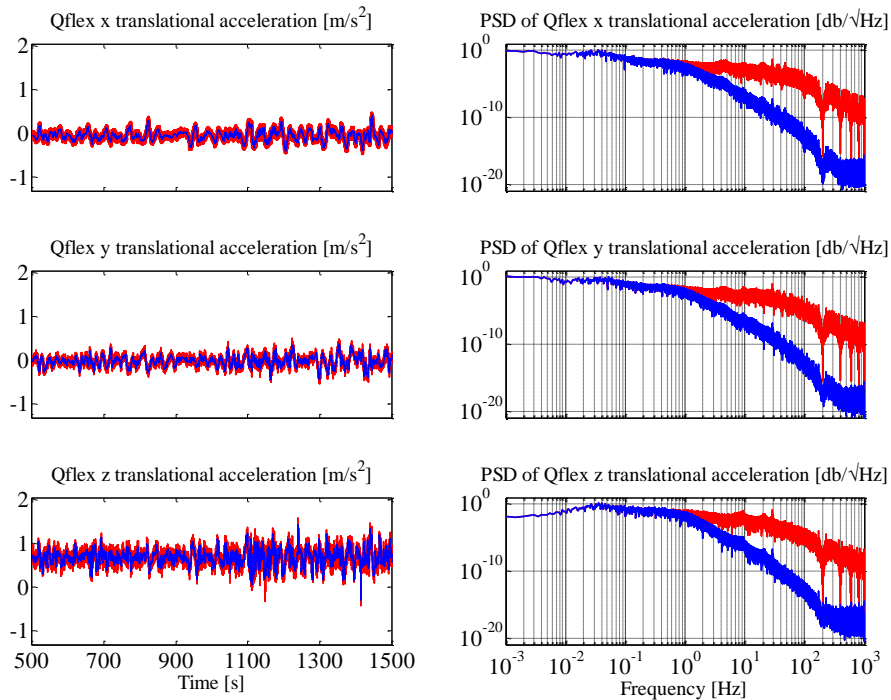


Figure 3-12: Raw (red line) and filtered (blue line) x, y, and z translational accelerations from Qflex accelerometer along with their PSD (Provided by Gedex)

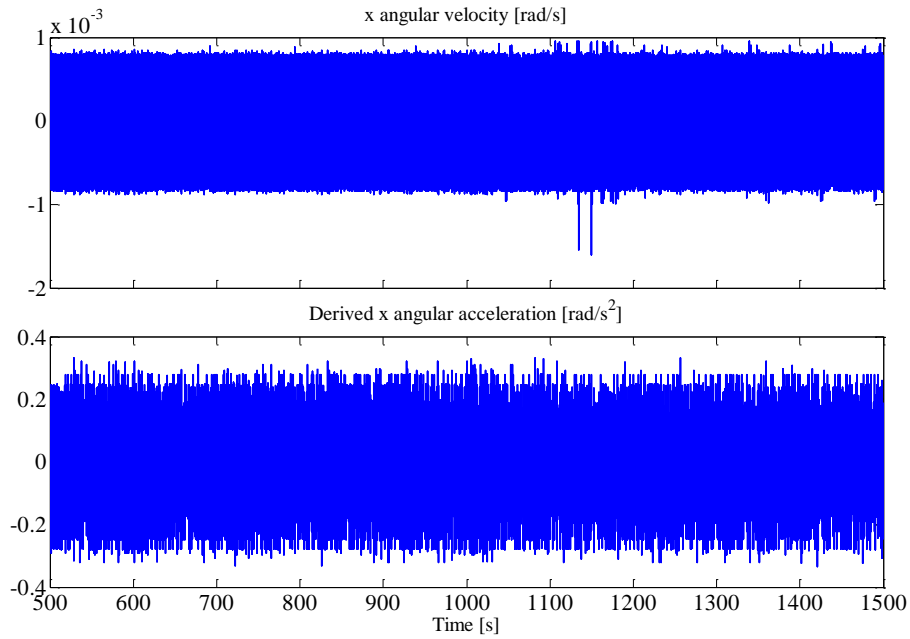


Figure 3-13: Raw x angular velocity from Applanix solution and derived x angular acceleration using spline derivative function (Provided by Gedex)

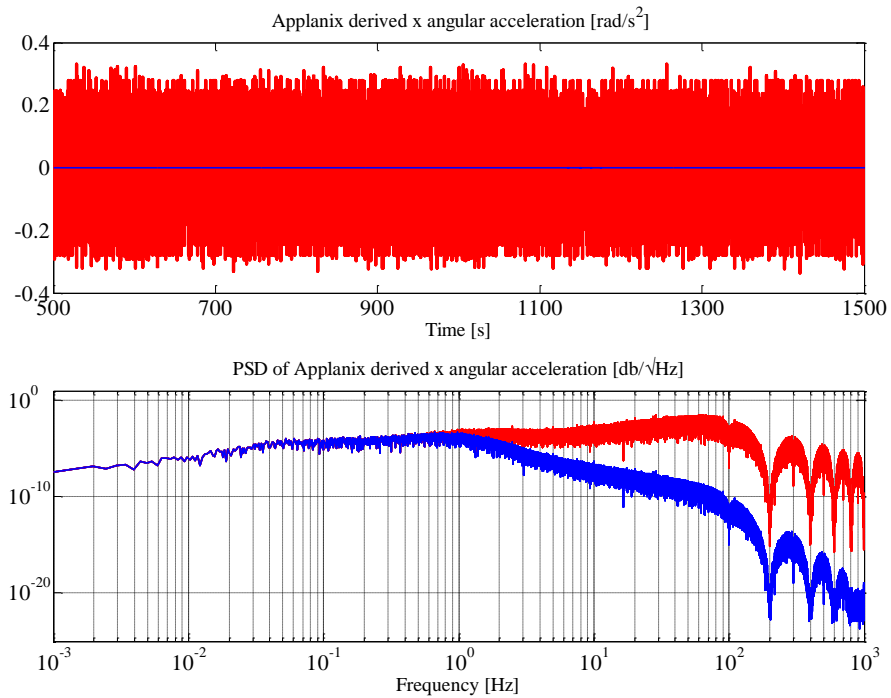


Figure 3-14: Raw (red line) and filtered (blue line) x angular acceleration derived from the Applanix solution along with its PSD (Provided by Gedex)

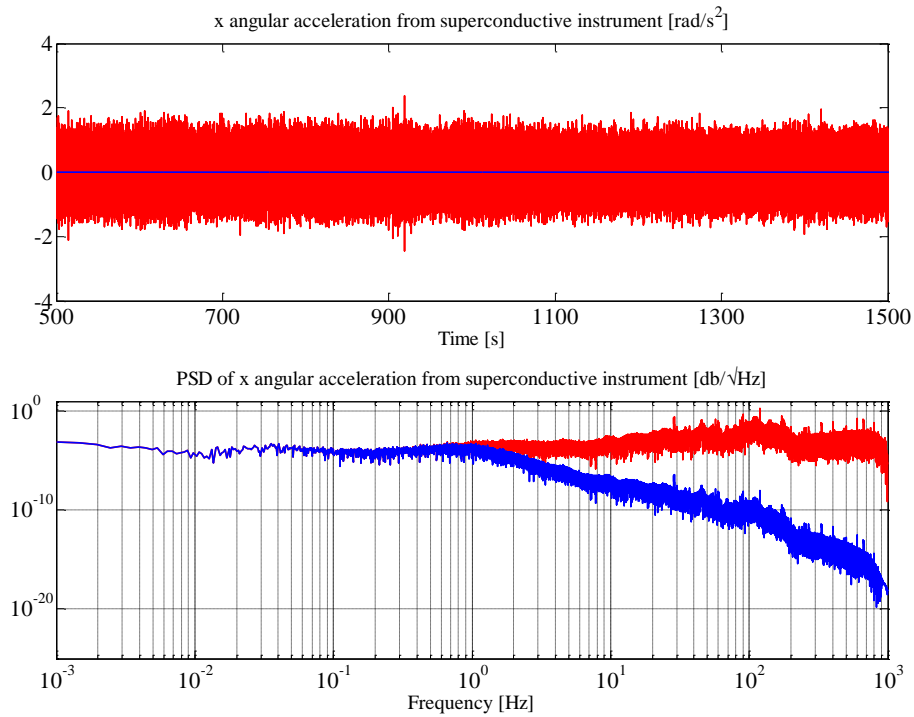


Figure 3-15: Raw (red line) and filtered (blue line) x angular acceleration from the superconductive angular accelerometer along with its PSD (Provided by Gedex)

Table 3-2: Regression coefficients estimated as a result of multiple linear regression with filtered measurements

Regression Coefficient	Magnitude
B_1^{\wedge}	0.9713
B_2^{\wedge}	-1.3552e-04
B_3^{\wedge}	-2.1951e-04
B_4^{\wedge}	3.2733e-04
B_5^{\wedge}	-0.9054
B_6^{\wedge}	0.8511
B_7^{\wedge}	0.2307

Once the regression coefficients are estimated, the low frequency error can be calculated by multiplying the estimated regression coefficients by the raw data as:

$$Low\ frequency\ error = B_2^{\wedge}(a_x) + B_3^{\wedge}(a_y) + B_4^{\wedge}(a_z) + B_5^{\wedge}(T_1) + B_6^{\wedge}(T_2) + B_7^{\wedge} \quad (3-15)$$

The role of angular acceleration derived from the Applanix IMU solution in this regression model is to estimate the bias error in the output of the superconductive angular accelerometer. The bias term in this regression model is the B_7 coefficient. It is assumed that the Applanix IMU solution can provide a bias-free angular acceleration, although it is not as accurate as the superconductive angular acceleration in higher frequencies. Figure 3-16 shows the raw angular acceleration, the calculated low frequency, and the raw angular acceleration when the low frequency error is removed from the data. There is only a small difference between the raw data and the raw data after removing the low frequency error.

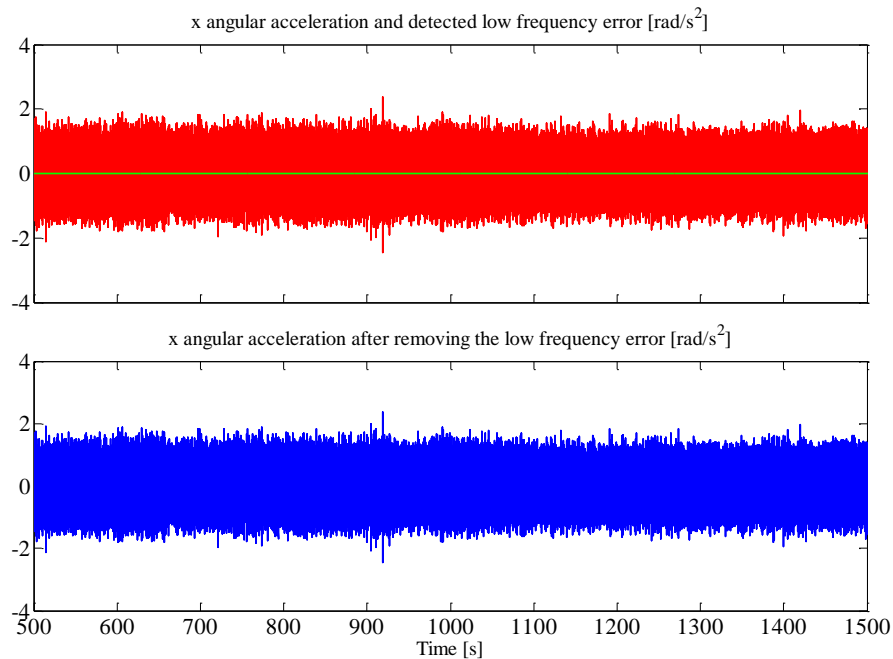


Figure 3-16: The top figure is raw angular acceleration (red line) and detected low frequency error (green line). The bottom figure is angular acceleration after removing the low frequency error (Provided by Gedex)

After removing the low frequency error from the raw angular acceleration, the remaining error represents the high frequency behaviour. For removing the high frequency fluctuations the Butterworth low pass filter with 1 Hz cut-off frequency is used. The raw angular acceleration, the angular acceleration after removing the high and low frequency errors, and the filtered Applanix

x angular acceleration with the Butterworth low pass filtering along with their PSD are depicted in Figure 3-17.

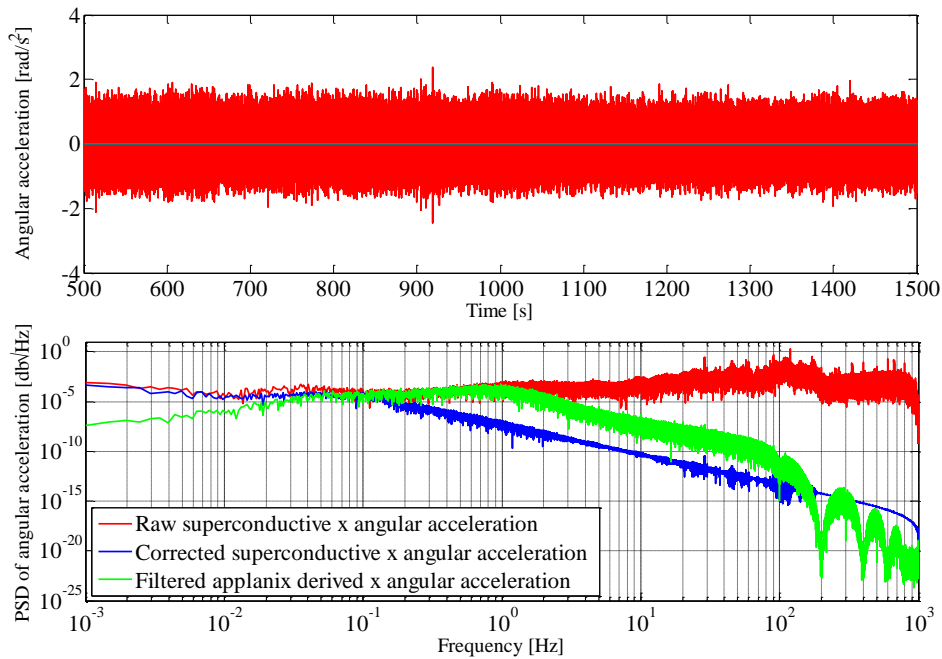


Figure 3-17: Raw (red line) and corrected (blue line) x angular acceleration in comparison to filtered Applanix derived x angular accelerations (green line) both in time domain (top plot) and frequency domain (bottom plot) (Provided by Gedex)

In the time domain it is hard to recognize the corrected superconductive x angular acceleration (blue line) from the filtered Applanix derived angular acceleration (green line). However, in the frequency domain, as can be seen from Figure 3-17, the low frequency error calculated by the multiple linear regression was not removed from the superconductive x angular acceleration in comparison to the filtered Applanix derived angular acceleration. The Butterworth low pass filtering reduces the high frequency errors in both the superconductive x angular acceleration and the Applanix derived x angular acceleration.

3.7 Summary

The information presented in this chapter included the Gedex system's working principles, measurements, measurements' noise, different reference frames, and its auxiliary sensors. The Gedex OQR gradiometer is accompanied by the superconductive angular and translational accelerometers and also some inertial sensors such as the Qflex accelerometers and the Applanix IMU. The purpose for using the superconductive angular and translational accelerometers is to model the dynamic vibration of the platform from the gradiometer output. However, both superconductive accelerations are noisy and this can limit the final performance of gradiometer output. The Gedex proposed empirical multiple linear regression and the Butterworth low pass filtering approaches removed the high frequency errors in the superconductive instruments. However, the low frequency errors did not reduce. The role of the angular acceleration derived from the Applanix IMU solution in this regression procedure was to estimate the bias error in the output of the superconductive angular accelerometer. It is needed to apply more effective methods to mitigate both low and high frequency errors of the superconductive instruments that may not require to engage the outputs of the auxiliary sensors.

Chapter 4: Error analysis of superconductive angular accelerometer and superconductive angular gradiometer data using static observations

In this chapter, the wavelet de-noising technique and Wiener low pass filtering will be implemented to remove high frequency errors in the output of the superconductive angular x-axis accelerometer. The wavelet de-trending technique will be applied to tackle the low frequency errors of this sensor, as well. The obtained results will then be compared with the empirical method to remove low and high frequency errors used by Gedex. This will then reveal the best filtering technique for the x angular acceleration. After that, these techniques will be used to filter the y angular acceleration and differential mode observation. Since there is no reference signal for validation of the filtered angular accelerations and gradients for the dynamic run of the system, all proposed filtering techniques will be applied to the static angular accelerations and differential mode measurements. The best filtering method will be selected based on its ability to reduce the RMS noise level. Finally, the best filtering technique will be applied on angular accelerations and differential mode output from the dynamic data set in Chapter 5.

In this chapter, before starting any data analysis, data available for this research is introduced and outliers will be removed from the available time series by the 3 standard deviation rule. Afterward, the best wavelet, decomposition level, and threshold estimators for the x angular acceleration data are chosen. Finally, the best wavelet methodologies will be applied on the y angular acceleration and the differential mode observation.

4.1 Data set available for this research

The data set used in this thesis includes the superconductive angular gradiometer output, and the superconductive angular and translational accelerations. Additionally, some auxiliary inertial sensors, such as the Applanix IMU and the Qflex translational accelerometer, are accompanying this superconductive instrument during the operation. The purpose for using all of these sensors is to help in compensating the errors in the output of gradiometer channel. Data sets for this research work came from two different runs of the system. The first one is from a static environment, where

the instrument was sitting undisturbed in the lab and the second one from a dynamic environment, where the instrument was under sinusoidal rotations in the lab. The first data set can be considered with known noise characteristics in this research work. Table 4-1 shows the detailed list of data available for this research for both dynamic and static data sets.

Table 4-1: List of data available for this research for both dynamic and static system operation

	Sensor	Observation	Unit
Superconductive Instruments	OQR z-axis gradiometer	Differential mode	rad/s^2
		Common mode (equivalently z angular accelerometer)	rad/s^2
	Superconductive angular accelerometer	x and y angular accelerations	rad/s^2
	Superconductive translational accelerometer	x, y, and z translational accelerations	m/s^2
Auxiliary Inertial Instruments	Applanix INS	Rotations along x, y, and z axes	rad
		Angular velocities along x, y, and z axes	rad/s
		Translational accelerations along x, y, and z axes	m/s^2
	Qflex accelerometer	Translational accelerations along x, y, and z axes	m/s^2

The only data sets used in this thesis is the output of the gradiometer and x and y angular accelerations which are shown in blue in Table 4-1. The reason for not using the inertial sensors is that the sensor outputs are less accurate than the superconductive instrument outputs. Additionally, the post processing method used in this thesis is wavelet spectral technique and low pass filtering which they don't require to add the inertial sensors outputs.

4.2 Removing outliers from observations using 3σ rule

Outliers are defined as data points that are noticeably different from the rest of the population. Outliers are caused by low quality instruments that produce poor measurements but they can occasionally be produced by high quality sensors (Sagar et al., 2009). It is very common to use the 3 standard deviation 3σ rule for this purpose.

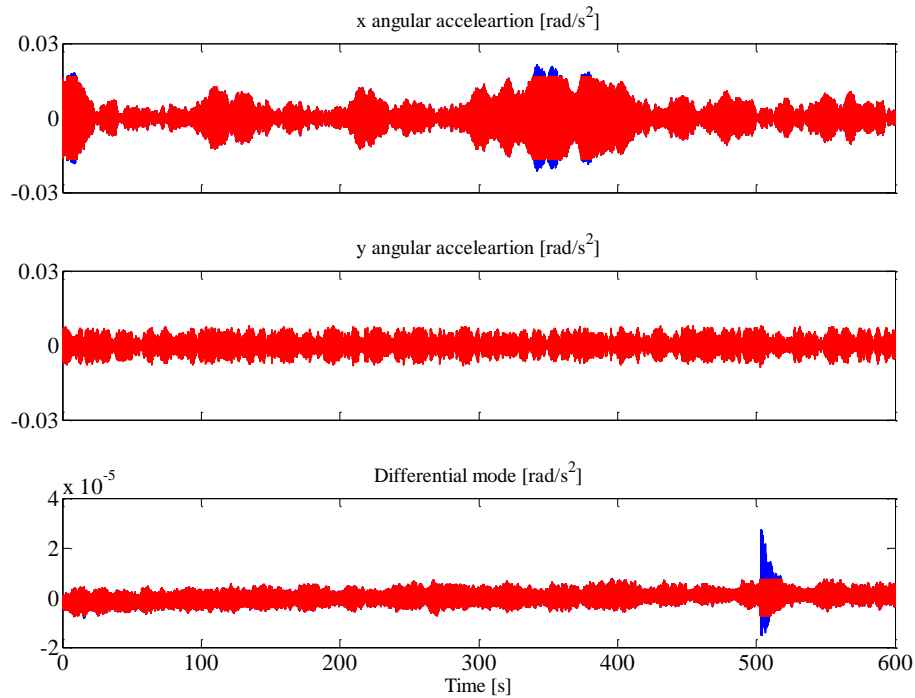


Figure 4-1: Differential mode (raw angular gradiometer output), x and y angular accelerations before removing the outliers (blue line) and after removing the outliers (red line) (all data from static run of the system)

Data points in a time series are considered as outliers if they are more than three standard deviations away from the mean (Ghilani and Wolf 2006). The differential mode (raw angular gradiometer output), and x and y angular accelerations before and after removing the outliers are depicted in Figure 4-1. As is clear from this figure, no outliers were detected for angular acceleration in the y channel. The number of outliers found in x angular acceleration is 1224 and for the gradiometer channel is 773 values. The outlier values replaced with the three standard deviations of the mean value in each time series.

4.3 Wavelet de-noising of x angular acceleration

Wavelet de-noising is proposed to cope with the high frequency errors in the angular accelerations. The basic wavelet de-noising technique includes signal decomposition, detail coefficients thresholding, and signal reconstruction with original approximation coefficients and modified

detail coefficients at predetermined Level of Decomposition (LOD). Appendix A provides the main equations used in wavelet analysis. There is a set of parameters that needs to be selected for the wavelet de-noising of angular accelerations. These parameters are:

- Wavelet base function
- Optimization criteria
- Threshold type and threshold estimator
- Level of decomposition

In order to discover the wavelet efficiency in applying to the x angular acceleration, possible combinations of these parameter will be investigated in the next section. These parameters will be discussed briefly in this section. After deciding about the best approach for de-noising, the methodology can be generalized to the y angular acceleration and the gradient data from the static run of the system.

4.3.1 Wavelet base function

The first parameter to be selected in any de-noising procedure is selecting the wavelet base function. In this thesis, wavelet families including Daubechy, Symlet, Coiflet, and Biorthogonal have been tested for de-noising. It has been found that the choice of wavelet family plays only a secondary role in de-noising of the available data sets for this work, while it is the number of vanishing moments in each family that primarily effects the result. 37 wavelets were applied to the data and are listed in Table 4-2.

Table 4-2: Various wavelets used in this chapter

Wavelet Name	Number of vanishing moments
Daubechy (Db)	1, 2, 3, 4, 5, 6, 7, 8, 9
Symlet (Sym)	2, 3, 4, 5, 6, 7, 8, 9
Coiflet (Coif)	2, 3, 4, 5
Biorthogonal (Bior)	1.1, 1.3, 1.5, 2.2, 2.4, 2.6, 2.8, 3.1, 3.3, 3.5, 3.7, 3.9, 4.4, 5.5, 6.8

4.3.2 Optimization criterion

The optimization criterion for selecting the best wavelet is the Root Mean Squared (RMS) difference between the true signal (which is zero here) and its reconstructed version. As explained before, the data set came from the static run of the system, which can be considered with known noise characteristics in this research work. Thus, this known noise characteristic will be minimized as much as possible. The performance of the de-noised signal is evaluated through the RMS difference function e defined as (Lyrio et al., 2004):

$$e = \sqrt{\frac{1}{N} \sum_{i=1}^N (t_i - \hat{t}_i)^2} \quad (4-1)$$

where t is the true signal and \hat{t} is the de-noised signal. The true signal in this case is considered to be a zero vector. The smallest RMS difference achieved by any wavelet with a specific vanishing moment can identify the best wavelet or the best de-noising method for this data set.

4.3.3 Thresholding procedure

Another important parameter for de-noising is the optimum thresholding scheme. The best thresholding will use the optimization criterion explained in the previous section. The procedure will consider parameters such as the type of threshold estimator, soft or hard thresholding, noise estimation procedure, and rescaling the threshold. In this thesis, four different thresholds known as Median, SURE, Heuristic, and Minimax were selected to compute the threshold magnitude. Soft thresholding is used for applying the threshold on the signal. The noise level was estimated using Equation (A-14). Threshold rescaling is done to deal with the type of noise found in the angular acceleration signal. Generally, threshold rescaling uses three assumptions: the unit noise assumption, which can lead to no rescaling of the threshold, the white noise assumption, which can lead to rescaling the threshold based on the noise level computed from the first level of decomposition (global thresholding), and the non-white noise assumption, which can lead to rescaling the threshold magnitude based on the noise level computed for each level of decomposition (level-dependent threshold). Threshold magnitudes computed by four different

threshold estimators considering the unit noise and white noise assumptions are listed in Table 4-3. It is obvious from this table that the original threshold magnitudes are very large for almost all the threshold estimators in comparison to the rescaled threshold magnitudes by the white noise assumption.

Table 4-3: Threshold magnitudes computed by four different threshold estimators considering the unit noise and white noise assumptions

Threshold type	No scaling threshold	Global threshold
Median	4.83	2.56e-04
SURE	0.023	1.47e-05
Heuristic	4.127	1.48e-05
Minimax	3.43	1.84e-04

On the other hand, Table 4-4 shows how threshold magnitude is rescaled for each LOD by the non-white noise assumption. Results in these tables are computed for the x angular acceleration using the Coif5 wavelet.

Table 4-4: Threshold magnitudes computed by four different threshold estimators with the non-white noise assumption

Threshold type \ LOD	Median	SURE	Heuristic	Minimax
1	0.0003	0.0001	0.0001	0.0002
2	0.0016	0.0007	0.0015	0.0012
3	0.0030	0.0007	0.0007	0.0021
4	0.0806	0.0193	0.0193	0.0580
5	0.0291	0.0070	0.0070	0.0209
6	0.0062	0.0038	0.0050	0.0044
7	0.0048	0.0021	0.0036	0.0034
8	0.0023	0.0006	0.0006	0.0017

By looking at the rescaled thresholds with the non-white noise assumption in Table 4-4, it is clear that the threshold magnitudes are increasing up to the 4th LOD and then they are decreasing from the 4th to the 8th LOD. This effectively shows the behavior of the noise contaminated in the x angular accelerations at different decomposition levels. If the rescaled threshold magnitude with the white noise assumption is used, the behavior of the noise in the first decomposition level will

be generalized to other decomposition levels. This might not be a valid assumption for analysing the angular accelerometer data.

It will be discussed in detail in Section 5.2 that the noise behavior of the superconductive instrument by design follows the red noise structure where the PSD of the noise has the form of $\frac{1}{f^2}$ (where f is the frequency). Therefore the threshold rescaling of the coefficients can be done by taking this piece of information into account. For this purpose, the noise level is calculated from the first LOD with the robust median absolute deviation, Equation (A-14), then rescaling it by the $\frac{1}{f^2}$ rule for the other LODs. Figure 4-2 and Figure 4-3 show the noise level based on the robust median absolute deviation and the rescaled noise level by the $\frac{1}{f^2}$ rule for the static x and y angular accelerations and also for the static differential mode observation, respectively.

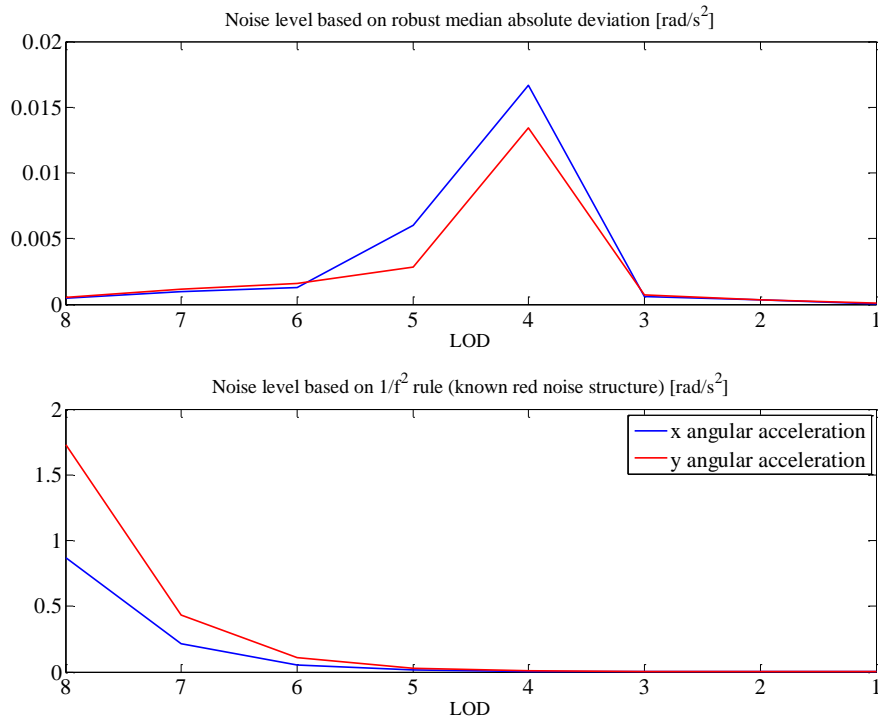


Figure 4-2: Noise level calculated for x and y angular acceleration based on the robust median absolute deviation and rescaled noise level from the first LOD by the $\frac{1}{f^2}$ rule

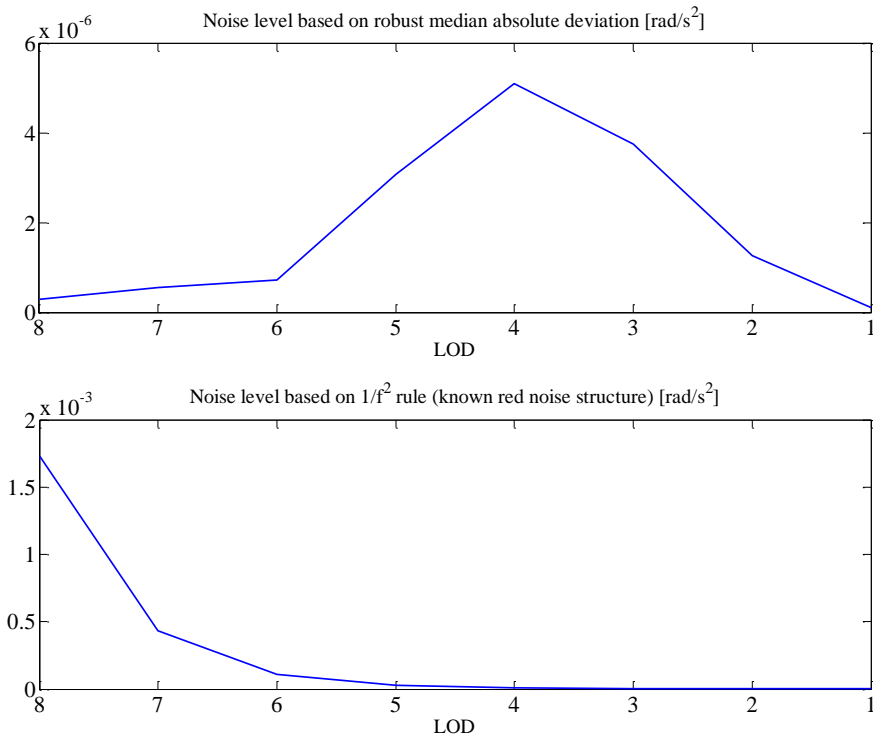


Figure 4-3: Noise level calculated for differential mode observation based on the robust median absolute deviation and rescaled noise level from the first LOD by the $\frac{1}{f^2}$ rule

Based on the knowledge from the wavelet analysis, the finer decomposition levels (smaller LOD) are representative of the noise contributions in any signal. Therefore, it is expected to have larger noise levels at finer scales. However, as it is clear from the top plots in both Figures 4-2 and 4-3, the noise levels from 1st to 3rd decomposition levels are small in magnitude. The larger noise level for both the accelerometer and the gradiometer observations occurs at the 4th LOD. Now, we can take the noise levels from the 1st to 4th LOD and rescale it as per the red noise behavior where there should be a larger noise level at smaller frequencies rather than larger frequencies (like what is illustrated in the bottom plots in both Figures 4-2 and 4-3). It can be shown that for the kind of observations we have for this research, it is more practical to estimate the noise level at each LOD regardless of the kind of non-white noise we have in the data. The de-noised signal as a result of this process will produce the same result as if we use the third option in de-noising where the reconstruction is done by only approximation coefficients, where the detail coefficients after

thresholding by the red noise assumption are shrunk to zero. More details regarding the results of the three de-noising approaches will be given in Sections 4.3.5 to 4.3.7.

4.3.4 Level of decomposition

To be consistent with the 1 Hz cut-off frequency that Gedex used to filter the angular accelerometer output, the multiresolution decomposition level has been selected at 7, which corresponds to signals with 1 Hz frequencies (see Appendix A, i.e., Equation (A-5) and Table (A-2) for this selection). The standard de-noising procedures in commercial packages (e.g., MATLAB) is done by the signal reconstruction with original approximation and all modified detail coefficients from the 1st to the 7th LOD. However, in this study, the reconstruction is done with the original approximation and modified detail coefficients at the 7th LOD. Moreover, the reconstruction is done with only original approximation at the 7th LOD.

The idea of using these different LOD was confirmed, especially when the energy of the signal is calculated and plotted. The log energy of the x angular acceleration is depicted in Figure 4-4. The expectation for the behavior of the noise is to have larger magnitude for the lower LOD. After applying the threshold, it is expected to decrease the energy of the noise from the larger to the smaller LOD. However, as can be seen from the energy of the original coefficient (red line), the expected behavior of the noise only occurs from the 4th level to 12th. After applying the level-dependent thresholding on the coefficients, the energy of the wavelet coefficient follows the expected behaviour up to the 6th LOD and then starts increasing after that. The energy of the rescaled coefficient with the white noise assumption (global thresholding scheme) shows a behaviour similar to the original coefficients. So, based on this analysis, it can be concluded that modifying the detail coefficients with the white noise assumption and taking the detail coefficients from all LODs into the de-noising procedure might not produce the optimum de-noising result. Reconstructing the signal with only modified detail coefficients at the 7th LOD with the non-white noise assumption can be an option for improvements.

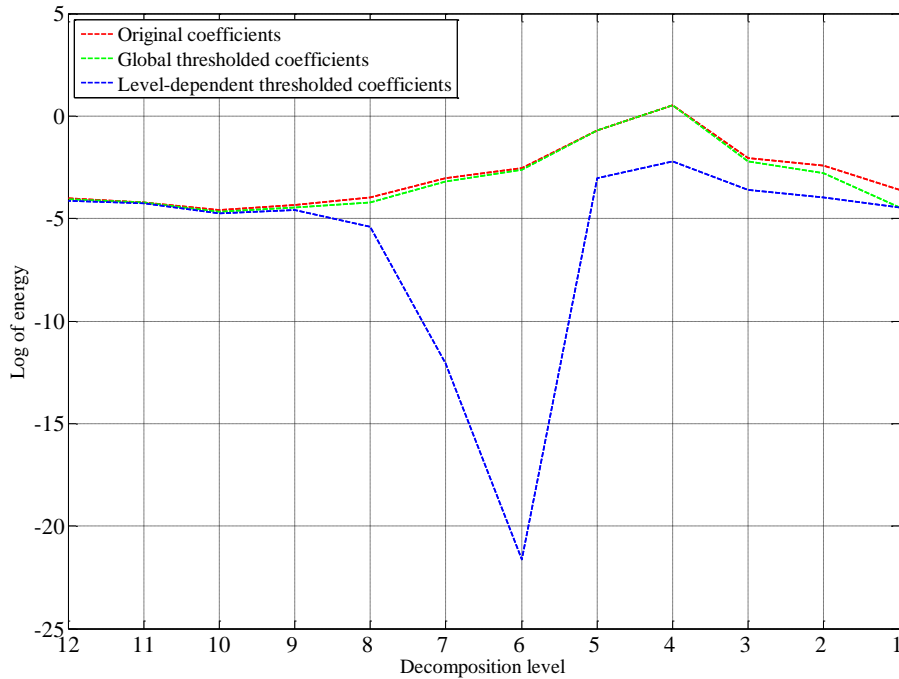


Figure 4-4: Variation of energy for original and shrunk coefficients (Coif5 with Minimax threshold estimator)

Therefore, three approaches are proposed for the de-noising of the x angular acceleration data as:

- 1- First approach: reconstructing the signal with the original approximation coefficients at the 7th LOD and modified detail coefficients from the 1st to the 7th LOD
- 2- Second approach: reconstructing the signal with the original approximation and the modified detail coefficients at the 7th LOD
- 3- Third approach: reconstructing the signal with only original approximation coefficients at the 7th LOD

All these proposed methods will be examined on the x angular acceleration data to discover which of them is able to produce the minimum RMS results. Detailed analysis about these different approaches is given in the next sub-section.

4.3.5 Results of de-noising: first approach

As explained in Section 4.3.1, four wavelet families with different vanishing moments have been used to decompose the x angular acceleration into detail and approximation coefficients. In this section, reconstruction is done with original approximation coefficients and modified detail coefficients from the 1st to the 7th LOD. Rescaling the detail coefficients is done by applying the global and level-dependent thresholding schemes. Table 4-5 shows the best wavelet families that generated the minimum RMS result by rescaling the detail coefficients with the white noise assumption. The results are also recorded for four different threshold estimators.

Table 4-5: Selected wavelet families that generated the minimum RMS result by rescaling the detail coefficients with global thresholding scheme (de-noising first approach)

Threshold type	Wavelet	RMS (rad/s^2)
Median	Db1	4.22e-03
SURE	Db1	5.38e-03
Heuristic	Db1	5.38e-03
Minimax	Db1	4.50e-03

Threshold type	Wavelet	RMS (rad/s^2)
Median	Sym2	5.14e-03
SURE	Sym2	5.44e-03
Heuristic	Sym2	5.44e-03
Minimax	Sym2	5.22e-03

Threshold type	Wavelet	RMS (rad/s^2)
Median	Coif2	5.34e-03
SURE	Coif3	5.45e-03
Heuristic	Coif3	5.45e-03
Minimax	Coif2	5.37e-03

Threshold type	Wavelet	RMS (rad/s^2)
Median	Bior1.1	4.22e-03
SURE	Bior1.1	5.38e-03
Heuristic	Bior1.1	5.38e-03
Minimax	Bior1.1	4.50e-03

Based on this table, the minimum RMS value is achieved for both Bior1.1 and Db1 with the Median threshold estimator showed in blue in this table. The RMS value of the original signal is $0.0055 rad/s^2$. Therefore, the best result in this approach shows a 23% improvement in reducing the noise level. The worst results belong to the Coif3 and the Sym2 wavelet families both for the SURE and the Heuristic threshold estimators. Figure 4-5 shows the original and de-noised signals along with coefficients before and after thresholding for the best result with the Bior1.1 wavelet.

As stated before, there was some expectations to see worse results after applying the global threshold on the coefficients.

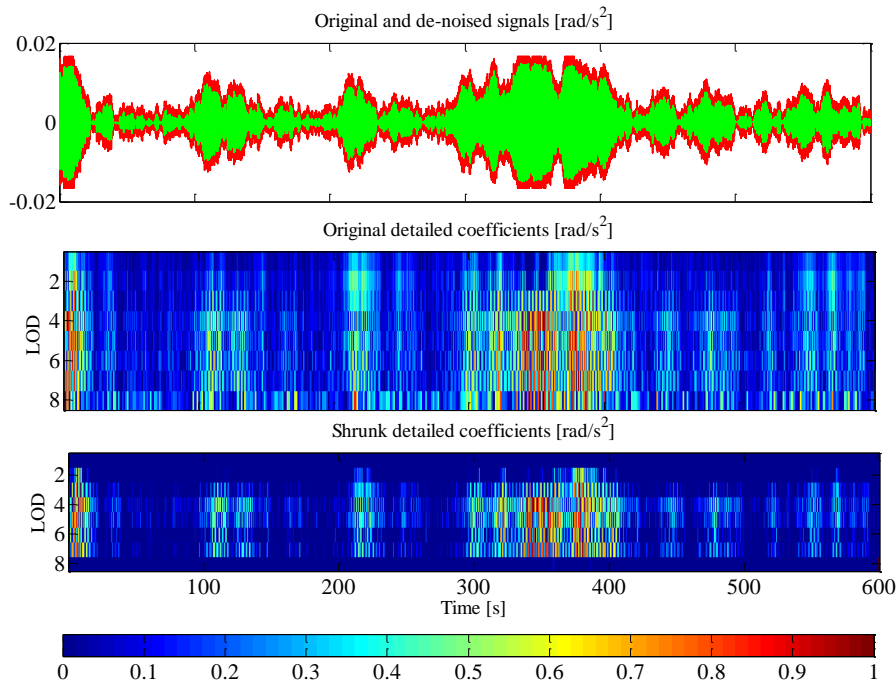


Figure 4-5: Original (red line) and de-noised (green line) signals along with their original and shrunk coefficients. Computed with the Bior1.1 wavelet and global thresholding scheme (de-noising first approach)

To make it more tangible, the reconstructed signal by the detail coefficients at different LOD before and after applying the global threshold is depicted in Figure 4-6. As can be seen from both Figure 4-5 and Figure 4-6, there is a slight difference between the original and the shrunk coefficients from the 2nd to the 7th LOD. As a result, there is not that much difference between the original and the de-noised signal in the first approach. Using the first approach for de-noising, the level-dependent threshold can be applied to the detail coefficients. Table 4-6 shows the selected wavelet families with the minimum RMS difference between the zero vector and the de-noised signal when the non-white noise is assumed in the data. Based on this table, the minimum RMS value is calculated for the Coif4 with the Median threshold estimator, which is shown in blue in this table. The Median threshold estimator showed its capability for providing the minimum RMS

values for all types of wavelet. The best result in this approach shows a 98.77% improvement in reducing the noise level in comparison to the original signal.

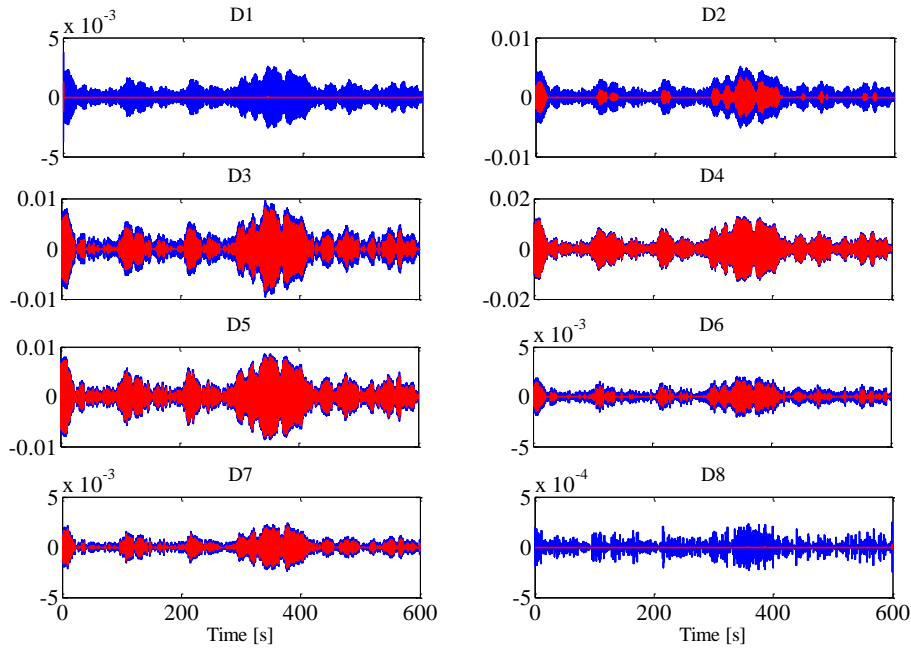


Figure 4-6: Reconstructed signal rad/s^2 with original detail coefficients (blue line) and modified details (red line) using Bior1.1 wavelet from the 1st to the 8th LOD. Coefficients have been shrunk with the Median threshold and the white noise assumption

Table 4-6: Selected wavelet families that generated the minimum RMS results by rescaling the detail coefficients with level-dependent thresholding scheme (de-noising first approach)

Threshold type	Wavelet	RMS (rad/s^2)
Median	Db8	6.78e-05
SURE	Db5	2.56e-03
Heuristic	Db1	2.27e-03
Minimax	Db4	2.40e-04

Threshold type	Wavelet	RMS (rad/s^2)
Median	Sym4	7.09e-05
SURE	Sym9	2.50e-03
Heuristic	Sym4	2.40e-03
Minimax	Sym4	2.42e-04

Threshold type	Wavelet	RMS (rad/s^2)
Median	Coif4	6.72e-05
SURE	Coif2	2.59e-03
Heuristic	Coif2	2.38e-03
Minimax	Coif3	2.34e-04

Threshold type	Wavelet	RMS (rad/s^2)
Median	Bior1.3	7.45e-05
SURE	Bior4.4	2.49e-03
Heuristic	Bior1.1	2.27e-03
Minimax	Bior2.8	2.27e-04

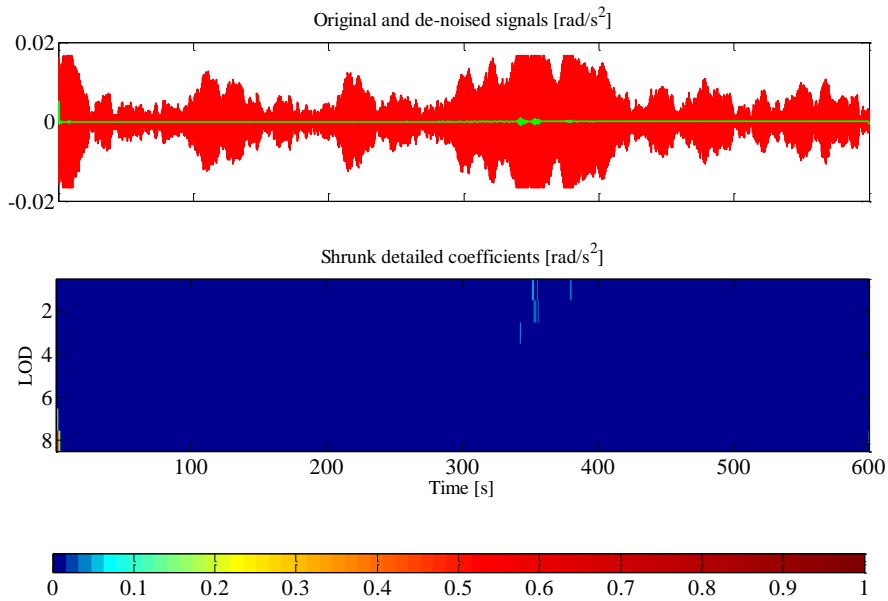


Figure 4-7: Original (red line) and de-noised (green line) signals with shrunk coefficients. Computed with the Coif3 wavelet and the level-dependent thresholding scheme (de-noising first approach)

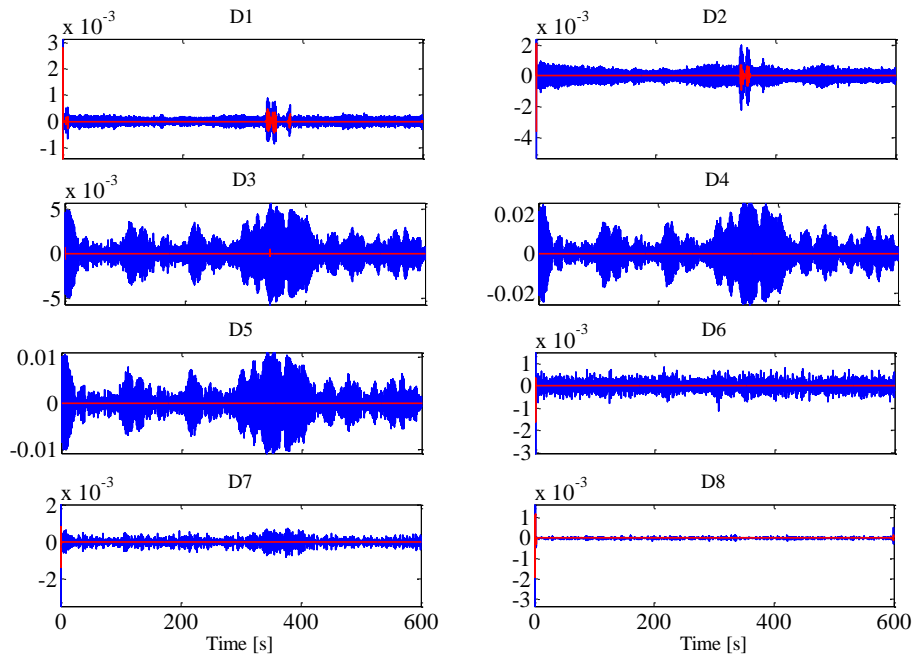


Figure 4-8: Reconstructed signal rad/s^2 with original detail coefficients (blue line) and modified details (red line) using the Coif3 wavelet from the 1st to the 8th LOD. Coefficients have been shrunk with the Median threshold estimator and the non-white noise assumption

Figure 4-7 shows the original and de-noised signals along with its shrunk coefficients for the best wavelet. To make it more tangible, the reconstructed signal by detail coefficients at different LOD before and after applying the level-dependent threshold can be seen in Figure 4-8. As is clear from this figure, almost all the coefficients were affected (reduced the amplitude) by the kind of threshold that was applied to the original coefficients.

4.3.6 Results of de-noising: second approach

It seems that by including the detail coefficients from the 1st to the 7th LOD in the reconstruction step, more noise is added to the de-noising procedure. So, in this section, the signal will be reconstructed with only original approximation and modified detail coefficients at the 7th LOD. The results of this analysis after applying the global and level-dependent thresholding schemes are given in Table 4-7 and Table 4-8, respectively.

Table 4-7: Selected wavelet families that generated the minimum RMS results with global threshold rescaling (de-noising second approach)

Threshold type	Wavelet	RMS (rad/s^2)
Median	Db8	9.25e-05
SURE	Db8	1.07e-04
Heuristic	Db8	1.07e-04
Minimax	Db8	9.65e-05

Threshold type	Wavelet	RMS (rad/s^2)
Median	Sym7	1.03e-04
SURE	Sym7	1.18e-04
Heuristic	Sym7	1.18e-04
Minimax	Sym7	1.07e-04

Threshold type	Wavelet	RMS (rad/s^2)
Median	Coif5	8.89e-05
SURE	Coif5	1.02e-04
Heuristic	Coif5	1.02e-04
Minimax	Coif5	9.25e-05

Threshold type	Wavelet	RMS (rad/s^2)
Median	Bior1.5	9.34e-05
SURE	Bior1.5	1.24e-04
Heuristic	Bior1.5	1.24e-04
Minimax	Bior1.5	9.43e-05

As is clear from these tables, when we only work with the 7th LOD, the assumption of the white and non-white noises for rescaling the thresholds does not influence the final result. In both thresholding schemes, the best result is obtained using the Coiflet families. However, the worst result in Table 4-7 is obtained using the Symlets wavelet families and the worst result in Table 4-8 is obtained using the Biorthogonal wavelet families. Although the results with white and non-

white noise assumptions are very close to each other, the minimum RMS value is recorded when the rescaling was done with the level-dependent thresholding scheme. The best wavelet is the Coif5 with almost all the threshold types shown in blue in Table 4-8.

Table 4-8: Selected wavelet families that generated the minimum RMS results with level-dependent threshold rescaling (de-noising second approach)

Threshold type	Wavelet	RMS (rad/s^2)	Threshold type	Wavelet	RMS (rad/s^2)
Median	Db8	6.20e-05	Median	Sym4	7.77e-05
SURE	Db8	6.20e-05	SURE	Sym7	7.80e-05
Heuristic	Db8	6.19e-05	Heuristic	Sym4	7.73e-05
Minimax	Db8	6.19e-05	Minimax	Sym4	7.73e-05

Threshold type	Wavelet	RMS (rad/s^2)	Threshold type	Wavelet	RMS (rad/s^2)
Median	Coif5	5.38e-05	Median	Bior1.3	7.39e-05
SURE	Coif5	5.45e-05	SURE	Bior6.8	8.34e-05
Heuristic	Coif5	5.38e-05	Heuristic	Bior1.3	7.39e-05
Minimax	Coif5	5.38e-05	Minimax	Bior1.3	7.40e-05

The original signal and de-noised signal after applying the level-dependent threshold are depicted in Figure 4-9. The minimum RMS value in this approach has $5.38e-05$ in rad/s^2 while the minimum RMS value in the previous approach was $6.72e-05$ in rad/s^2 . The second approach for de-noising showed 20% reduction in RMS value in comparison to the best result in the first approach. The best result here shows 99.01% improvement in reducing the noise level in comparison to the original signal.

Figure 4-10 shows the reconstructed signal with the approximation coefficient and modified detail coefficient at the 7th LOD. Once again, more reduction is obvious in the amplitude of the modified details (red line) by the non-white noise assumption in plot (B). Red line in plot (B) plus the blue line in plot (A) is what we summed to create the best result in Figure 4-9 (top figure with green line).

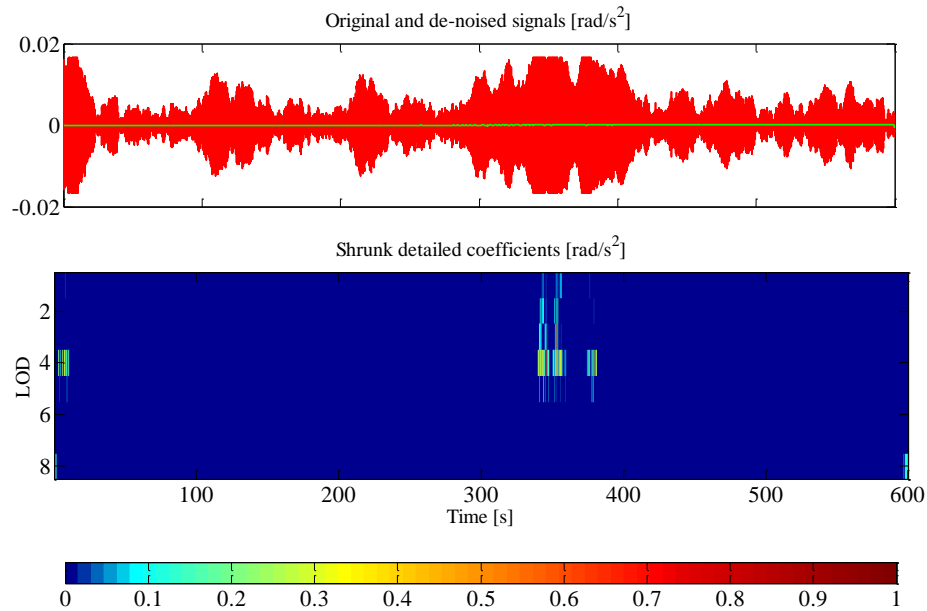


Figure 4-9: Original (red line) and de-noised (green line) signals with shrunk coefficients. Computed with Coif5 and level-dependent thresholding scheme (de-noising second approach)

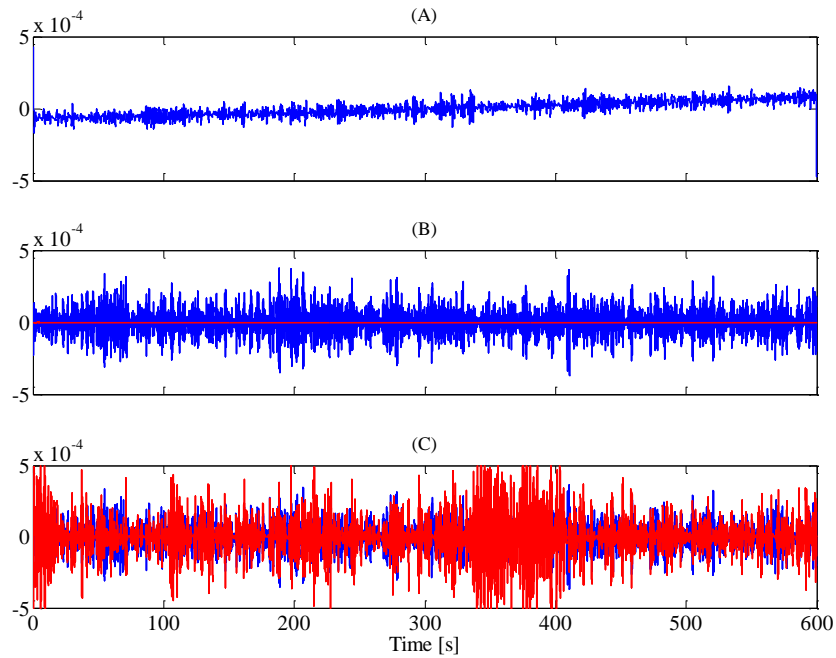


Figure 4-10: (A) Reconstructed signal with the original approximation coefficient at the 7th LOD. (B) Reconstructed signal (non-white noise assumption) with the original detail coefficient (blue line) and modified detail coefficient with the Minimax threshold (red line) at 7th LOD. (C) Reconstructed signal (white noise assumption) with original detail coefficient (blue line) and modified detail coefficient with the Median threshold (red line) at 7th LOD. The Coif5 wavelet was used in all reconstruction

4.3.7 Results of de-noising: third approach

The last option for de-noising is reconstructing the signal with only the approximation coefficient at the 7th LOD. The minimum RMS values are listed in Table 4-9. The best result here is obtained by using the Coif5 wavelet and the worst result by using the Sym7 wavelet. The best result achieved with the second approach showed a 1% improvement in comparison to the best result achieved in the third approach.

Table 4-9: Selected wavelet families that generate the minimum RMS results reconstructed with only approximation coefficients at the 7th LOD

Wavelet	RMS (rad/s^2)
Db9	6.44e-05
Sym7	8.92e-05
Coif5	5.38e-05
Bior1.3	7.39e-05

The results up to here indicate that the best approach for removing the noise from the x angular acceleration is obtained by the second approach when the reconstruction is done with the original approximation and modified detail coefficients at the 7th LOD by the non-white noise assumption. The best wavelet is the Coif5 and the best performance has been recorded for the Median, Heuristic, Minimax threshold estimator.

4.4 Butterworth and Wiener low pass filtering results

The estimation of the PSDs for both the true signal and the measurement noise are needed for computing the Wiener filter's frequency response. In this research work, the estimate of the true signal is the de-noised signal (reconstructed signal with the original approximation and modified detail coefficients at the 7th LOD with the Coif5 wavelet). The noise estimate is calculated by subtracting the de-noised signal from raw data. After computing the filter's frequency response, which is depicted in Figure 4-11, Equation (A-18) can be used to get the filtered x angular

acceleration. The Butterworth low pass filtering with 1 Hz cut-off frequency, as explained in Section 3-6, is another frequency domain filter, which can be applied to the angular acceleration.

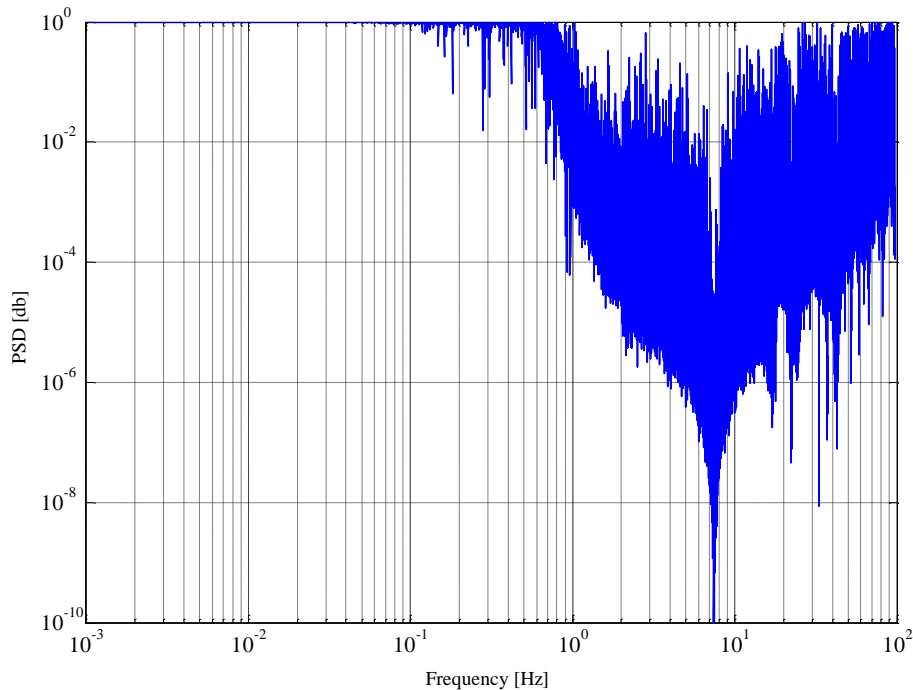


Figure 4-11: Wiener filter's frequency response (calculated for x angular acceleration)

Figure 4-12 shows the PSD of the de-noised x angular acceleration in comparison to the two frequency domain filters: Wiener and Butterworth low pass filtering. The RMS value of the filtered signal after applying the Wiener filtering is $5.02e-05 \text{ rad/s}^2$ that in comparison to the RMS value of the wavelet de-noised signal of $5.38e-05 \text{ rad/s}^2$ provides 7% improvement in reducing the noise level. The RMS value of the Butterworth result is $9.60e-05 \text{ rad/s}^2$. The RMS value achieved by wavelet de-noising showed 44% improvement in comparison to the Butterworth low pass filtering result. The RMS value of the result after the Butterworth low pass filtering and the wavelet de-noising showed 98.24% and 99.02% improvement in reducing the noise level in comparison to the original signal, respectively.

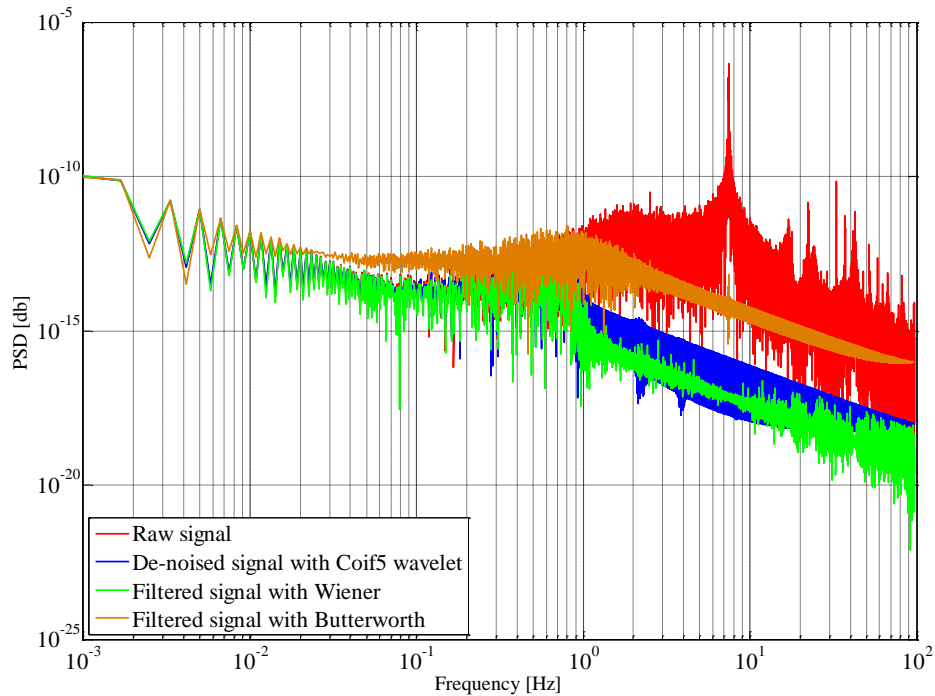


Figure 4-12: Comparison between the de-noised x angular acceleration with the frequency domain filters: Butterworth and Wiener

It is worth mentioning that the result of the Wiener low pass filtering depends on how the estimated true signal is selected. For instance, if the estimated true signal is the output of the Butterworth low pass filtering, the RMS value achieved from the filtered x angular acceleration is $6.95e-05 \text{ rad/s}^2$ that, in comparison to the RMS value of the de-noised signal provides a worse result. However, the result of the Wiener low pass filtering in comparison to the Butterworth low pass filtering itself showed 28% improvement in reducing the noise level.

4.5 Wavelet de-trending and de-noising of x angular acceleration

De-trending and de-noising is a three-step process. In the first step, wavelet decomposition of the signal is made up to the 8th, 9th, and 10th LODs. Then signal reconstruction is done by approximation coefficients for wavelets with various vanishing moments. This process creates different trends for each LOD. To select among these trends, the RMS difference between each trend and the zero vector (an assumption of no trend) is calculated. The smallest RMS achieved

by any wavelet will be considered as the best wavelet for producing the desired trend. Table 4-10 shows the wavelet families, which produced the best trends for the x angular acceleration.

Table 4-10: Wavelet candidates that produce the best trends for the x angular acceleration

LOD	8	9	10
Wavelet	Db9	Db9	Db1
	Sym7	Sym7	Sym7
	Bior1.3	Bior1.3	Bior1.1
	Coif5	Coif5	Coif5

The second step of the de-trending and de-noising is to remove the desired trend from the raw data. For example, consider the 8th LOD in which the approximation coefficient with Db9 has been detected as the best trend. The trend is removed from the raw data and the residual is generated. Finally, the residual is processed by the wavelet de-noising procedure where the signal reconstruction is done by original approximation and modified detail coefficients at the 7th LOD by rescaling the thresholds with the level-dependent noise thresholding. Results of the de-trending and de-noising are shown in Table 4-11 for different wavelet families and threshold estimators.

Table 4-11: Selected wavelet families that generate the minimum RMS results for the x angular acceleration (Results for the de-trending approach at the 8th LOD)

Threshold type	Wavelet	RMS (rad/s ²)	Threshold type	Wavelet	RMS (rad/s ²)
Median	Db8	4.45e-05	Median	Sym3	5.54e-05
SURE	Db8	4.68e-05	SURE	Sym6	6.78e-05
Heuristic	Db8	4.55e-05	Heuristic	Sym3	5.96e-05
Minimax	Db8	4.57e-05	Minimax	Sym3	6.03e-05

Threshold type	Wavelet	RMS (rad/s ²)	Threshold type	Wavelet	RMS (rad/s ²)
Median	Coif5	3.08e-05	Median	Bior1.3	3.55e-05
SURE	Coif5	3.18e-05	SURE	Bior1.5	5.38e-05
Heuristic	Coif5	3.08e-05	Heuristic	Bior1.3	3.55e-05
Minimax	Coif5	3.08e-05	Minimax	Bior1.3	3.57e-05

As can be seen from this table, the best families (giving the lowest RMS values) are the Coiflet and Biorthogonal families with the Minimax and Median threshold estimators, respectively

(shown in blue in this table). The PSD of the reconstructed signal with the Coif5 wavelet is plotted in Figure 4-13. One can compare this result with the PSDs of the de-noised and raw signals, as well. As can be seen from this figure, the low frequency error is successfully removed from the data. The de-trended and de-noised signal shows a 99.44% improvement in reducing the noise level in comparison to the original signal.

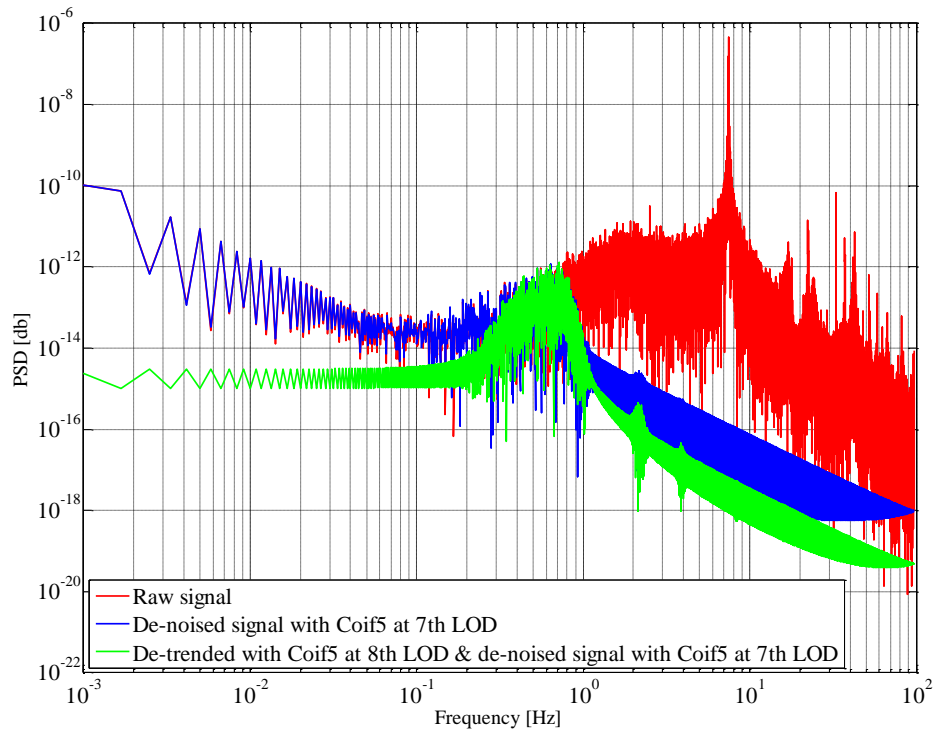


Figure 4-13: De-trended and de-noised x angular acceleration in comparison to the de-noised and raw signals

With the hope of improvement, the LOD is increased to the 9th and 10th LODs. The same procedure was repeated and the result is shown in Table 4-12. As can be seen from this table, when the LOD is increased, larger RMS values are produced. Therefore, the best wavelet de-trending and de-noising approach is the 8th LOD.

Table 4-12: Selected wavelet families that generate the minimum RMS results for the x angular acceleration (Results for de-trending approach at the 9th and the 10th LODs)

Threshold type	RMS (rad/s^2) (at 9 th LOD)	RMS (rad/s^2) (at 10 th LOD)	Threshold type	RMS (rad/s^2) (at 9 th LOD)	RMS (rad/s^2) (at 10 th LOD)
Median	6.00e-05	4.80e-05	Median	1.05e-04	1.66e-04
SURE	6.31e-05	4.79e-05	SURE	1.13e-04	1.72e-04
Heuristic	6.16e-05	4.78e-05	Heuristic	1.08e-04	1.67e-04
Minimax	6.19e-05	4.78e-05	Minimax	1.08e-04	1.68e-04

Threshold type	RMS (rad/s^2) (at 9 th LOD)	RMS (rad/s^2) (at 10 th LOD)	Threshold type	RMS (rad/s^2) (at 9 th LOD)	RMS (rad/s^2) (at 10 th LOD)
Median	3.48e-05	3.63e-05	Median	3.79e-05	6.16e-05
SURE	3.58e-05	3.73e-05	SURE	5.45e-05	7.40e-05
Heuristic	3.48e-05	3.63e-05	Heuristic	3.80e-05	6.16e-05
Minimax	3.48e-05	3.63e-05	Minimax	3.82e-05	6.17e-05

It is worth mentioning that it is possible to design a bandpass filter instead of the wavelet de-trending and de-noising that can be properly model both the low frequency trends and the high frequency errors in the x angular acceleration. The explanation regarding such a bandpass filter is given in Appendix B. The results in the appendix indicates that designing an optimum bandpass digital filter is not an easy task; however, its implementation is much simpler than wavelet de-trending and de-noising analysis.

4.6 Wavelet de-trending and de-noising of x angular acceleration in comparison to empirical linear regression approach

Gedex used a linear regression approach for modeling the low frequency error in the angular accelerometer output (see Chapter 3). The general concept behind this regression procedure is that the contaminated low frequency error in the output of the superconductive angular acceleration is a function of translational accelerations in x, y, and z directions combined with temperature fluctuations. Since temperature information is not available for this work, only translational accelerations and the Applanix derived angular acceleration will be used in the linear regression (see also Section 3.6). Figure 4-14 shows the low frequency error computed by the linear

regression and by the wavelet de-trending (approximation coefficient at the 8th LOD with the Coif5 wavelet).

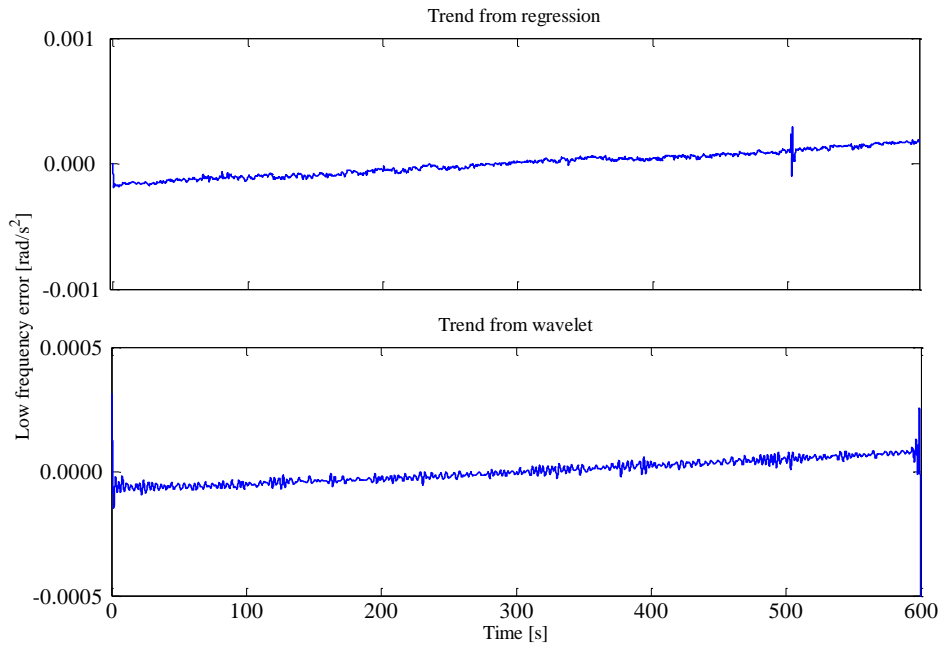


Figure 4-14: Trend computed as a result of linear regression in comparison to the trend computed by wavelet (approximation at 8th LOD with Coif5)

There are three approaches for removing the high frequency errors from the data after removing the low frequency error from the raw data either by the regression or the wavelet de-trending technique. The first approach is wavelet de-noising, the second approach is the Butterworth low pass filtering, and the third one is the Wiener low pass filtering. For the case of Wiener filtering, the estimation of the true signal is the de-trended and de-noised signal from the wavelet analysis. The wavelet de-trending and de-noising result can be compared with the result of the linear regression, Butterworth and Wiener low pass filtering in Figure 4-15.

Both Wiener and wavelet results show some improvement in reducing the noise level versus the Butterworth low pass filtering result. The RMS value for the result after applying the regression and Butterworth filtering is $9.08e-05 \text{ rad/s}^2$. However, the RMS value after applying the wavelet

de-noising and de-trending on the signal is $3.08e-05 \text{ rad/s}^2$. The wavelet de-noising and de-trending performance shows a 66% improvement in comparison to the performance of the linear regression and the Butterworth low pass filtering procedure. Empirical approach shows 98.33% improvement in reducing both the low and high frequency errors in comparison to the original signal. However, the improvement by wavelet de-trending and de-noising is 99.44%.

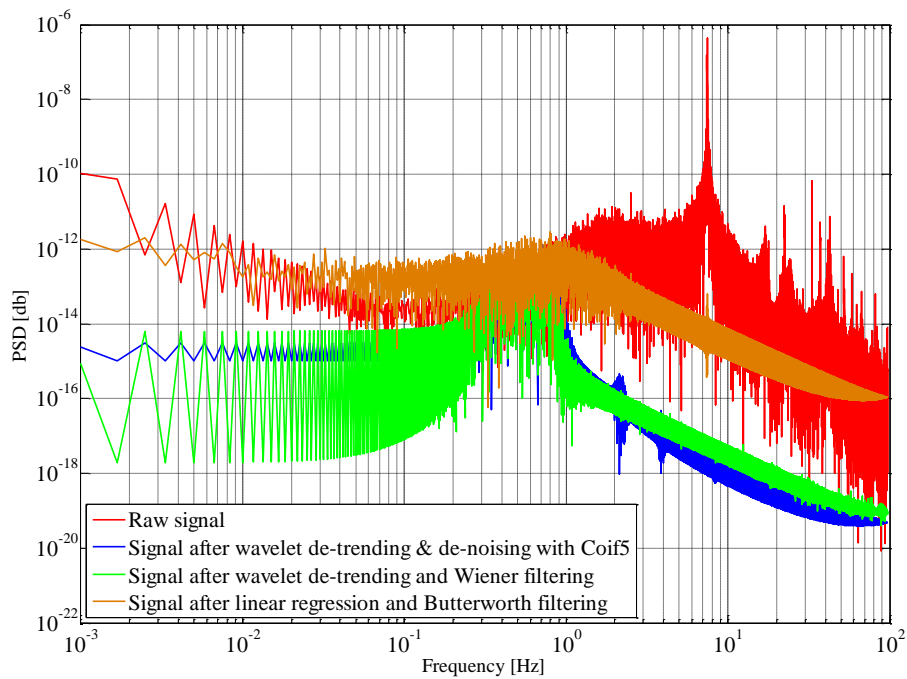


Figure 4-15: The x angular acceleration after applying the linear regression and Butterworth low pass filtering (blue line) in comparison to the signal after wavelet de-trending and de-noising with Bior1.3 wavelet (green line)

The RMS value of the signal after applying the wavelet de-trending and then the Wiener low pass filtering is $2.59e-05 \text{ rad/s}^2$. It shows 16% improvement in reducing the noise level in comparison to the results using the wavelet de-trending and de-noising approach. It is noteworthy that the Wiener low pass filtering result is influenced by how the estimated true signal is selected. The true signal used as the input to the filter in this section is the result of wavelet de-trending and de-noising approach and therefore it is not surprising that it provides the lowest RMS value in this process.

4.7 Wavelet de-trending and de-noising of y angular acceleration

As was discussed in Section 4.5, the best wavelet de-trending and de-noising approach is a three-step process. In the first step, wavelet decomposition of the y angular acceleration is made up to the 8th LOD. The signal reconstruction is then done by approximation coefficients for each wavelet with various vanishing moments. This process produces the different trends. The RMS difference between each trend and the zero vector is calculated. The smallest RMS value achieved by any wavelet identify the best wavelet for producing the desired trend. Table 4-13 shows the best wavelets for producing the wanted trend for different wavelet families at the 8th LOD. Since increasing the LOD is not improving the output, only the results related to the 8th LOD are presented.

Table 4-13: Wavelet candidates that produce the best trends for the y angular acceleration

LOD	8
Wavelet	Db3
	Sym4
	Bior1.3
	Coif5

In the second step, the trend (low frequency error), which is the approximation coefficient at the 8th LOD, is removed from the raw y angular acceleration and the residual is computed. The third step is the wavelet de-noising of this residual. The best de-noising procedure (as explained in Section 4.3.6) is to decompose the signal up to the 7th LOD and then reconstruct the signal by the original approximation and modified detail coefficients at the last LOD.

Modified detail coefficients are produced by rescaling the original coefficients with the level-dependent threshold procedure. De-noising results are shown in Table 4-14 for different wavelet families and threshold estimators. As can be seen from this table, the best family, yielding minimum RMS value, is the Debauches family with the Heuristic threshold estimator (shown in blue in this table).

Table 4-14: Selected wavelet families that generate the minimum RMS results for the y angular acceleration

Threshold type	Wavelet	RMS (rad/s^2)
Median	Db4	3.64e-05
SURE	Db8	3.66e-05
Heuristic	Db4	3.64e-05
Minimax	Db4	3.64e-05

Threshold type	Wavelet	RMS (rad/s^2)
Median	Sym7	3.55e-05
SURE	Sym7	3.59e-05
Heuristic	Sym7	3.55e-05
Minimax	Sym7	3.55e-05

Threshold type	Wavelet	RMS (rad/s^2)
Median	Coif5	3.64e-05
SURE	Coif5	3.65e-05
Heuristic	Coif5	3.64e-05
Minimax	Coif5	3.64e-05

Threshold type	Wavelet	RMS (rad/s^2)
Median	Bior1.3	4.01e-05
SURE	Bior1.5	3.93e-05
Heuristic	Bior1.5	3.93e-05
Minimax	Bior1.5	3.92e-05

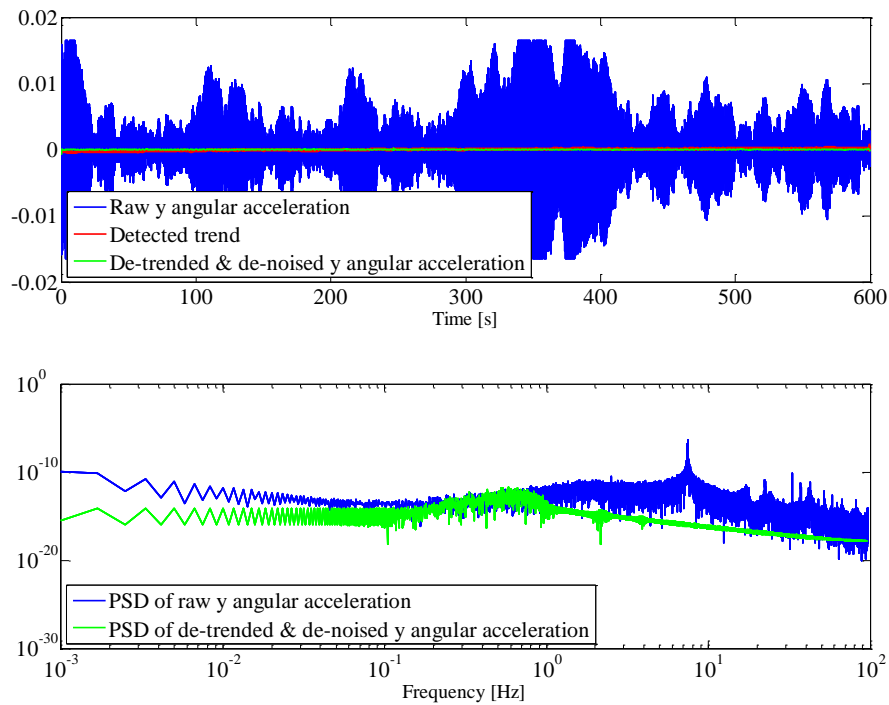


Figure 4-16: The y angular acceleration (blue line), detected trend (red line), and the de-noised and de-trended signal (green line) in rad/s^2 along with their PSDs (bottom plot) in db

Figure 4-16 shows the raw y angular acceleration and the trend (approximation coefficient with Db3 at the 8th LOD) plus the de-trended and de-noise signal along with their PSD. As is clear from

this figure, the noise level is successfully reduced both in the high and in the low frequency parts of the data.

4.8 Wavelet de-trending and de-noising of raw gradient

The same wavelet de-trending and de-noising procedure is also applied to the raw gradiometer output. Table 4-15 shows the best wavelets for producing the wanted trend for different wavelet families at the 8th LOD.

Table 4-15: Wavelet candidates that produces the best trends in gradiometer channel

LOD	8
Wavelet	Db3
	Sym4
	Bior2.4
	Coif2

After removing the trend from the raw gradient, the residual is processed by a new wavelet de-noising analysis. De-noising results are shown in Table 4-16 for different wavelet families and threshold estimators. As can be seen from this table, the best family is the Coiflet family with the Median threshold estimator (shown in blue in this table).

Figure 4-17 shows the raw gradient and the detected trend (approximation coefficient with the Coif2 wavelet at the 8th LOD) plus the de-trended and de-noised signal with the Coif2 wavelet at the 7th LOD along with its PSD. The trend here is assumed as the summation of all systematic effects on the gradiometer output, including the linear and non-linear effects of angular and translationa accelerations of the platform, temperuture fluctuations, and angular velocities squared. The de-trended and de-noised differential mode is considered as a true differential mode. This true value is used in a simulation procedure in the next chapter, where the performance of the gradiometer output will be evaluated after removing the effect of angular velocities squared.

Table 4-16: Selected wavelet families that generate the minimum RMS results for the gradient measurement

Threshold type	Wavelet	RMS (rad/s^2)	Threshold type	Wavelet	RMS (rad/s^2)
Median	Db5	3.45e-08	Median	Sym4	3.29e-08
SURE	Db6	3.58e-08	SURE	Sym4	3.41e-08
Heuristic	Db5	3.53e-08	Heuristic	Sym4	3.31e-08
Minimax	Db5	3.55e-08	Minimax	Sym4	3.31e-08

Threshold type	Wavelet	RMS (rad/s^2)	Threshold type	Wavelet	RMS (rad/s^2)
Median	Coif3	3.21e-08	Median	Bior3.7	3.49e-08
SURE	Coif3	3.35e-08	SURE	Bior5.5	3.62e-08
Heuristic	Coif3	3.22e-08	Heuristic	Bior3.9	3.56e-08
Minimax	Coif3	3.23e-08	Minimax	Bior3.9	3.58e-08

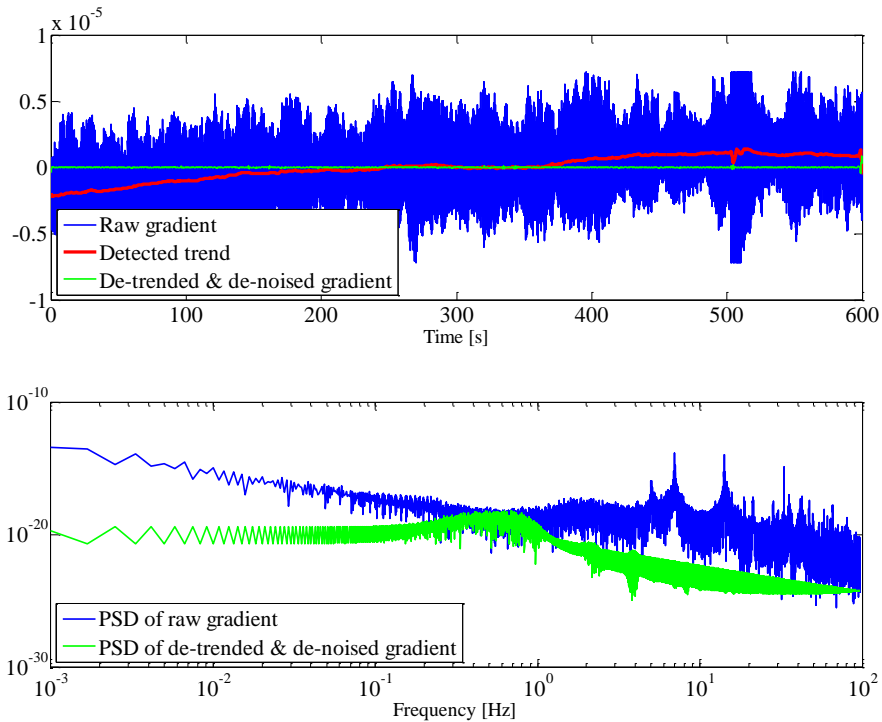


Figure 4-17: The raw differential mode (blue line), detected trend (red line), and the de-noised and de-trended signal (green line) in rad/s^2 along with their PSDs (bottom plot) in db

It is worth mentioning that here instead of the 1 Hz frequency in the gradiometer channel, a desired wavelength for exploration purposes can be used. For airborne applications, there is a relation

between the speed of the flight s , the corresponding spatial resolution x and a specific temporal sampling frequency f_s as (Bruton 2000)

$$x = \frac{s}{f_s} \quad (4-2)$$

This equation can be used to estimate the minimum spatial wavelength that can be recovered for specific flight speed and temporal sampling. Typical wavelengths and amplitudes in mapping salt domes, for oil exploration, and ore bodies were given in Table 1-1. For example, with a typical flight speed of 64 m/s and an ore body of 0.4 km wavelength, the corresponding temporal frequency is 0.2 Hz using Equation (4-2). This frequency in wavelet domain (see Table A-2) corresponds to the 9th LOD. So the 1 Hz frequency can be changed in this section according to the wavelength that one is interested to recover.

4.9 Summary

In this chapter, wavelet de-noising, Wiener low pass filtering, and Butterworth low pass filtering have been applied to x-axis angular acceleration to reduce the high frequency errors of the data. Also, wavelet de-trending and linear regression approaches were applied to mitigate the low frequency portion of the noise in the data.

For the wavelet de-noising, 37 different wavelets have been applied to the x angular accelerations, including the Daubechy, Symlet, Coiflet, and Biorthogonal wavelet families. Four different threshold estimators known as Median, SURE, Heuristic, and Minimax were used to compute the threshold magnitudes. The threshold magnitudes were rescaled by multiplying the noise level with the threshold magnitude. Rescaling was done either by a white noise assumption where the noise level was computed only from the first level of decomposition, or by a non-white noise assumption where the noise level was computed for each LOD. Furthermore, rescaling the noise level was done by assuming the red noise in the data. The results of red noise assumption rescaling were comparable with the results where the third option in de-noising was used (reconstructing with only approximation coefficients). The best de-noising results occurred when the signal was reconstructed with original approximation and modified detail coefficients at the 7th LOD with

non-white noise assumption. The wavelet de-noising of the x angular acceleration in comparison to the Wiener and the Butterworth low pass filtering results are summarized in Table 4-17. The estimated true signal for the Wiener filter in Table 4-17 is the de-noised signal. When the estimated true signal was the output of the Butterworth low pass filtering, the RMS value of the filtered x angular acceleration was increased to $6.95e-05 \text{ rad/s}^2$. This RMS value in comparison to the Butterworth low pass filtering result showed the 28% improvement in reducing the noise level.

Table 4-17: The RMS value achieved by wavelet de-noising of the x angular acceleration with the Coif5 wavelet and the Minimax threshold estimator in comparison to the RMS value achieved by the Wiener and Butterworth low pass filtering methods

Filter typed	RMS (rad/s^2)	Improvement w.r.t original signal with RMS value of 0.0055 rad/s^2
Wavelet de-noising	$5.38e-05$	99.02%
Wiener	$5.02e-05$	99.08%
Butterworth	$9.60e-05$	98.24%

The wavelet de-trending approach has been utilized to mitigate the low frequency error from the angular accelerations. The de-noising procedure was also applied after removing the trend. The wavelet de-noising and de-trending performance showed the 66% improvement in comparison to the performance of the linear regression and the Butterworth low pass filtering procedure. The improvement with respect to original signal by wavelet de-trending and de-noising procedure is 99.44% while the improvement by Gedex procedure is 98.33%.

The RMS value of the signal after applying the wavelet de-trending and then the Wiener low pass filtering showed 16% improvement in reducing the noise level in comparison to the results using the wavelet de-trending and de-noising approach. The reason for this improvement is because the true signal used as the input to the Wiener filter was the result of wavelet de-trending and de-noising approach. The Wiener low pass filtering performance depends on by the fact how the estimated true signal is selected.

The same filtering techniques were additionally applied to the y angular acceleration and differential mode observation from the static run of the system. Table 4-18 shows which techniques are known to provide the smallest RMS values for the noise in the differential mode, and x and y

angular accelerations. The same technique can then be applied on the data from the dynamic run of the system. More analysis on this subject will be given in Chapter 5.

Table 4-18: Filtering approaches that produced the minimum RMS results for the differential mode, x and y angular accelerations

Noisy signal	Wavelet for de-trending	Wavelet for de-noising	Threshold type
Differential mode	Coif2	Coif3	Median
x angular acceleration	Coif5	Coif5	Median
y angular acceleration	Sym4	Sym7	Heuristic

Chapter 5: Quality assessment of the gradiometer output

As was discussed in Chapter 2 and 3, the gradiometer output includes many error sources, such as angular and translational sensitivities, angular velocities squared, temperature sensitivity, fundamental or intrinsic gradiometer error, axis misalignment of the pivot axes of the two test masses, and output non-linearity. Among all these errors the major focus is given to the effects of angular velocities squared in this study. When angular accelerations are available, angular velocities squared can be calculated and ultimately the gradiometer output can be corrected for this error. However, angular accelerations are noisy and their error analysis was discussed in Chapter 4. The techniques that were applied to the static data set will be applied to the dynamic data set in this chapter. Firstly, using the dynamic data set, the high quality angular accelerations are obtained and then the high quality angular velocities squared are calculated. Eventually, the effect of angular velocities squared will be removed from the gradiometer output. Furthermore, the gradient data is evaluated after removing the angular velocities squared term. In order to assess the performance of the airborne gradiometry, it is very common to compare the gradients with upward-continued-ground-based gravity measurements (Boggs and Dransfield 2004, Murphy 2004). However, such control data are not available for this research work. Therefore, the true gradient will be simulated at the end of this chapter for this purpose. The performance of the angular gradiometer will then be evaluated by error propagation using the single-input-single-output system.

5.1 Removing angular velocities squared from angular gradiometer measurements

Differential mode (dm) is considered as one of the gradiometer outputs, which contains the gradient difference component in it. As was shown in Chapter 3, the x-axis OQR can be mathematically expressed by Equation (3-9). Since the output of the z-axis OQR is available for this thesis, we rewrite the equations of angular motions for the z-axis OQR. The z-axis OQR is illustrated in Figure 5-1.

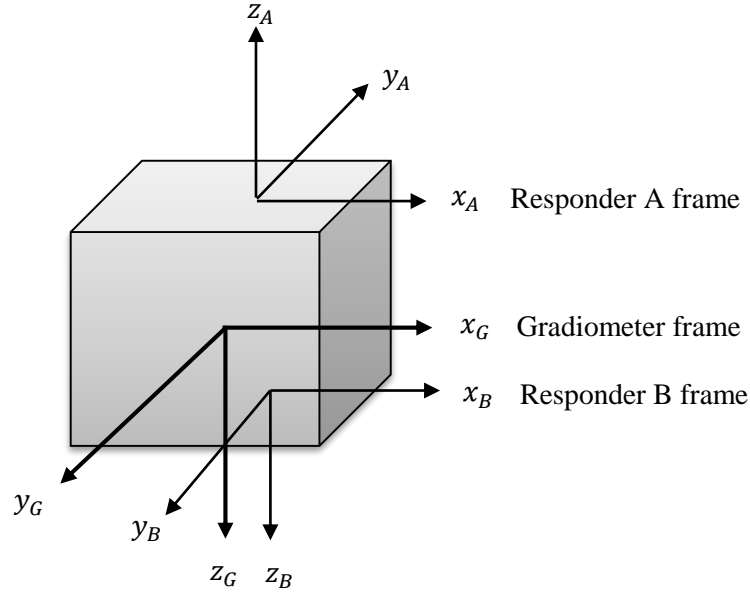


Figure 5-1: Configuration of the z-axis OQR gradiometer with its coupled z-axis angular accelerometers

For brevity, we don't repeat the derivation like it was done in Chapter 3 and we only write the z-axis OQR measurement in the gradiometer frame with the following equation:

$$dm = (\tau_{z,A} - \tau_{z,B}) = 2I_{xy,A}[(\Gamma_{xx} - \Gamma_{yy}) + \Omega_y^2 - \Omega_x^2] \quad (5-1)$$

Equation (5-1) shows that the gradiometer measurement contains not only the wanted term, i.e., the true gradient difference $(\Gamma_{xx} - \Gamma_{yy})$, but also two unwanted terms that are the angular velocities squared in x and y directions, Ω_x^2 and Ω_y^2 . The true gradient difference $(\Gamma_{xx} - \Gamma_{yy})$ can be computed as follows:

$$(\Gamma_{xx} - \Gamma_{yy}) = \frac{(\tau_{z,A} - \tau_{z,B})}{2I_{xy,A}} - (\int \dot{\Omega}_y dt)^2 + (\int \dot{\Omega}_x dt)^2 \quad (5-2)$$

It is noteworthy that the angular acceleration measurements in x and y axes, $\dot{\Omega}_x$ and $\dot{\Omega}_y$, are used in this equation instead of the angular velocities because the angular velocities were not directly measured for this purpose. Also, the inertial moment of the responder A, $I_{xy,A}$ in this equation, can be computed with the following relation (Matthews 2002):

$$I_{xy} = \frac{m}{2}(l^2 - b^2) \quad (5-3)$$

where, $m = 0.677$ is the test bar mass in kg , $b = 2.4e - 2$ is the width of the bar in m and $l = 10.2e-2$ is the length of the bar in m (Moody 2011). So, the unit of inertial moment is in $Kg.m^2$. Dividing the differential mode in rad/s^2 by the inertial moment in $Kg.m^2$, needs a coefficient to account for this unit conversion. Since the effect of the inertial moment is only shown as a scaled quantity and there is no access to this coefficient for this research, all illustrated figures throughout this chapter are normalized versions of the true gradient.

The block diagram in Figure 5-2 shows how angular velocities squared can be removed from differential mode and consequently how the true gradient is produced.

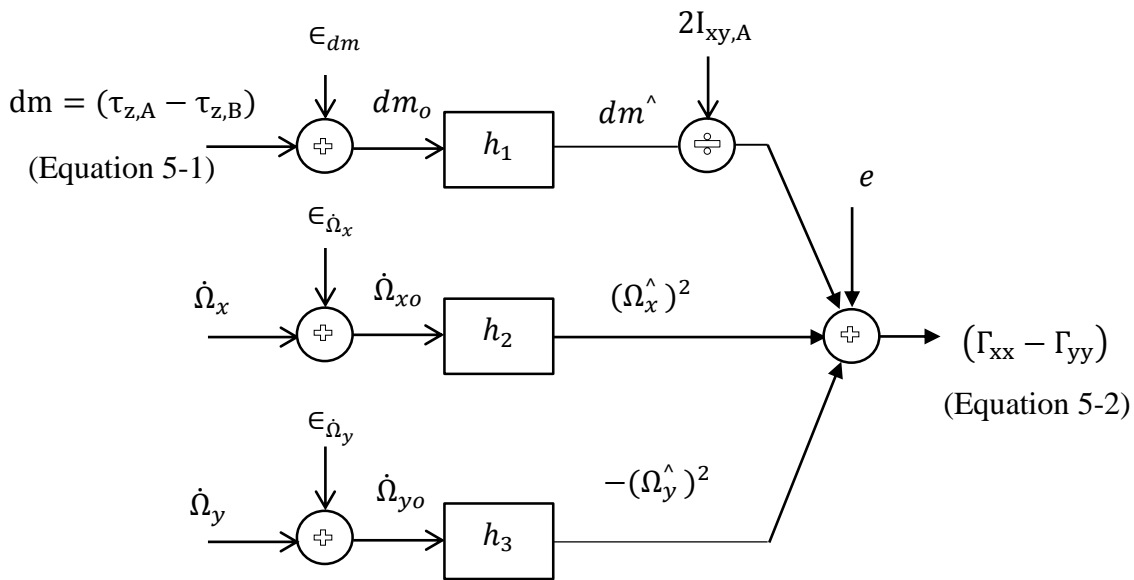


Figure 5-2: A three-input, single-output system with noises for the OQR type gradiometer

As can be seen from this diagram, the gradiometer output that contains the two unwanted angular velocities squared plus some random noise ϵ_{dm} are combined to generate the observed differential mode dm_o . The two observed angular accelerations $\dot{\Omega}_{xo}$ and $\dot{\Omega}_{yo}$ are generated with the combination of their true values, $\dot{\Omega}_x$ and $\dot{\Omega}_y$ and their corresponding random noises $\epsilon_{\dot{\Omega}_x}$ and $\epsilon_{\dot{\Omega}_y}$. These random noises can be removed from all observed quantities by defining a proper transfer

function h_i (any filtering procedures, e.g., wavelet). Then by dividing the estimated differential mode dm^{\wedge} by the inertial moment constant and adding the estimated (corrected) angular velocities squared to the scaled dm^{\wedge} , the true gradient difference ($\Gamma_{xx} - \Gamma_{yy}$) is produced as illustrated with in Figure 5-2. This figure is a very simple depiction of the gradiometer output since, as discussed in Chapters 2 and 3, there are other error sources that influence the gradiometer measurement. However, the major focus here is the effect of angular velocities squared.

The raw and the filtered x and y angular accelerations are illustrated in Figure 5-3 and Figure 5-4, respectively. Also, angular velocities squared derived from raw and filtered x and y angular accelerations are illustrated in Figure 5-5 and Figure 5-6, respectively. Selected wavelets for de-noising and de-trending of the static angular accelerations $\hat{\Omega}_{xo}$ and $\hat{\Omega}_{yo}$ were listed in Table 4-18, which they applied on the dynamic x and y angular acceleration in this section.

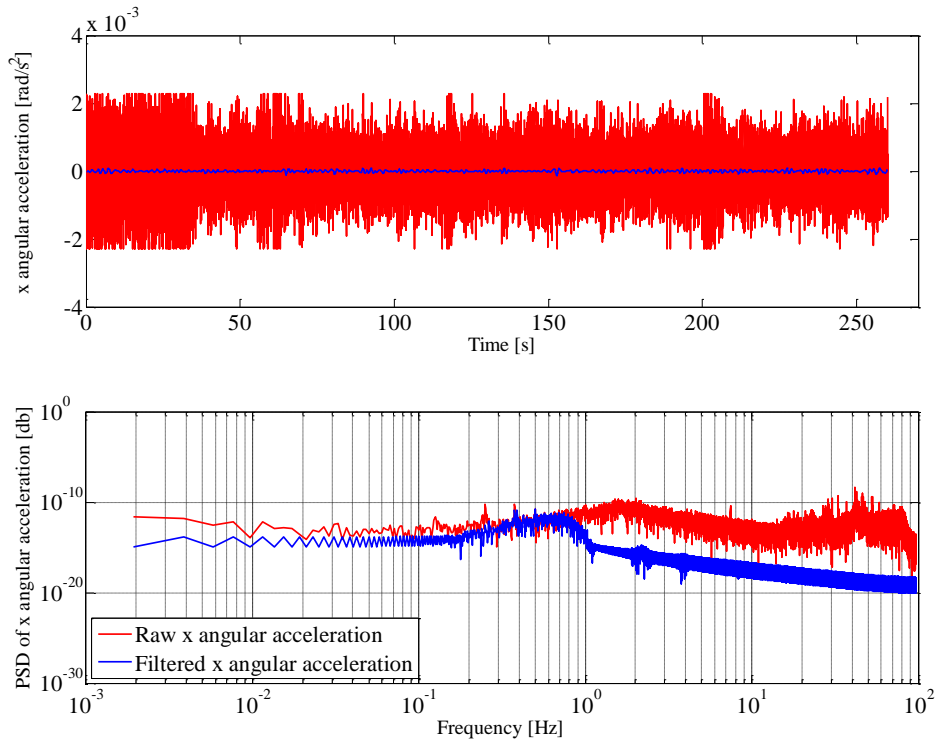


Figure 5-3: Raw and filtered x angular accelerations along with their PSDs using dynamic data

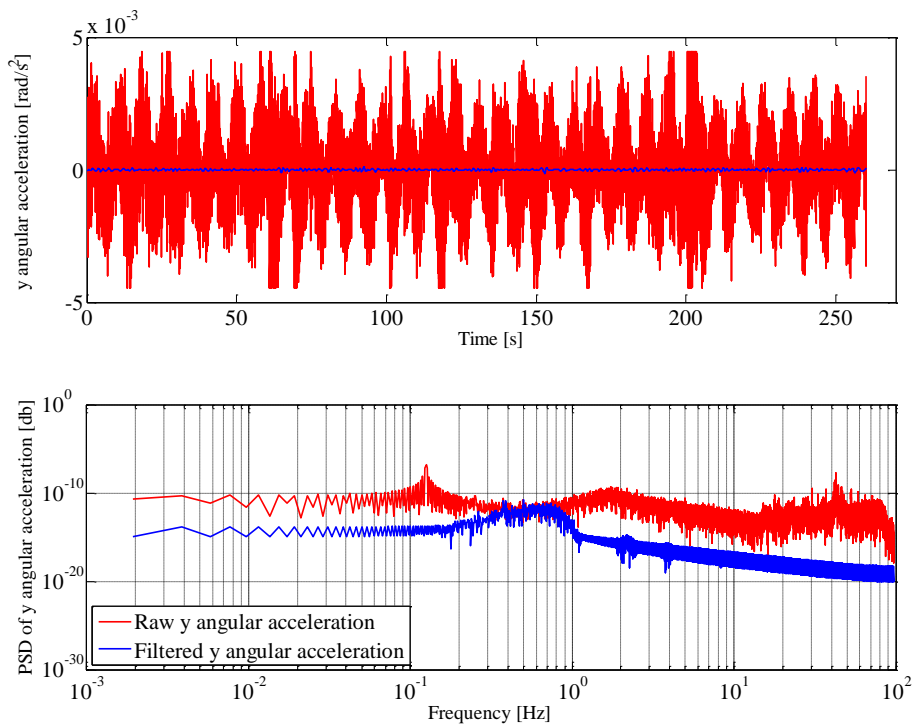


Figure 5-4: Raw and filtered y angular accelerations along with their PSDs using dynamic data

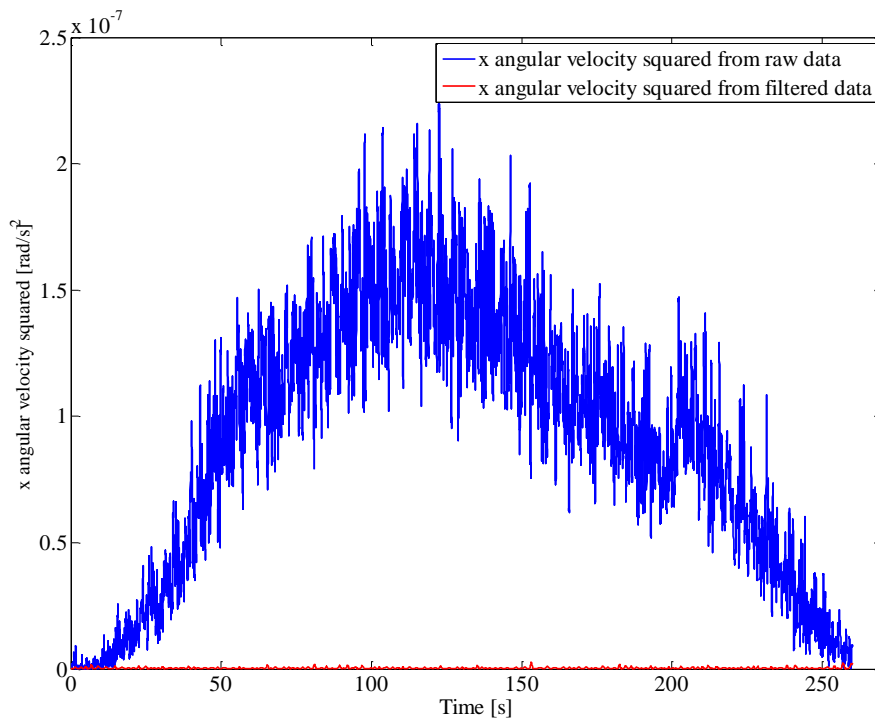


Figure 5-5: X angular velocities squared derived from raw and filtered angular accelerations

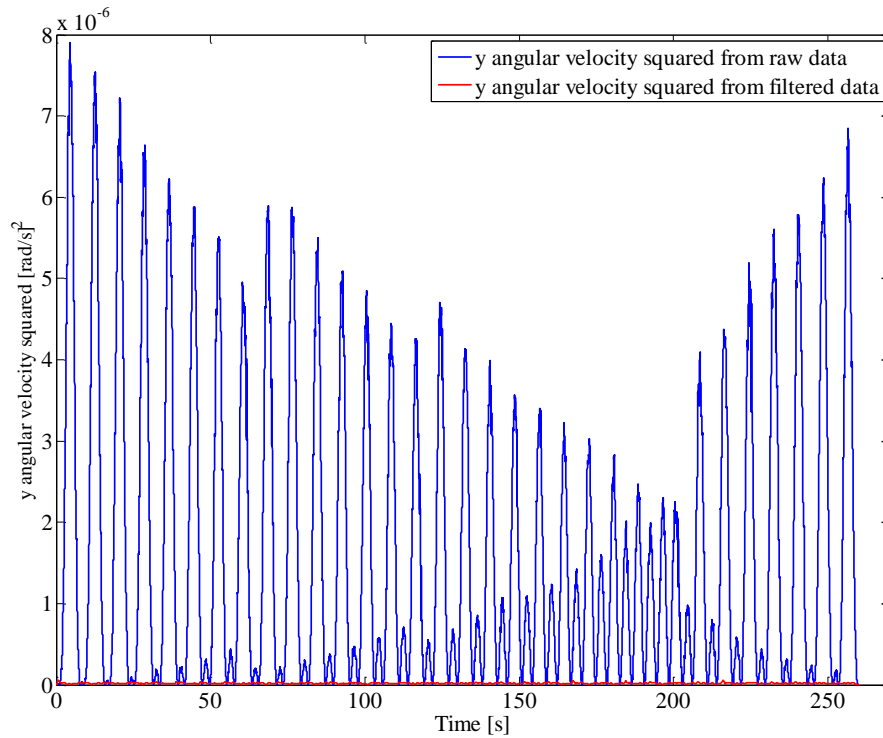


Figure 5-6: Y angular velocities squared derived from raw and filtered angular accelerations

The effect of angular velocities squared derived from the raw data is -1590 Eötvös (mean value) while the same effect derived from filtered data is -20 Eötvös. The raw gradient after removing the -1590 Eötvös effects is the blue plot in Figure 5-7. The amplitude of the blue plot fluctuates between -10000 Eötvös to 5000 Eötvös in time domain and there is a bias in low frequency part of the signal in frequency domain. However, the raw gradient after removing the -20 Eötvös effect (green plot) corresponds strongly to the raw gradient (red plot) as shown in Figure 5-7. The reason is that there are still a large numbers of systematic effects that influence the gradiometer channel. In order to remove these systematic effects, the wavelet de-trending of the gradiometer output is necessary. The result is depicted in Figure 5-8. The raw gradient after de-trending and de-noising (green plot) is called the true differential mode. The effects of angular velocities squared derived from the filtered data is then removed from true differential mode and the result is called true gradient (orange plot in Figure 5-8). Both of these true values will be used in the next section to evaluate the final accuracy of the gradient through a simulation procedure.

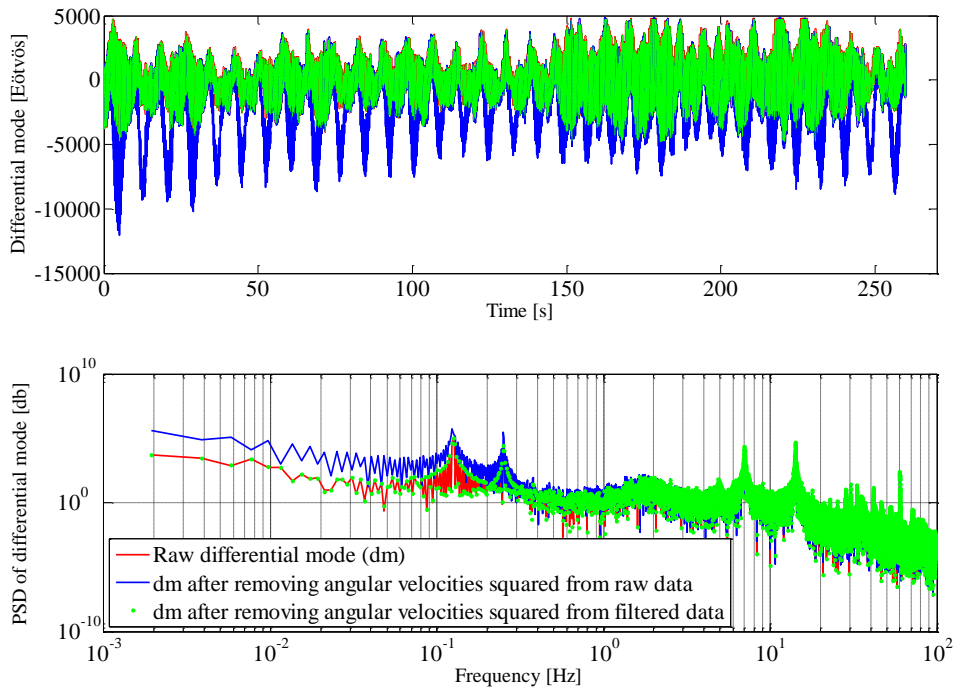


Figure 5-7: Raw gradient, raw gradient after removing the angular velocities squared derived from raw data, raw gradient after removing the angular velocities squared derived from filtered data in time and frequency domains

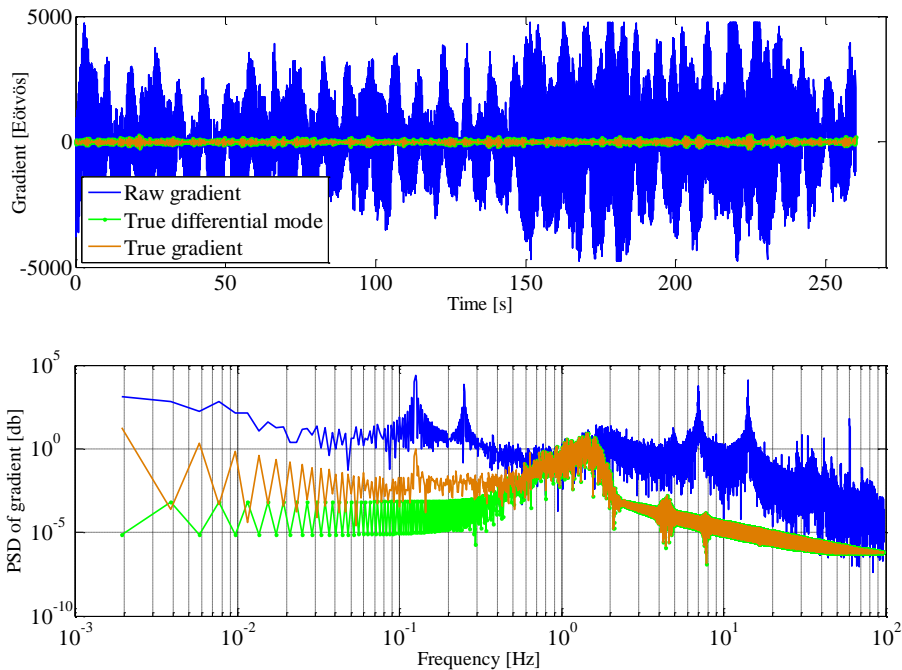


Figure 5-8: True gradient after removing both the angular velocities squared and the rest of the errors by the wavelet filtering in time and frequency domains

It is noteworthy that the true gradient here is the result of the wavelet de-trending at 7th LOD and the wavelet de-noising at 6th LOD. So, the frequency band of interest is in 1 to 2 Hz, which corresponds to the geological signal in a 64 to 128 *m* wavelength (assuming a flight speed of 64 *m/s*). The filtered angular accelerations used to derive angular velocities squared here is the result of the wavelet de-trending at 8th LOD and the wavelet de-noising at 7th LOD (corresponds to frequencies in 0.5 to 1 Hz).

For mineral exploration, the measuring accuracy of the superconductive angular gradiometer should be less than 1 Eötvös which meets the industry need for recovering the wavelength in a 50 to 100 *m* (Kann 2004). It is going to test this requirement in the next section through the simulation procedure.

5.2 Performance of the superconductive angular gradiometer

Any observable can be modeled with two major components. The first one uses a deterministic model in which the behavior of the observations is modelled by known mathematical expressions. The second one uses a stochastic model that accounts for the residual effects after removing the deterministic part from observations. Deterministic and stochastic models are often referred to as trend $t(\tau)$ and residual $r(\tau)$ in literature (Vanicek and Krakiwsky 1986). The trends are predictable; however, the residuals account for any uncertainty in the observations and are unpredictable random processes. Mathematical tools such as statistics filtering, correlation functions and spectral density functions are used to model stochastic components (Craymer 1998). The OQR type superconductive angular gradiometer is influenced by many systematic errors (see Chapter 3). The only systematic effects that were removed from the gradiometer channel were the angular velocities squared (see previous section). The gradiometer output is influenced by random noise that was divided into two groups: white noise and non-white noise; see Chapter 4.

Due to lack of real measurements and control data the accuracy of the gradient is evaluated through a simulation procedure. As is clear from Equation (5-2), the true gradient is the combination of three terms, namely the differential mode and the angular accelerations in the x and y directions.

To assess the sensitivity of the true gradient with respect to any of these parameters, the true signal and random noise terms for each parameter must be simulated. The true signal for each of these parameters is the output of the wavelet de-trending and de-noising procedures. The random noise for this simulation is assumed to be colored noise. The colors of noise describes the power spectrum of the noise in the frequency domain. According to Pilgram and Kaplan (1998), noise power spectrum has the form of $\frac{1}{f^\alpha}$, where f is the frequency. For example, white noise has zero mean, constant variance and is uncorrelated in time. It has a constant power spectrum over the whole frequency band with $\alpha = 0$. Red and pink noises have also zero mean and constant variance but they are correlated in time. The red noise power spectrum has more power in low frequencies than the pink noise. Power spectrum of purple and blue noises have more power in high frequencies. Colored noises and their frequency contents are listed in Table 5-1. Figure 5-9 shows the PSD of the different colored noises.

Table 5-1: Noise colors (Carter 2008)

<i>Colors</i>	<i>Frequency content</i>
Purple	$\frac{1}{f^{-2}}$ ($\alpha = -2$)
Blue	$\frac{1}{f^{-1}}$ ($\alpha = -1$)
White	$\frac{1}{f^0}$ ($\alpha = 0$)
Pink	$\frac{1}{f}$ ($\alpha = 1$)
Red/Brown	$\frac{1}{f^2}$ ($\alpha = 2$)

Before adding random noise to the true differential mode and the angular accelerations, it is necessary to figure out what type of random noise exists in these measurements. For this purpose first the trend is removed, by the wavelet de-trending method, from all of these measurements to create the residuals. Then the PSDs of the residuals were calculated and depicted in Figure 5-10. Now it is required to figure out which colored noise shows similar behaviour to the residuals. It is clear from Figure 5-10 that the behavior of both differential mode and y angular acceleration are similar to the behaviour of the pink and red noises.

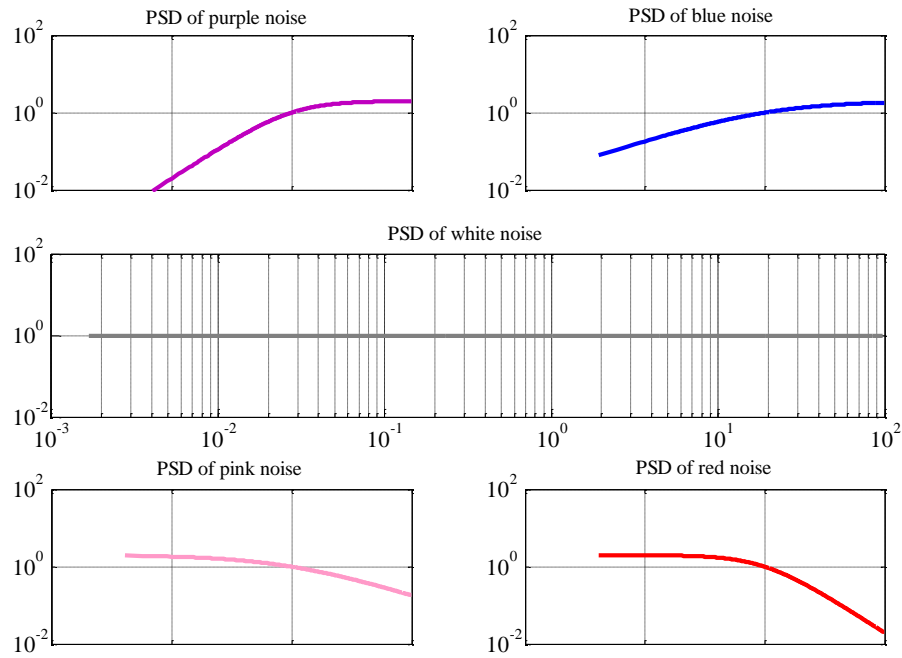


Figure 5-9: PSD of the different kinds of noise

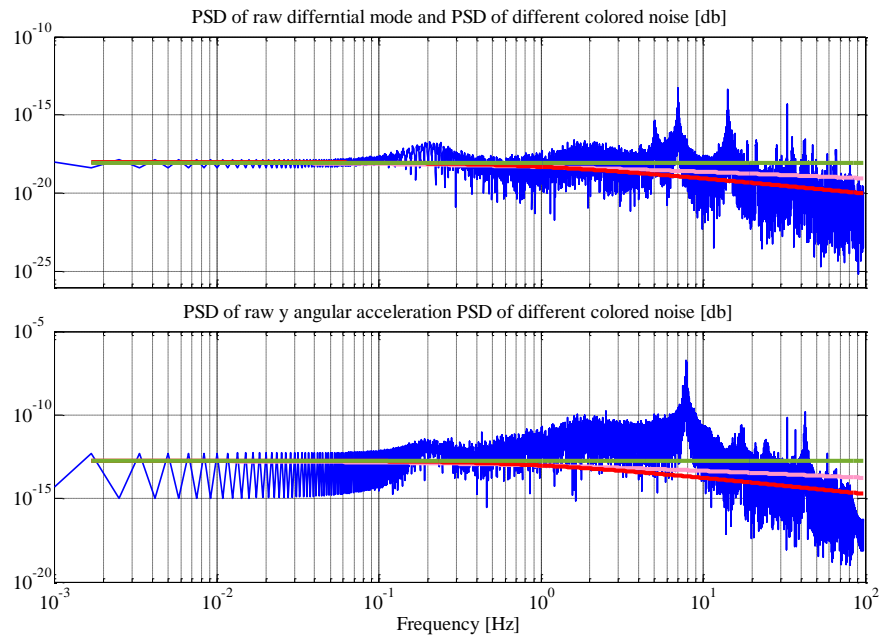


Figure 5-10: PSD of the raw differential mode and the raw y angular accelerations after de-trending along with the PSD of the different noise types (white noise (gray line), pink noise (pink line), and red noise (red line))

Since the static data is considered as an indicator of the noise floor throughout this thesis, it has been used to create PSDs in Figure 5-10, as well. Since the behaviour of the x angular acceleration is similar to the y angular acceleration, the PSD of the x angular acceleration is not depicted in this figure.

The random errors in the gradiometer channel are typically modeled as white noise at the higher frequencies or red noise at the lower frequencies (Moody 2011, Jekeli 2006, Moody et al., 1988). Thus, in the next section the gradient and angular accelerations will be simulated by adding white, pink, and red noise to the true data.

5.2.1 *Simulating the true gradient*

Recalling Equation (5-2), for creating the simulated true gradient it is needed to simulate three terms, namely the differential mode (dm) and the angular accelerations in x and y directions ($\dot{\Omega}_x$ and $\dot{\Omega}_y$). The simulation is done by adding random noise to the true values of dm, $\dot{\Omega}_x$ and $\dot{\Omega}_y$. The true values of $\dot{\Omega}_x$, $\dot{\Omega}_y$, and dm are the result of the wavelet de-trending and de-noising of the real dynamic observations, which was depicted in Figures 5-3, 5-4, and 5-8 in Section 5.1. The simulated parameters can be written as:

$$\begin{aligned}
 dm_{sim}(t) &= dm_{true}(t) + \epsilon_{dm}(t) \\
 \dot{\Omega}_{xsim}(t) &= \dot{\Omega}_{xtrue}(t) + \epsilon_{\dot{\Omega}_x}(t) \\
 \dot{\Omega}_{ysim}(t) &= \dot{\Omega}_{ytrue}(t) + \epsilon_{\dot{\Omega}_y}(t)
 \end{aligned}
 \tag{5-4}$$

$\epsilon_{dm}(t)$, $\epsilon_{\dot{\Omega}_x}(t)$, and $\epsilon_{\dot{\Omega}_y}(t)$ are random processes characterized by different variances and noise types such as white, pink and red. The values of the simulated variances came from the static data, which provide the noise floor. The standard deviations of the static data before and after wavelet filtering are shown in Table 5-2.

Table 5-2: Mean and standard deviation of the x and y angular accelerations $\dot{\Omega}_x, \dot{\Omega}_y$ and differential mode observation dm from the static data before and after wavelet filtering

Parameter	Before wavelet analysis (rad/s ²)		After wavelet analysis (rad/s ²)	
	Mean	Sd	Mean	Sd
$\dot{\Omega}_x$	-6.50e-08	5.45e-03	9.07e-08	3.08e-05
$\dot{\Omega}_y$	8.39e-09	3.01e-03	-2.36e-07	3.55e-05
dm	-1.59e-8	2.28e-06	1.22e-10	3.21e-08

These values shown that the standard deviation of the gradient is smaller than that of the angular accelerations, and the standard deviation of the angular accelerations in x and y channels are in the same range. Thus, by assuming the Standard deviation (Sd) in the ranges of 3e-01 to 3e-09, different realizations are generated with the following three assumptions (in all realizations it is assumed that both angular accelerations have equal Sd):

- 1- The same standard deviation for all three parameters
- 2- The standard deviation of the differential mode is bigger than that of the two angular accelerations
- 3- The standard deviation of the differential mode is smaller than that of the two angular accelerations

Table 5-3 summarizes the different Sds that were selected based on the above three assumptions for creating different realizations.

Table 5-3: Different Sds for creating different realizations (rad/s²)

Assumption (1) Sd(dm)=Sd($\dot{\Omega}_x, \dot{\Omega}_y$)	Assumption (2) Sd(dm)<Sd($\dot{\Omega}_x, \dot{\Omega}_y$)	Assumption (3) Sd(dm)>Sd($\dot{\Omega}_x, \dot{\Omega}_y$)
Sd = 3e-01	Sd($\dot{\Omega}_x, \dot{\Omega}_y$) = 3e-3	Sd(dm) = 3e-3
Sd = 3e-03	Sd(dm) = 3e-05	Sd($\dot{\Omega}_x, \dot{\Omega}_y$) = 3e-05
...	Sd(dm) = 3e-06	Sd($\dot{\Omega}_x, \dot{\Omega}_y$) = 3e-06
Sd = 3e-09	Sd(dm) = 3e-07	Sd($\dot{\Omega}_x, \dot{\Omega}_y$) = 3e-07
	Sd(dm) = 3e-08	Sd($\dot{\Omega}_x, \dot{\Omega}_y$) = 3e-08

Some produced realizations made by the above assumptions are represented in this section. For example, produced realizations by the first assumption where all three parameters have the same S_d are depicted in Figures 5-11 and 5-12. Ensemble of the true gradients by the second assumption is produced with white, pink and red noise assumptions. However, only the simulated result with the pink noise assumption is depicted in Figure 5-13.

It seems that when the S_d s are in the range of 10^{-1} to 10^{-4} the simulated true gradients are neither similar to the raw gradient nor to the true gradient in Figure 5-8. Thus, most of the realizations depicted in plots (A) and (B) in Figure 5-11, Figure 5-12 and Figure 5-13 will be ignored in this study. However, when the S_d s are selected in the range of 10^{-5} to 10^{-9} (plots (C) and (D) in Figures 5-11, 5-12, 5-13), the simulated true gradients are either similar to the raw or the true gradient. Therefore, all the simulated true gradient similar to (C) and (D) plots in these figures are used in the next section to evaluate the performance of the gradiometer output.

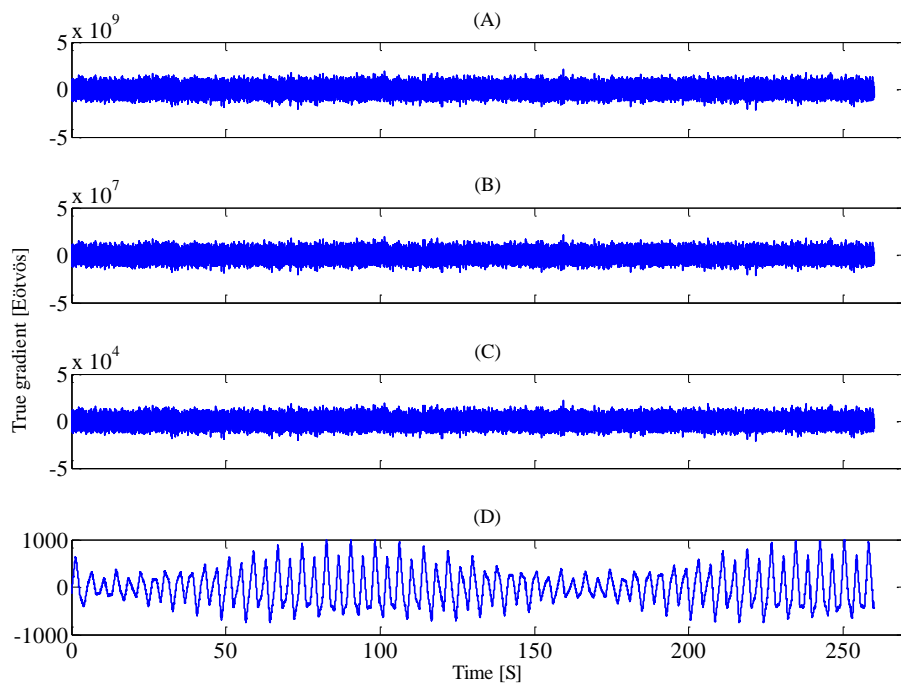


Figure 5-11: Simulated true gradient with equal standard deviation assumption (white noise assumption). S_d of all terms in rad/s^2 : (A) $3e-01$, (B) $3e-03$, (C) $3e-06$, and (D) $3e-09$

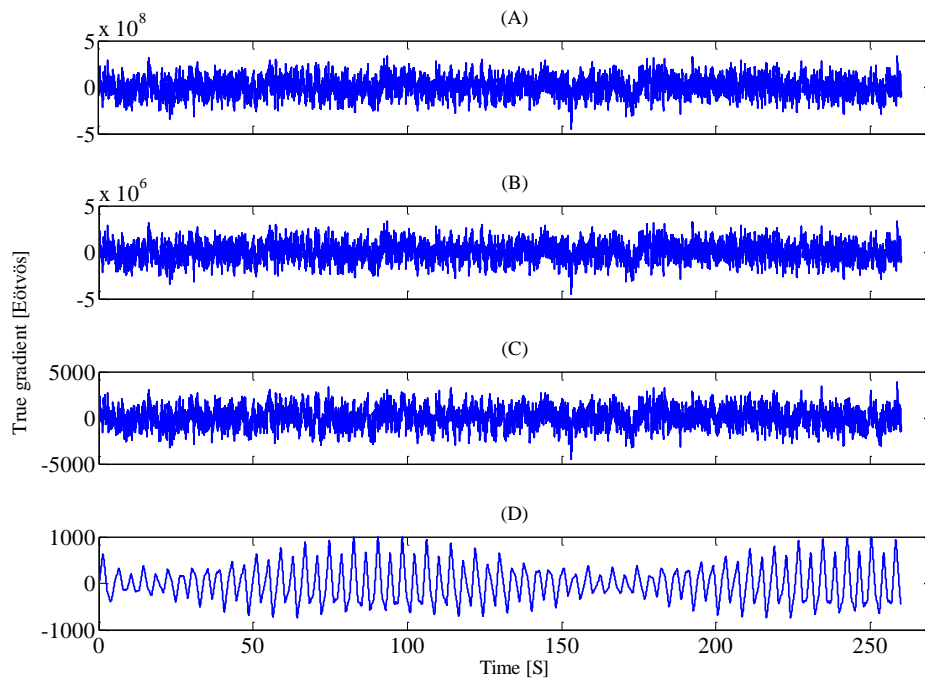


Figure 5-12: Simulated true gradient with equal standard deviation assumption (red noise assumption). Sd of all terms in rad/s^2 : (A) $3e-01$, (B) $3e-03$, (C) $3e-06$, and (D) $3e-09$

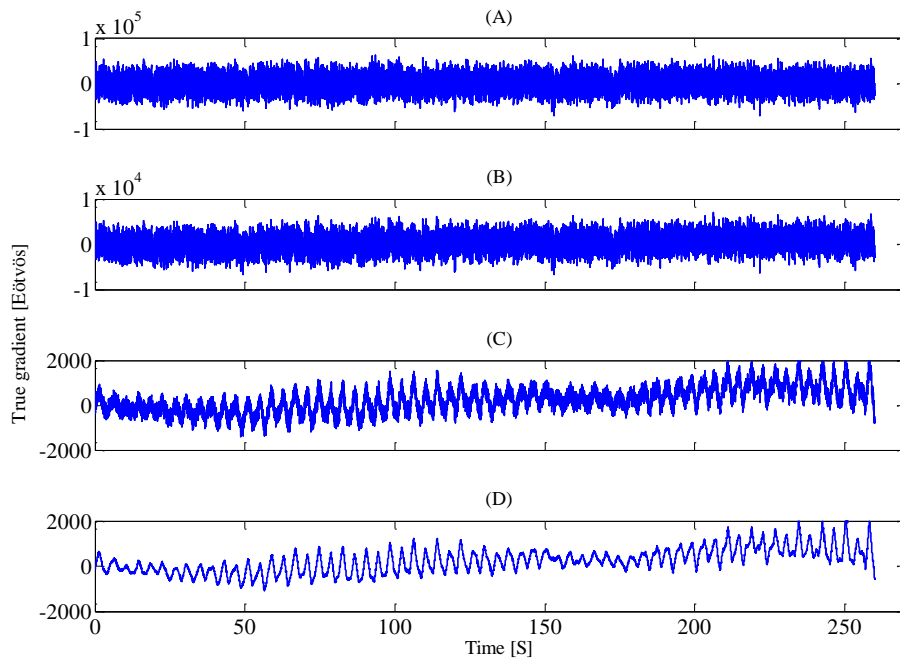


Figure 5-13: Simulated true gradient with the second noise assumption (pink noise assumption). Sd of the accelerations in all cases is $3e-3 rad/s^2$. Sd of the differential mode in rad/s^2 : (A) $3e-5$, (B) $3e-6$, (C) $3e-7$, and (D) $3e-8$

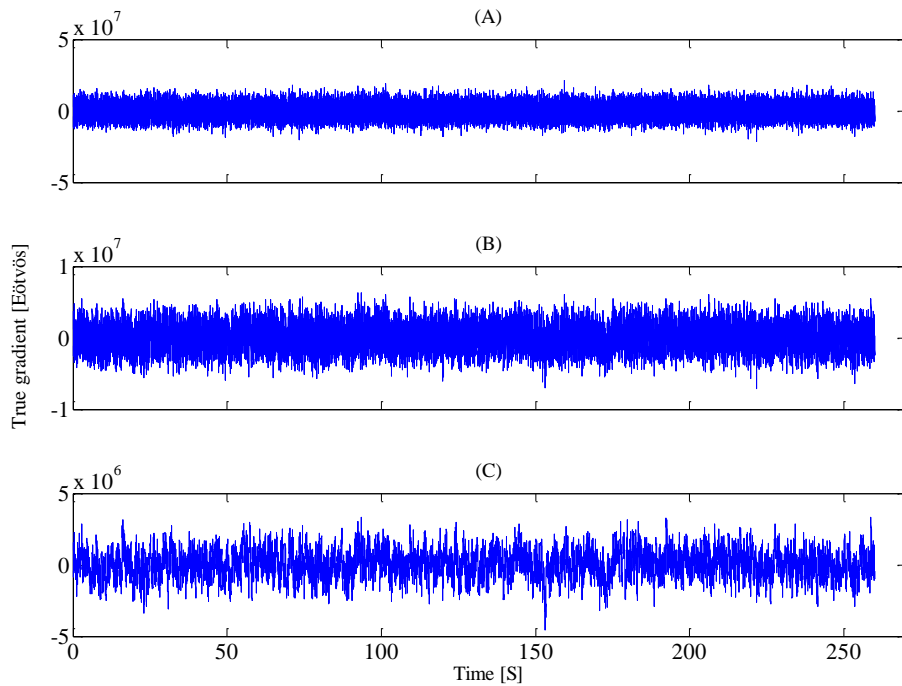


Figure 5-14: Simulated true gradient with the third noise assumption. Sd of the differntial mode in all cases is $3e-3 \text{ rad/s}^2$. Sd of the angular acceleration is $3e-5 \text{ in rad/s}^2$. The noise type: (A) white (B) pink, and (C) red

Produced realizations by the third assumption are depicted in Figure 5-14. In this case the Sd of the differential mode is smaller than that of the angular accelerations. It seems that the third assumption does not provide reliable simulated signals for our process because by decreasing the Sd of the accelerations, the amplitude of the true gradients is not changed for almost all cases with white, pink, and red noise assumptions. However, to consider some extreme situations in evaluating the performance of the gradiometer, these simulated true gradeints will be processed in the next sub-section, as well.

5.2.2 Error propagation in a single-input, single-output system of the gradiometer channel

Figure 5-15 illustrates error propagation when there is a single input and single output for the system. This system works under the assumption of no time varying parameters (statistical characteristics do not change over time). That is the only random noise ϵ that can be added to the true input x is the white noise case. The output of the system y is the combination of the estimated

signal \hat{y} and system output noise e . By defining such a system in Figure 5-15, it is possible to determine the estimated output in terms of the system transfer function h . Moreover, the PSD of the estimated noise P_{ee} is determined in a least-squares sense by minimizing the squared difference between the estimated output signal \hat{y} and desired output signal y . The system can be expressed mathematically in time domain as (Sideris 1996):

$$y = (x + \epsilon) * h + e \quad (5-5)$$

where $*$ indicates the convolution operator.

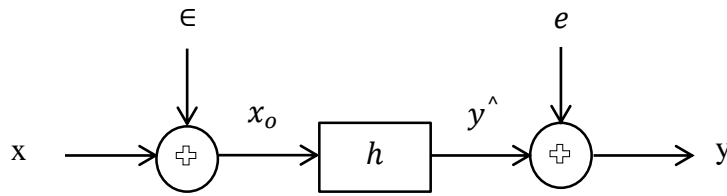


Figure 5-15: Propagation of error in a single-input, single-output system in gradiometer channel

The equivalent system equation in the frequency domain is written as follows:

$$F\{y\} = (F\{x\} + F\{\epsilon\})F\{h\} + F\{e\} \quad (5-6)$$

where F is the Fourier transform operator.

The PSD of the noise P_{ee} can be computed by solving the Equation (5-6) for $F\{e\}$ and then multiplying it by its complex conjugate $F^*\{e\}$. Finally by taking the expectation E from this multiplication, the PSD of the noise is derived:

$$P_{ee} = E[F(e)F^*(e)] \quad (5-7)$$

$$P_{ee} = P_{yy} - HP_{yx} - H^*P_{xy} + H(P_{xx} + P_{\epsilon\epsilon})H^* = P_{yy} - P_{y\hat{y}} \quad (5-8)$$

If no correlation is assumed between the input noise with input and output signals, optimum frequency response function can be computed by taking the derivative of Equation (5-8) with respect to H and then setting it to zero. This optimum frequency response function is then:

$$H = \frac{P_{xy}}{P_{xx} + P_{\epsilon\epsilon}} \quad (5-9)$$

When the the desired output signal is x itself (like the case here where the x is true gradient), Equation (5-9) is the Wiener filter frequency response as shown in Appendix A with Equation (A-15). Based on Parseval's theorem, integrating the PSD generates the mean squared value. Since the P_{ee} is the PSD of the difference between the true signal y and the estimated signal y^\wedge , the following relation can be used to compute the variance of the output system (Bendat and Piersol 1985):

$$\int_{-\infty}^{\infty} P_{ee} dt = \text{mean squared error}[y^\wedge] = [E(y^\wedge - y)]^2 = \text{Var}[y^\wedge] + (b[y^\wedge])^2 \quad (5-10)$$

So if the integration is taken from P_{ee} and the bias b is removed, the variance is calculated as below:

$$\text{Var}(y^\wedge - y) = \int_{-\infty}^{\infty} P_{ee} dt - (b[y^\wedge])^2 \quad (5-11)$$

It is noted that the bias b (systematic error) was removed from the gradient data before doing the simulation. So, the bias is zero or negligible in this work and the variance is equal to the mean square error.

Some of the simulated true gradient signals (in total 38 time series) made in Section 5.2.1 with the white noise assumption are considered as the input measurement x_o in this analysis. All these signals were processed with Wiener low pass filtering. Eventually, the estimated or filtered signal is generated along with its noise variance using Equation (5-11).

Table 5-4: Accuracy of the filtered simulated true gradient with equal weight noise assumption

Sd of accelerations (rad/s ²)	Sd of differential mode (rad/s ²)	Sd of (y [^] - y) (Eötvös)
3e-03	3e-03	19.51
3e-04	3e-04	21.65
3e-05	3e-05	12.11
3e-06	3e-06	1.26
3e-07	3e-07	0.07
3e-08	3e-08	0.02
3e-09	3e-09	0.002

Table 5-4, Table 5-5 and Table 5-6 show the results of this analysis with the first, second, and third noise Sd assumptions, respectively. In all these tables when the Sd of accelerations and differential mode are in the range of 10^{-3} to 10^{-6} , more realistic results are produced for the given observations in this research. However, when the ranges are in order of 10^{-5} to 10^{-8} , more realistic results are produced for the filtered observations. By comparing the numbers in these tables, the smallest Sd is 0.002 Eötvös that occurs when both differential mode and angular accelerations have equal noise Sd in the order of $3e-09 \text{ rad/s}^2$ showed in blue in Table 5-4.

Table 5-5: Accuracy of the filtered simulated true gradient when the noise Sd of the differential mode is smaller than angular accelerations

Sd of accelerations (rad/s^2)	Sd of differential mode (rad/s^2)	Sd of ($y^{\wedge} - y$) (Eötvös)
3e-03	3e-04	21.50
	3e-05	15.66
	3e-06	10.47
	3e-07	9.87
	3e-08	9.81
	3e-09	9.81
3e-04	3e-05	12.49
	3e-06	1.96
	3e-07	0.81
	3e-08	0.73
	3e-09	0.73
3e-05	3e-06	1.31
	3e-07	0.13
	3e-08	0.06
	3e-09	0.05
3e-06	3e-07	0.08
	3e-08	0.01
	3e-09	0.01
3e-07	3e-08	0.01
	3e-09	0.001
3e-08	3e-09	0.002

Based on the available data sets, the Sd of the differential mode are smaller than the angular accelerations. Table 5-5 shows the results of this kind of situation. Moreover, the sensitivity of the gradiometer output is tested for some extreme situations. The extrem cases occur when the Sd of

the differential mode is bigger than the angular accelerations. Table 5-6 shows the results of these extreme situations.

Table 5-6: Accuracy of the filtered simulated true gradient when the noise Sd of the differential mode is bigger than angular accelerations

Sd of differential mode (rad/s^2)	Sd of accelerations (rad/s^2)	Sd of ($y^{\wedge} - y$) (Eötvös)
3e-05	3e-06	12.07
	3e-07	12.06
	3e-08	12.06
	3e-09	12.06
3e-06	3e-07	1.26
	3e-08	1.27
	3e-09	1.26
3e-07	3e-08	0.07
	3e-09	0.07
3e-08	3e-09	0.02

By comparing the Table 5-5 and Table 5-6, it is obvious that the output of the gradiometer is more sensitive to the differential mode errors than the errors in the angular accelerations. That is, by decreasing the Sd of the differential mode and taking the Sd of angular accelerations as a constant parameter, the accuracy of the true gradient is decreasing (see Table 5-5). However, when the Sd of the differential mode was assumed constant and the Sd of the accelerations were decreased, there was no improvement in the accuracy of the estimated true gradient as can be seen in Table 5-6. Again, the most accurate results in both Table 5-5 and Table 5-6 have been recorded when both accelerations and differential mode accuracies were in certain ranges, such as 10^{-5} to $10^{-9} rad/s^2$.

The Sd of the raw angular accelerations and gradient are in the range of 10^{-3} and 10^{-6} , respectively. Therefore, it can be concluded that the accuracy of the system output using the raw observations is 10.47 Eötvös which is shown in red in Table 5-5. However, the Sd of the angular accelerations after wavelet de-trending and de-noising was reduced to the order of 10^{-5} and for the differential mode that was reduced to the order of 10^{-8} . So, the final accuracy of the true gradient in this research is 0.06 Eötvös which is shown in blue in Table 5-5. This final accuracy

for the system output (less than 1 Eötvös) meets the industry needs for exploration of the typical ore bodies with wavelength of 50 to 100 *m*.

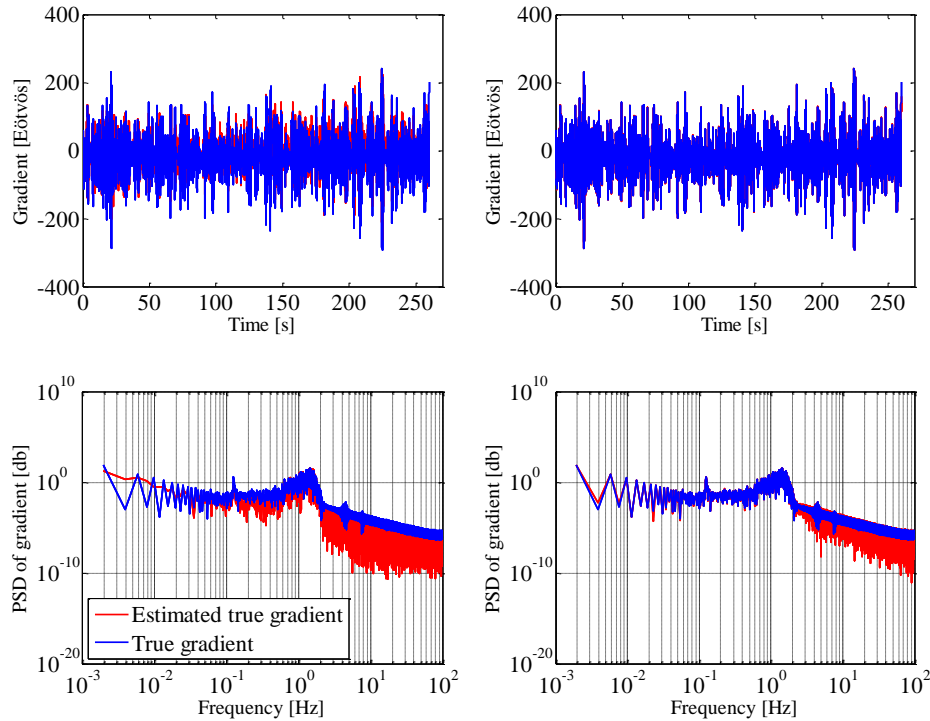


Figure 5-16: True gradient in comparison to estimated true gradient when the Sd of the observations and the Sd of the filtered observations are used to calculate the accuracy of the system output. Left plots: the accuracy of the system output is 10.47 Eötvös. The right plots: the accuracy of the system output is 0.06 Eötvös

Figure 5-16 shows the true gradient in comparison to the estimated true gradient when the Sd of the observations and the Sd of the filtered observations were used to calculate the accuracy of the system output. The left plots (both in time and frequency domains) show the result when the accuracy of the system output is 10.47 Eötvös. Whereas, the right plots show the result when the accuracy of the system output is 0.06 Eötvös (the final accuracy at this research work).

5.3 Summary

The effect of angular velocities squared derived from raw data is -1590 Eötvös while the same effect derived from filtered data is -20 Eötvös. The raw gradient before and after removing the angular velocities squared, the -20 Eötvös effect, were quite similar. The reason is that there are still a large numbers of systematic effects that influenced the gradiometer channel. The performance of the angular gradiometer was evaluated by error propagation in a single-input-single-output system. For this purpose, the true gradient was simulated by simulating the three terms, namely the differential mode and angular accelerations in the x and y directions. The true values, the noise type, and the noise amplitudes were required to do the simulation. The true values of these parameters came from the result of the wavelet de-trending and de-noising of the real dynamic observations. The random noises added to the true values included white, pink, and red noises. The noise amplitude came from the Sds of the static data for each of these three terms. The accuracy of the filtered simulated true gradient with equal weight noise assumption indicated the smallest RMS value (0.002 Eötvös) when both the differential mode and angular accelerations have equal noise Sd in the order of $3e-09 \text{ rad/s}^2$. The biggest RMS value (19.51 Eötvös) occurred when the parameters have the noise Sd in range of the $3e-03 \text{ rad/s}^2$. The output of the gradiometer showed more sensitivity to the differential mode errors than the errors in the angular accelerations. The simulation results showed that achievable accuracy of the system output in this research work is less than 1 Eötvös which meets the industry needs for exploration of typical ore bodies.

Chapter 6: Conclusions and recommendations

Airborne gravity gradiometry offers a great potential in discovering meaningful geological features. By combining airborne gradiometry data with other exploration methods the risks and ambiguities regarding exploration decisions can be decreased. The gradiometer instrument that was studied in this thesis is a superconductive angular gradiometer, with target resolution of the 1 Eötvös at 1 sample per second. The claimed target resolution, as discussed in Matthews (2002) for some regions such as Mt Tom Price, Olympic dam, Elura, and Broken Hill, is sufficient for discovering many mineral deposits (e.g., zinc, gold, copper, and silver). Unfortunately, the presence of a number of limiting factors can reduce the final performance of the gradiometer in a mobile platform. Error contributions in the gradiometer output are related to angular and translational sensitivities, angular velocities squared, temperature sensitivity, fundamental or intrinsic gradiometer error, axis misalignment of the two test masses, and output non-linearity. In addition to improving the sensor noise filtering, reducing the effects of angular velocities squared was a main objective for this research. Investigating about alternative post processing approaches to reduce the errors in the gradiometer output and of its auxiliary sensors (superconductive angular accelerometer) was also a major concern in this work.

6.1 Conclusions

The major objectives of this thesis were outlined in Section 1.3. The main findings and results related to the thesis objectives are outlined below:

The wavelet de-noising technique and Wiener low pass filtering were implemented to remove high frequency errors in the output of the superconductive angular accelerometer x-axis. The wavelet de-trending technique was applied to tackle the low frequency errors of this sensor, as well. The proposed methodologies were applied on the static data, which determines the noise floor for this research study. Obtained results were compared with the results of empirical methods such as

Butterworth low pass filtering and linear regression. This analysis has demonstrated the following points:

- 1- The kind of wavelet base function and the kind of threshold estimator used play a secondary role in the wavelet de-noising and de-trending procedures. However, the number of vanishing moments in each wavelet family had a more substantial effect in reducing the noise RMS value.
- 2- The minimum RMS value has been achieved when the non-white noise was assumed to contaminate the angular gradiometer and angular accelerometer outputs.
- 3- The best wavelet de-noising results were obtained when the reconstructions were done with original approximation and modified detail coefficients at the 7th LOD.
- 4- The RMS value achieved by the wavelet de-noising of the static x angular acceleration showed 44% improvement in comparison to the Butterworth low pass filtering. The RMS value of the result after the Butterworth low pass filtering and the wavelet de-noising showed 98.24% and 99.02% improvement in reducing the noise level in comparison to the original signal, respectively.
- 5- The result of the Wiener low pass filtering depends on how the estimated true signal is selected. For instance, if the estimated true signal is the output of the wavelet de-noising, the filtered signal with the Wiener method showed a 4% improvement in reducing the noise level in comparison to the de-noised signal, which is 99.08% improvement in comparison to the original signal.
- 6- The wavelet de-trending and de-noising procedure yielded a 66% improvement in reducing the noise level in comparison to the performance of the linear multiple regression and the Butterworth low pass filtering results. Wavelet de-trending and de-noising results indicate a 99.44% improvement in reducing the noise level in comparison to the original signal while the same improvement for the empirical approach is 98.33%.
- 7- The wavelet de-trending and the Wiener low pass filtering results showed a 16% improvement in comparison to the wavelet de-trending and de-noising results (99.52% improvement in comparison to the original signal). This was because the estimated true signal into the Wiener filtering was the output of the wavelet de-trending and de-noising procedure.

8- The signal processing method proposed in this research was efficient not only in reducing the noise RMS value, but also in reducing the cost and complexity while solving the problem. This is because, contrary to the empirical method used by Gedex, it does not rely on the output of auxiliary sensors, such as temperature and independently measured accelerations.

A bandpass digital filtering was also designed and applied to the x angular acceleration (see Appendix B). The results indicate the following points:

- 1- Designing an optimum bandpass digital filter is not an easy task; however, its implementation is much simpler than wavelet de-trending and de-noising technique.
- 2- Even though the performance of the best bandpass filter (by least-squares method) is marginally (i.e., 0.05%) worse than that of the best wavelet, it is worth mentioning that this is only tested against the static data and that the noise structure may well change under dynamic conditions. In such a scenario the stopband may contain more noise than in the static case, but with bandpass filtering this would have no residual effect (i.e., all noise in stopband is suppressed).

The effects of angular velocities squared derived from the filtered data was -20 Eötvös. The raw gradient before and after removing this effect were similar. The reason is that there are a large number of systematic effects that influenced the gradiometer channel. For removing the rest of the systematic effects the wavelet de-trending and de-noising of the gradient was applied.

Due to the lack of available control data, the quality assessment of the gradiometer output was done through a simulation procedure. More than 35 different simulated true gradients were analyzed by error propagation in single-input-single-output system. The results support the following points:

- 1- The smallest RMS value (0.002 Eötvös) occurs when both the differential mode and angular accelerations had equal noise S_d in the order of $3e-09 \text{ rad/s}^2$. The biggest RMS

value (19.51 Eötvös) was obtained when the parameters had the noise S_d in range of $3e-03 \text{ rad/s}^2$.

- 2- The gradiometer output was more sensitive to the differential mode errors than the errors in the angular accelerations.
- 3- The S_d s of the static x angular acceleration, y angular acceleration, and differential mode after the wavelet de-noising and de-trending are $3.08e-05 \text{ rad/s}^2$, $3.55e-05 \text{ rad/s}^2$, and $3.21e-08 \text{ rad/s}^2$, respectively. So the final accuracy of the true gradient in this research work is 0.06 Eötvös.

The simulation results showed that achievable accuracy of the system output is better than 1 Eötvös which can meet the industry needs for exploration of typical ore bodies that require the gradients to be known with an accuracy of 1 Eötvös.

6.2 Recommendations

Further investigations and future research work are recommended below:

- 1- Combining bandpass filtering together with in-band filtering (e.g., wavelet) is highly recommended. This could be either done in two steps (i.e., bandpass first then wavelet) or doing it all within wavelet (e.g., putting wavelet coefficients to zero apart from certain LODs - using the external knowledge that there is no signal in such LOD).
- 2- The error analysis in this research has been assumed that the calibration in terms of thermal, electrical, and mechanical have been successfully done for the sensors that produced the data sets used. That is why the post processing approaches were weighted highly in this study. Although we did not have access to the contribution of each of these factors to the gradiometer output, further investigations should be done if Gedex is willing to release such data.
- 3- One of the major concerns regarding this study is the possibility that after applying all these filtering techniques we may have altered the true signal in some of the data sets. In the future, the known noise characteristic of the data and information regarding reference

(control) data must be made available. In this way, we are not only able to improve both the system's performance but also we are able to give a definitive answer regarding the actual gradiometer accuracy that it can achieve.

- 4- A proper system modeling relied on the equations that given the operation of the system is required, i.e., that relate all sensor measurements to the gradiometer output.
- 5- State space error modeling such as Kalman filtering is recommended for non-white noise structure of the gradiometer data.
- 6- The thesis reported a current performance regarding a superconductive angular gradiometer sitting in a laboratory situation. Undoubtedly, further investigations are required to reduce the noise level in a real platform during the flight conditions. For this, the system needs to be flown over an area with well-known gravity gradients.
- 7- In a future version of the hardware, Gedex should include firmware for controlling the system and for easy access to all sensor recording.
- 8- The dynamic case simulation should be done again by creating a much more dynamic data set that would include additional biases, signal drops, and disturbances due to flight dynamics and vibrations.
- 9- Variance Component Estimation is recommended to calculate the associated noise variance in the simulation procedure.
- 10- Having the output of three-axis gradiometer is recommended. It is not only useful in efficient reduction of the noise level but also in providing more constraints to recover the geological signals.
- 11- Having cross component of the gradient plus the gradient difference output (which was the only component available for this research) is recommended. It can, also, provide more constraints to recover geological signals.

References

- Adamczak, S, W Makiela, and K Stepien. 2010. "Investigating advantages and disadvantages of the analysis of a geometrical surface structure with the use of Fourier and Wavelet transform." *Metrology and measurement systems* 233-244.
- Andreas, E.L, and G Trevino. 1996. "Using wavelets to detect trends." *Journal of Atmospheric and Oceanic technology* 554-564.
- Anstie, J, T Aravanis, P Johnston, A Mann, M Longman, A Sergeant, R Smith, et al. 2010. "Preparation for flight testing the VK1 gravity gradiometer." Abstracts from the ASEG-PESA, Airborne Gravity 2010 Workshop. Canberra: Geoscience Australia. 5-12.
- Barnes, G.J, and J.M Lumley. 2010. "Noise analysis and reduction in full tensor gravity gradiometry data." Abstracts from the ASEG-PESA, Airborne Gravity 2004 Workshop. Canberra: Geoscience Australia. 21-27.
- Bendat, J.S , and A.G Piersol. 1985. *Random data analysis and measurement procedures, Second Edition (Revised and Expanded)*. Printed in the United States of America: John Wiley & Sons, Inc.
- Biegert, E.K, M Talwani, and D.J Smit. 2001. "IG-2: Gravity gradients for de-risking prestack depth migration." Shell U. K. Exploration and Production. Amsterdam, The Netherlands: EAGE 63rd Conference & Technical Exhibition.
- Boggs, D.B, and M.H Dransfield. 2004. "Analysis of errors in gravity derived from FALCON airborne gravity gradiometer." Abstracts from the ASEG-PESA, Airborne Gravity 2004 Workshop. Canberra: Geoscience Australia. 135-141.

- Brown, R.G. 1983. Introduction to random signal analysis and kalman filtering. Printed in the United States of America : John Wiley & Sons, Inc.
- Bruton, A.M. 2000. Improving the accuracy and resolution of SINS/DGPS airborne gravimetry. PhD thesis, Calgary, Alberta: Department of Geomatics Engineering, The University of Calgary.
- Carroll, K.A, D Hatch, and B Main. 2010a. "Performance of Gedex high-definition airborne gravity gradiometer." Abstracts from the ASEG-PESA, Airborne Gravity 2010 Workshop. Canberra: Geoscience Australia. 37-43.
- Carroll., A.K, Moody V, and H.J Piak. 2010b. Torque on a body due to the local gravity gradient tensor. Confidential report, Mississauga, Ontario: Gedex Inc.
- Carter, B. 2008. OP AMP noise theory and applications. Dallas: TX: Texas Instruments, 10.1-10.24.
- Chan, H.A, and H.J Piak. 1987. "Superconducting gravity gradiometer for sensitive gravity measurements. I. Theory." The American Physical Society 35: 3551-3571.
- Craymer, M.R. 1998. The least squares spectrum, its inverse transform and autocorrelation function: theory and some applications in Geodesy. PhD thesis , Toronto : Graduate Department of Civil Engineering, The University of Toronto.
- Donoho, D.L, and I.M Johnstone. 1995. "Adapting to unknown smoothness via wavelet shrinkage." Journal of the American Statistical Association 90: 1200-1224.
- Dransfield, M.H, and J.B Lee. 2004. "The FALCON airborne gravity gradiometer survey systems." Abstracts from the ASEG-PESA, Airborne Gravity 2004 Workshop. Canberra: Geoscience Australia. 15-19.

- Dransfield., M. 2007. "Airborne gravity gradiometry in search for mineral deposits." *Advances in Airborne Geophysics* 341-354.
- El-Ghazouly , A.A, M.M Elhabiby, and N El-Sheimy. 2009. "The use of wavelets in GPS error analysis with emphasis to singularity detection and multipath removal." *American Geophysical Union Joint Assembly*. Toronto.
- El-Ghazouly, A.A. 2013. Multi-Resolution spectral techniques for static DGPS error analysis and mitigation. PhD thesis, Calgary, Alberta: Department of Geomatics Engineering, The University of Calgary.
- Elhabiby, M.M. 2007. Wavelet representation of geodetic operators. PhD thesis, Calgary, Alberta: Department of Geomatics Engineering, The University of Calgary.
- Farge, M. 1992. "Wavelet transforms and their applications to turbulence." *Annu. Rev. Fluid Mech* 395-457.
- Fodor, I.K, and C Kamath. 2001. "Denoising through wavelet shrinkage: an empirical study." *Journal of Electronic Imaging*.
- Gao, R.X, and R Yan. 2011. *Wavelets: theory and applications for manufacturing*. Springer.
- Ghilani, C.D, and P.R Wolf. 2006. *Adjustment computations: spatial data analysis*, Forth Edition. Hoboken, New Jersey: John Wiley & Sons, INC.
- Goldstein, H. 1965. *Classical mechanics*. Printed in the United States of America: Addison-Wesley Publishing Company, INC.

- Goossens, B, A Pizurica, and W Philips. 2009. "Removal of correlated noise by modelling the signal of interest in the wavelet domain." *IEEE transactions on image processing* 1153-1165.
- Guio, P. 2011. Levi-Civita symbol and cross product vector/tensor. December 03.
- Hein, G.W. 1995. "Progress in airborne gravimetry: solved, open and critical problems." IAGG symposium G4, IUGG XXI General Assembly. Boulder, Colorado: Department of Geomatics Engineering at The University of Calgary. 3-11.
- Hofmann-Wellenhof, B, and H Moritz. 2006. *Physical Geodesy*, Second corrected edition. Austria: SpringerWienNewYork.
- Jekeli, C. 2006. "Airborne gradiometry error analysis." *Springer* 257-275.
- Kann, F.V. 2004. "Requirements and general principles of airborne gravity gradiometers for mineral exploration." Abstracts from the ASEG-PESA, Airborne Gravity 2004 Workshop. Canberra: Geoscience Australia. 1-4.
- Karam, L.J, J.H McClellan, I.W Selesnick, and C.S Burrus. 1999. *Digital filtering*. Boca Raton: CRC Press LLC.
- Li, Y. 2000. *Airborne gravimetry for geoid determination*. PhD thesis, Calgary, Alberta: Department of Geomatics Engineering, The University of Calgary.

- Lumley , J.M, J.P White, G Barnes, D Huang, and H.J Paik. 2004. "A superconducting gravity gradiometer tool for exploration." Abstracts from the ASEG-PESA, Airborne Gravity 2004 Workshop. Canberra: Gepsience Australia . 21-39.
- Lyrio, J, L Tenorio, and Y Li. 2004. "Efficient automatic denoising of gravity gradiometry data." Society of Exploration Geophysicists 772-782.
- Matthews, R. 2002. Mobile gravity gradiometry. PhD thesis, Physics, Department of Physics, The University of Western Australia.
- McTavish, Don. 2014. Information for U of Calgary. Confidential Report , Mississauga, Ontario: Gedex Inc.
- Misiti, M, Y Misiti, G Oppenheim, and J.M Poggi. 2014. Wavelet toolbox user's guide. The MathWorks, Inc.
- Moody, M. V, and H. J Paik. 2004. "A superconductive gravity gradiometer for inertial navigation." Position, Location, and Navigation Symposium 775-781.
- Moody, M. V, Q Kong, H. J Paik , and J. W Parke. 1988. "Three-axis superconducting gravity gradiometer - progress report ." 16th gravity gradiometry conference . Colorado: United States Air Force Academy.
- Moody, M.V. 2011. "A superconducting gravity gradiometer for measurements from a moving vehicle." Review of scientific instruments, American Institute of Physics.

- Moody, M.V, and H.J Paik. 2004. "A superconducting gravity gradiometer for inertial navigation." Position location and navigation Symposium 775-781.
- Moody, M.V, and H.J Paik. 2007. Cross-component superconducting gravity gradiometer with improved linearity and sensitivity for gravity gradient sensing. United States of America Patent 60/663. December 11.
- Moody, M.V, H.J Paik, and E.R Canavan. 2003. "Principle and performance of a superconducting angular accelerometer." Review of Scientific Instruments, American Institute of Physics 1310-1318.
- Moody, M.V, H.J Paik, and E.R Canavan. 2002. "Three-axis superconducting gravity gradiometer for sensitive gravity experiments." Review of Scientific Instruments, American Institute of Physics 3957-3974.
- Moody, Martin Vol, and Ho Jung Paik. 2007. United States Patent US00 7, 305,879 B2.
- Murphy, C.A. 2004. "The Air-FTG airborne gravity gradiometer system." Abstracts from the ASEG-PESA, Airborne Gravity 2004 Workshop. Canberra: Geoscience Australia. 7-14.
- Nassar, S. 2003. Improving the inertial navigation system (INS) error model for INS and INS/DGPS applications. PhD thesis , Calgary, Alberta: Department of Geomatics Engineering, The University of Calgary.
- Oppenheim, A.V, and R.W Schafer. 1989. Discrete-Time signal processing. Prentice-Hall, Inc.

- Parks, T. W, and J. H McClellan. 1972. "Chebyshev approximation for non-recursive digital filters with linear phase." IEEE Trans Au-20: 195-199.
- Piak, H.J, E.R Canavan, and M.V Moody. 1997. "Airborne/shipborne SGG survey system." Banff, Canada. 565-570.
- Pilgram, B, and D.T Kaplan. 1998. "A comparison of estimators for 1/f noise." Physica (Department of mathematics and computer science, Macalester College) 108-122.
- Sagar, M.J, S.N Sampat, and S.B Parmar. 2009. "Outlier removal using multilevel wavelet transform technique." Journal of information, knowledge and research in Electronics and communication Engineering 671-674.
- Sasgen, I, Z Martinec, and K Fleming. 2006. "Wiener optimal filtering of GRACE data." Stud. Geophys. Geod 499-508.
- Schwarz, K.P, and A.A Vassiliou. 1986. "Requirements for the use of airborne gravity gradiometry in geophysical exploration." Proceedings of the fourteenth annual gravity gradiometry conference. Colorado: United States Air Force Academy.
- Schwarz, K.P, and Z Li. 1996. An introduction to airborne gravimetry and its boundary value problems. Lecture notes, Como Italy: IAG International Summer School.
- Selesnick, I.V. 2013. EL 713: Digital signal processing. Lecture notes, New York: NYU Polytechnic School of Engineering.

- Sideris, M.G . 1996. "On the use of heterogeneous noisy data in spectral gravity field modeling methods." *Journal of Geodesy* 470-479.
- Skaloud, J. 1999. Optimizing georeferencing of airborne survey systems by INS/DGPS. PhD thesis , Calgary, Alberta: Department of Geomatics Engineering, The University of Calgary.
- Smith, S.W. 1999. *The scientist and engineer's guide to digital signal processing*, Second Edition. San Diego, California: California Technical Publishing.
- Teskey, W. 2011. Assessment and attenuation of movement disorder motion using inertial sensors. PhD thesis, Calgary, Alberta: Department of Geomatics Engineering, The University of Calgary.
- Torge, W. 1989. *Gravimetry*. Berlin: Walter de Gruyter.
- Torrence, C, and G.P Compo. 1998. "A practical guide to wavelet analysis." *Bulletin of American Meteorological Society* 61-78.
- Tryggvason, B, B Main, and B French. 2004. "A high resolution airborne gravimeter and airborne gravity gradiometer." Abstracts from the ASEG-PESA, Airborne Gravity 2004 Workshop. Canberra: Geoscience Australia. 41-44.
- Vanicek, P, and E Krakiwsky. 1986. *Geodesy the concepts*. New York: Elsevier Science Publishing Company, INC.
- Wu, L. 1996. Spectral methods for post processing of airborne vector gravity data. Master thesis, Calgary, Alberta: Department of Geomatics Engineering, The University of Calgary.

Appendix A: An introduction to wavelet analysis and Wiener low pass filtering

Wavelet transforms have shown great potential in data analysis especially in detecting trends (the lowest frequency part in a signal), singularities and discontinuities, in compressing and de-noising of the signal, and in analyzing non-continuous and irregular functions (El-Ghazouly 2013, El-Ghazouly et al., 2009, Goossens et al., 2009, Sagar et al., 2009, Elhabiby 2007, Nassar 2003, Andreas and Trevino 1996.). It also has localizations properties that make it a powerful tool to analyze non-stationary signals such as the signals available for this research. In contrast to traditional Fourier methods, wavelets can provide a wide range of options to select the best base functions. Multiresolution analysis, as a great tool in wavelet spectral analysis makes this method computationally efficient. Additionally, the de-noising technique can help keep the desired signal and remove the unwanted content of the signal better than low pass filtering that automatically removes the whole high frequency content of the signal. Wavelets are also capable of mitigating both the white and the non-white noise parts of the errors contaminating in any observations. Besides the advantages of wavelets, there are some disadvantages. For instance, the method is complicated in terms of selecting a suitable base function, level of decomposition, threshold types and many other optimizing parameters.

Wiener low pass filtering as one of the popular frequency domain filters that can also be applied to the data sets available for this research to cope with high frequency errors in the data. The filter is designed in a way that the average squared error is minimized. One of the major advantages of this filter is that it is simple and easy to implement in the frequency domain. On the other hand, the Wiener filter works only under an assumption of stationarity with white noise. Furthermore, the estimated power spectral densities of the true and noise signals are necessary to calculate the filter's frequency response, which might be difficult to obtain.

Both the wavelet and the Wiener low pass filtering methods will be briefly introduced in this appendix. These methods will be applied to the x angular acceleration data, which can then be generalized to the y angular acceleration and differential mode observations.

A.1 Wavelet spectral analysis

Going through the pure mathematical background of the wavelets is not a primary goal of this thesis; interested readers are referred to many literature sources, such as Farge (1992) and Torrence and Compo (1998), and Gao and Yan (2011). Here, wavelets and their properties will be introduced briefly. The Continuous Wavelet Transform (CWT) and its inverse will then be shown with a simple formula. Afterwards, the concept of Discrete Wavelet Transform (DWT) along with Multiresolution Analysis (MRA) will be discussed.

A.1.1 Wavelets properties

By definition, the average value of the wavelet must be zero in the time domain. Additionally, wavelets are oscillatory and their energy concentrated at a short time interval, which makes them a great tool to study non-continuous and irregular functions, and to analyze non-stationary signals. Mean and variance for a non-stationary signal change over time. Figure A-1 shows how the mean and variance of the x angular acceleration are changing over time. The mean and variance are calculated based on a moving average technique with a group of 500 samples at each part. Therefore, it is apparent that wavelets would be a good option to analyze this signal.

The Fourier transform is only restricted to sine and cosine functions while the wavelet spectral analysis can provide a large number of base functions to analyze the signal. This is one of the advantages of wavelet analysis. A set of mother wavelets is shown in Figure A-2. The wavelet base functions are classified by some properties such as orthogonality, number of vanishing moments, symmetry, and compact support. The orthogonality property helps quick decomposition and reconstruction of analyzed signals.

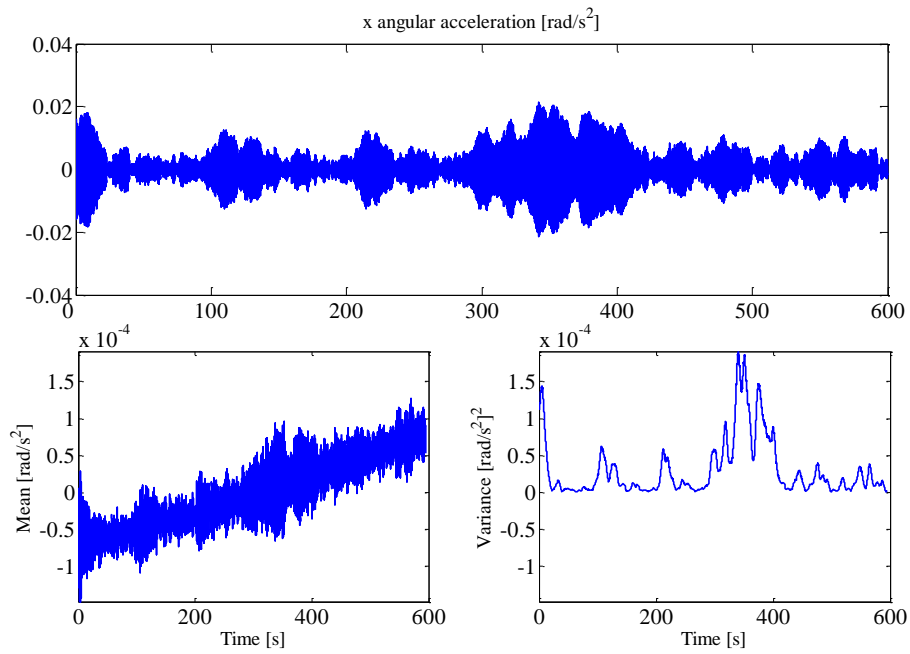


Figure A-1: Mean and variance of x angular acceleration (static data set)

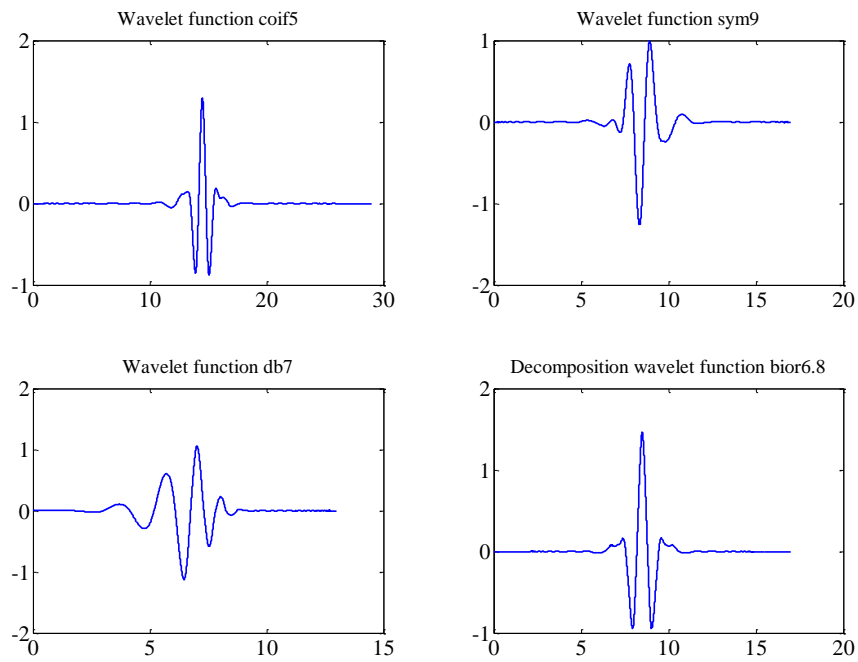


Figure A-2: Different kind of mother wavelets

The number of vanishing moments determines if a chosen wavelet is able to best approximate the analyzed signal with polynomials of special degree. The symmetry property is a desirable property in filtering problems. Finally, the compact support operators are defined as functions with non-zero value only in a limited portion of their domains. This property ensures detecting localized features in a signal (Gao and Yan 2011, Lyrio et al., 2004). A number of wavelet families with their different properties are shown in Table A-1.

Table A-1: Wavelet families and their properties (Misiti et al., 2014)

Property	Morlet	Gaussian	Meyer	Haar	Daubechy	Symlet	Coiflet	Biorthogonal
Orthogonality			✓	✓	✓	✓	✓	✓
Arbitrary NOVM					✓	✓	✓	✓
Symmetry	✓	✓	✓	✓				✓
Compactly support				✓	✓	✓	✓	
CWT	✓	✓	✓	✓	✓	✓	✓	✓
DWT				✓	✓	✓	✓	✓

NOVM stands as Number of Vanishing Moments in Table A-1.

Wavelets are good for studying signals of limited duration or length. However, they are not suitable to analyze periodic or infinite signals (Adamczak et al., 2010). In either case, wavelet base functions require some modifications to fit to the requirements of analyzing signals. Wavelets are also not helpful in detection image edges (Gao and Yan 2011).

A.1.2 Continuous Wavelet Transform (CWT)

A wavelet transform, like any other transform, is defined as an inner product between a signal x and a known base function ψ . The CWT is expressed as (Gao and Yan 2011):

$$\langle x(t), \psi(t) \rangle = wt(s, \tau) = \frac{1}{\sqrt{s}} \int_{-\infty}^{\infty} x(t) \psi^* \left(\frac{t-\tau}{s} \right) dt \quad (\text{A-1})$$

ψ^* is the complex conjugate of the scaled by s and translated by τ mother wavelet

The result is a series of coefficients, which describes the similarity between the signal and the known base function. The wavelet transform can then decompose the signal into a weighted sum

of scaled and translated versions of the wavelet base function (mother wavelet). The signal under analysis can be reconstructed with the help of the inverse wavelet transform given below:

$$x(t) = \frac{1}{C_\psi} \int_0^\infty \frac{ds}{s^2} \int_{-\infty}^\infty w t_x(s, \tau) \frac{1}{\sqrt{s}} \psi\left(\frac{t - \tau}{s}\right) d\tau \quad (\text{A-2})$$

where $C_\psi = \int_0^\infty \frac{|\Psi(f)|^2}{f} df < \infty$ is the so called admission condition of the wavelet $\psi(t)$.

The scaling function is responsible for extracting information from the signal under analysis at different time or frequency resolutions while the translating function helps the localization of any feature in both the space and frequency domains. Scaling helps squeezing and stretching the wavelet function and makes it appropriate for what information one wants to extract from the signal. The high frequency information (features that change rapidly) is detectable at smaller number of scales while the low frequency information (features that change slowly) is detectable at larger number of scales.

In practice, coefficients of the CWT are used to represent how a signal will look like in a wavelet domain. Two parameters, the energy of the signal and the scalogram, are common to use for this purpose. The total energy variation of the signal E at each scale is written as (Lyrio et al., 2004):

$$E_j = \sum_k w_{j,k}^2 \quad j = 1, \dots, J \quad (\text{A-3})$$

where $w_{j,k}^2$ is the power of the wavelet coefficient at time k and j is the number of scale. The energy of the x angular acceleration is shown in Figure A-3 (using wavelet Db8 base function from scale 1 to 60). As is clear from this figure, at smaller wavelet scales (high frequency) the energy is distributed smoothly. However, at larger scales (frequency mostly from 8 to 32), there are some sharper peaks with large amplitude. After scale 40 there is no variation in the energy of the signal.

The Scalogram (the percentage of energy) is another tool for showing the wavelet coefficient, which is formulated as (Misiti et al., 2014):

$$sc = \left(\frac{w_{j,k}^2}{\sum_j E_j} \right) * 100 \quad (\text{A-4})$$

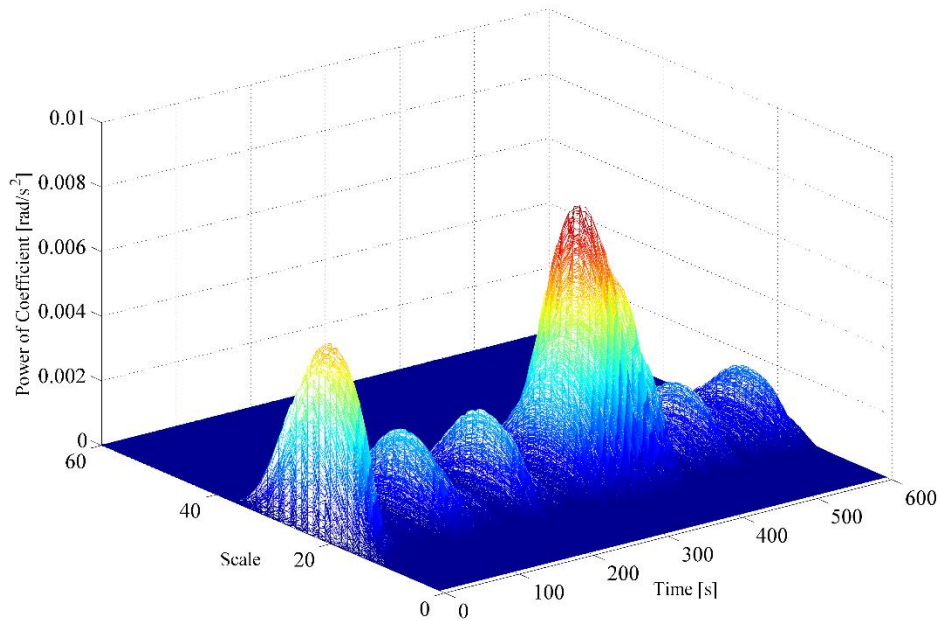


Figure A-3: Energy variation of the x angular acceleration as a function of scale in power of rad/s^2 using Db8 wavelet base function from 1 to 60 scales

This is also very commonly used to represent a signal in a wavelet domain as a function of frequency variation. A pseudo-frequency F_a is given to correspond to the given scale s . This can be formulated as (Teskey 2011):

$$F_a = \frac{F_c}{s\Delta t} \quad (A-5)$$

where F_c is center frequency and Δt is sampling period.

As is clear from Equation (A-5), the pseudo frequency is the scaled version of the center frequency. Center frequency is defined as the frequency of a sinusoidal function that matches to the given wavelet. Figure A-4 displays the contour plot of the scalogram related to the x angular acceleration signal from static data. One can see the corresponding frequency (4.3 Hz to 16.9 Hz frequencies) to each scale (8 to 32 scales).

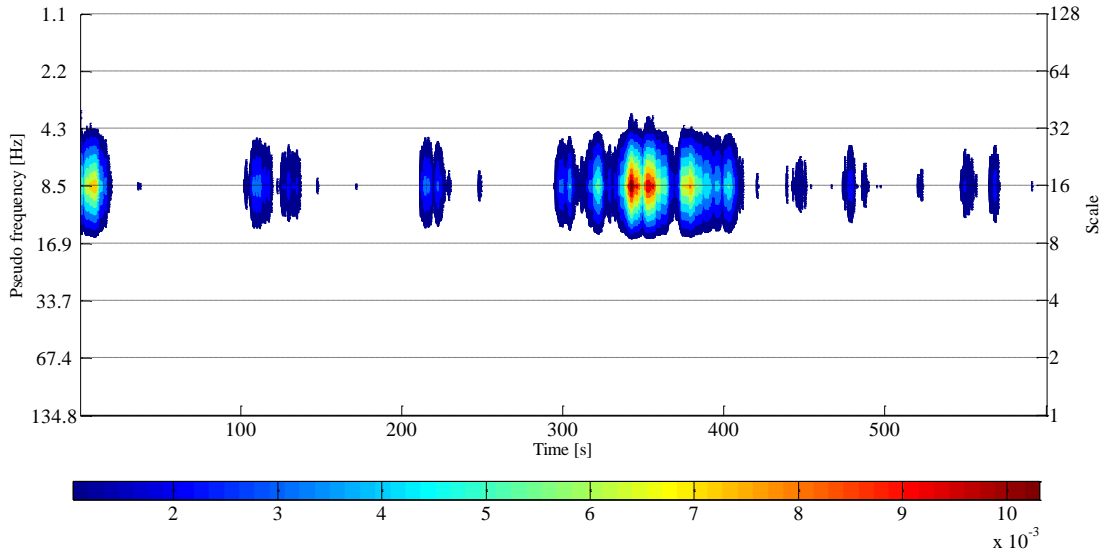


Figure A-4: The contour plot of the scalogram for x angular accelerations (using Coif5 as a wavelet base function)

Increasing the number of scales in CWT can build a more complete picture of the analyzing signal, which can produce redundant information. However, this will increase the amount of memory size and time needed for computation, as well. This is why the Discrete Wavelet Transform (DWT) is implemented in practice instead of the CWT. The DWT is discussed in the next sub-section.

A.1.3 Discrete Wavelet Transform (DWT)

One way to discretize the CWT is to discretize the scale and translation parameters. The most common way to use a logarithmic form of scale is written as (Gao and Yan 2011):

$$\begin{cases} s = s_0^j \\ \tau = k\tau_0 s_0^j \end{cases} \quad s_0 < 1, \tau_0 \neq 0 \quad j, k \in \mathbb{Z} \quad (\text{A-6})$$

where \mathbb{Z} denotes the set of integers. Thus, the translated and scaled version of a mother wavelet can be written as follows:

$$\psi_{j,k}^*(t) = \frac{1}{\sqrt{s_0^j}} \psi^*\left(\frac{t - k\tau_0 s_0^j}{s_0^j}\right) \quad (\text{A-7})$$

It is practical to select $s_0 = 2$ and $\tau_0 = 1$, which is called a dyadic frame. Eventually, the DWT of the signal can be computed by putting Equation (A-7) into Equation (A-1). The integer j will

increase until it satisfies the length of the signal N ($N = 2^j$). This procedure builds orthogonal wavelet bases and leads to multiresolution analysis, which helps fast decomposition and reconstruction of the signal without producing redundant information, and at the same time preserving all desired information contained in the original signal. This is explained in the next section.

A.1.4 Multiresolution analysis (MRA)

Multiresolution analysis was introduced as a mathematical background for constructing orthogonal wavelet base functions that helps simple, fast and efficient decomposition and reconstruction of the signal using a DWT. The algorithm follows a pyramid structure by decomposing the signal to two sets of low and high pass filtering coefficients. By convolving the signal with high pass H and low pass L filtering coefficients along with down sampling by a factor of 2 generates detail D_1 and approximation A_1 coefficients at first Level of Decomposition (LOD), respectively. The approximation part can be further decomposed to provide the next level of detail information D_2 and approximation information A_2 . The process is continued until the maximum level of decomposition satisfies the length of the signal in a logarithmic scale. A two-level decomposition of the signal as a wavelet tree is visualized in Figure A-5. The arrow representation in this figure denotes sub-sampling that keeps only the even numbered component of the data at each stage (Gao and Yan 2011).

MRA of the space $L^2(R)$ (R denotes the integer numbers), theoretically, includes a sequential approximation subspaces $V_{i,j} \in Z$ (Z denotes the integer numbers). So mathematically, the approximation coefficient $A_{j,k}$ at scale j is the inner product of the signal $x(t)$ and a shifted version of the scaling function $\phi_{j,k}$ (belongs to a subspace V , which is) as below (Gao and Yan 2011):

$$A_{j,k} = \langle x(t), \phi_{j,k}(t) \rangle \tag{A-8}$$

$$A_{j,k} = \sum_k A_{j,k} \phi_k(2^{-j}t) = \sum_k A_{j,k} \phi_{j,k}(t) \quad k \in Z$$

Similarly, the detail coefficient $D_{j,k}$ is the inner product of the signal with a function $\psi_{j,k}(t)$, which is an orthogonal complement of the subspace V as:

$$D_{j,k} = \langle x(t), \psi_{j,k}(t) \rangle \quad (\text{A-9})$$

$$D_{j,k} = \sum_k D_{j,k} \psi_k(2^{-j}t) = \sum_k D_{j,k} \psi_{j,k}(t) \quad k \in \mathbb{Z}$$

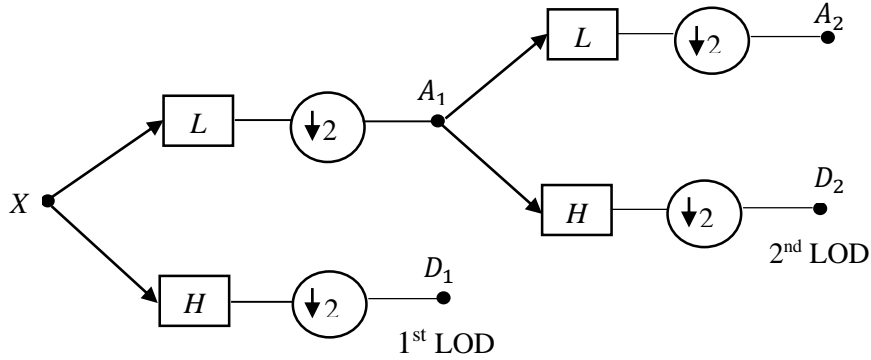


Figure A-5: A two-level decomposition of the signal as a wavelet tree

Thus, the inverse wavelet transform instead of Equation (A-2) is written as:

$$x(t) = \sum_{j=-\infty}^J \sum_{k=-\infty}^{\infty} D_{j,k} \psi_{j,k}(t) + \sum_{k=-\infty}^{\infty} D_{J,k} \phi_{j,k}(t) \quad (\text{A-10})$$

J is a predetermined scale.

As was mentioned in Section A.1.2, each scale corresponds to a pseudo frequency and now each LOD has the same properties. Table A-2 shows different LODs and their corresponding pseudo frequencies computed for static data with a 195.32 Hz sampling frequency.

Table A-2: Pseudo frequencies associated with each decomposition level at 195.32 Hz sampling rate computed with Coif5 wavelet

LOD	Pseudo Frequency (Hz)	LOD	Pseudo Frequency (Hz)
1	67.35	7	1.05
2	33.68	8	0.53
3	16.84	9	0.26
4	8.42	10	0.13
5	4.21	11	0.07
6	2.10	12	0.03

Obviously, the low frequency information is projected into a larger decomposition level whereas the high frequency information is mapped into a smaller decomposition level. This concept is depicted in Figure A-6 in terms of approximation and detail coefficients.

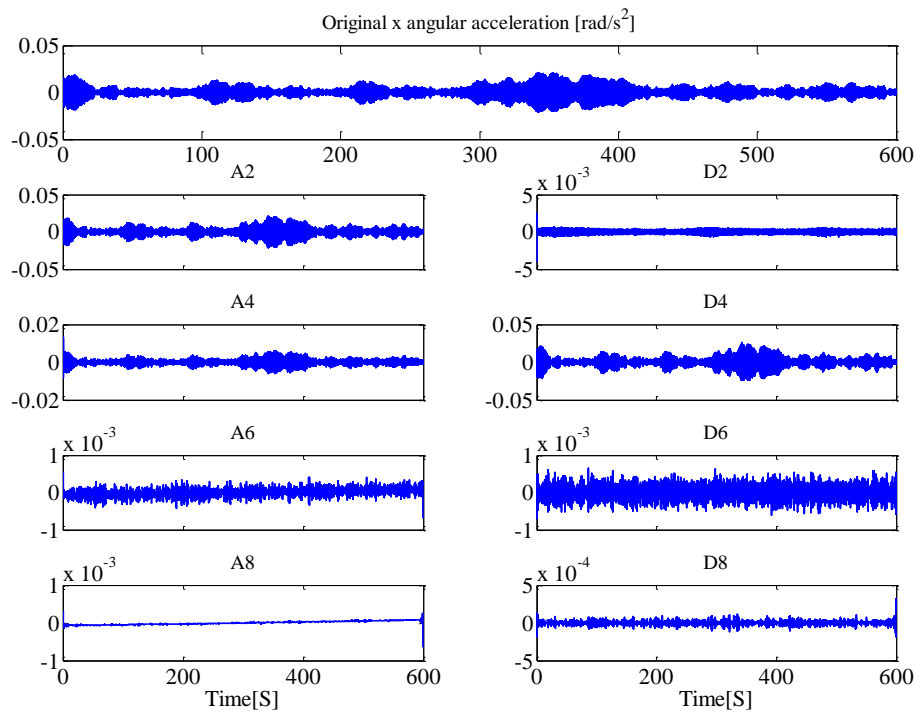


Figure A-6: Reconstructed x angular acceleration with detail and approximation coefficients with Coif5 wavelet from the 1st to the 8th LOD

Now, a handy tool is available for reconstructing the signal with either approximation or detail information at the desired frequency band. Generally, this leads to the idea of de-noising where the wanted term is approximation coefficients, and de-trending where the wanted term is detail coefficients.

A.2 Wavelet de-noising

The idea of wavelet de-noising is based on the fact that the energy of the signal is represented by a small number of wavelet coefficients with large magnitude, typically located at the larger LOD. However, the energy of the noise is represented by a large number of wavelet coefficients with small magnitude, typically located at the smaller LOD (Lyrio et al., 2004). In other words, detail coefficients at a smaller LOD, as can be seen in Figure A-6, correspond to noise distribution in a signal. Approximation coefficients represent long-term trends that is a wanted signal to be maintained in the de-noising procedure. Consequently, the separation of the noise from the signal can be achieved by choosing a proper LOD for signal reconstruction. If a thresholding scheme is added to the de-noising procedure, the performance of the procedure will be improved. That is reconstruction is done with only detail coefficients whose magnitudes are larger than the determined threshold (Gao and Yan 2011). Consequently, any de-noising problem includes the well-known following steps:

- 1- Decomposing the noisy signal into two parts, detail and approximation coefficients using the MRA technique
- 2- Modifying the detail coefficients through the wavelet shrinkage (thresholding) rules
- 3- Reconstructing the signal with original approximation and modified detail coefficients

As can be seen through the above mentioned steps, the first concern in de-noising is decomposition. For the decomposition, it is required to select the wavelet base function and the number of multiresolution levels. In this thesis, wavelet families including Daubechey, Symlet, Coiflet, and Biorthogonal have been tested for de-noising. Table A-1 shows how these wavelets are different in their orthogonality, symmetry, compact support, and number of vanishing moments. For the kind of noise contaminating the angular accelerometer output, the number of multiresolution decomposition levels has been selected as 7, which corresponds to signals with 1 Hz frequencies (see Equation A-5 and Table A-2 for this correspondence).

Finally yet importantly, the performance of any de-noising is related to detail coefficients thresholding. The main purpose of thresholding is to decide about keeping or ignoring the particular coefficient. The following relation shows how the thresholding is applied to the coefficients d (Fodor and Kamath 2001):

$$\hat{d} = \hat{\sigma} \delta_{\lambda}(d) \quad (\text{A-11})$$

Where,

- \hat{d} : Shrunk version of detail coefficient
- λ : Threshold magnitude
- $\delta_{\lambda}()$: Shrinkage function
- $\hat{\sigma}$: Estimated standard deviation for the noise level

Optimum de-noising results depend on the choice of some parameters such as threshold magnitude that is calculated by some threshold estimators, shrinkage functions that determines how the threshold is applied to data (soft or hard thresholding), and noise estimations that makes the threshold value to be scaled. Thus, different de-noising models will differ in the choices for these parameters. A brief explanations about these three parameters is given in the next sub-sections.

A.2.1 Soft or hard thresholding ($\delta_{\lambda}()$)

The shrinkage function $\delta_{\lambda}()$ determines how a particular threshold is applied to wavelet coefficients. There are two common ways for this in literature: the first one is hard thresholding in which the coefficients whose amplitudes are smaller than the threshold are set to zero. Mathematically, this is written as (Misiti et al., 2014):

$$\hat{d} = \begin{cases} d & |d| > \lambda \\ 0 & |d| \leq \lambda \end{cases} \quad (\text{A-12})$$

The second approach is called soft thresholding and the coefficients whose magnitudes are larger than the threshold will shrink to zero. Mathematically, this is expressed as:

$$\hat{d} = \begin{cases} d - \lambda & d > \lambda \\ 0 & |d| \leq \lambda \\ d + \lambda & d < -\lambda \end{cases} \quad (\text{A-13})$$

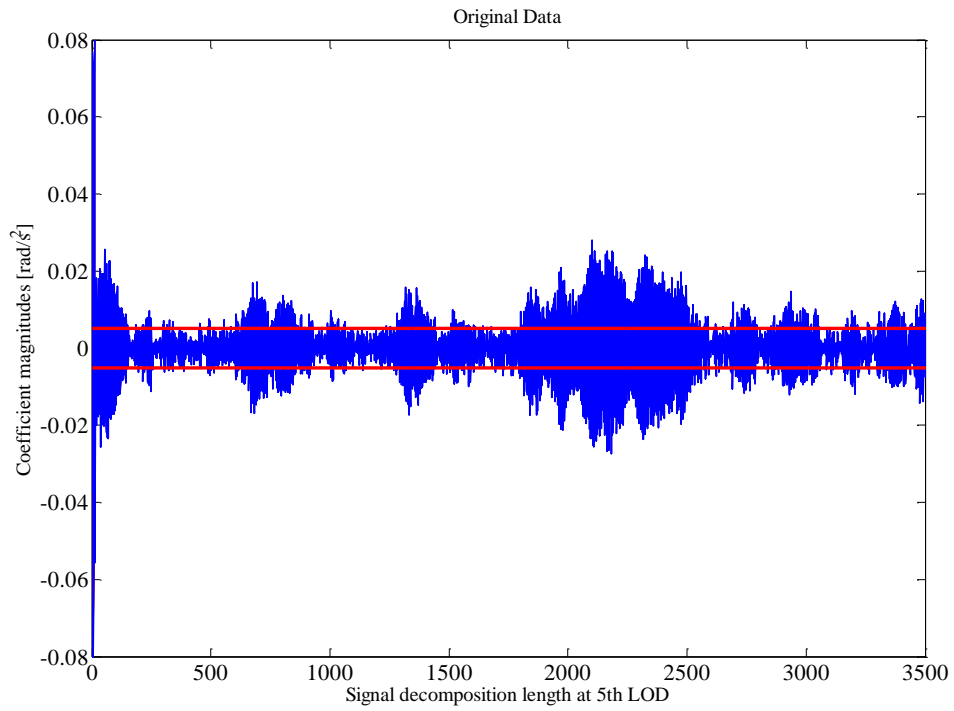


Figure A-7: Detail coefficient at the 5th LOD computed by Coif5 wavelet for the x angular acceleration (threshold magnitude is depicted with red line)

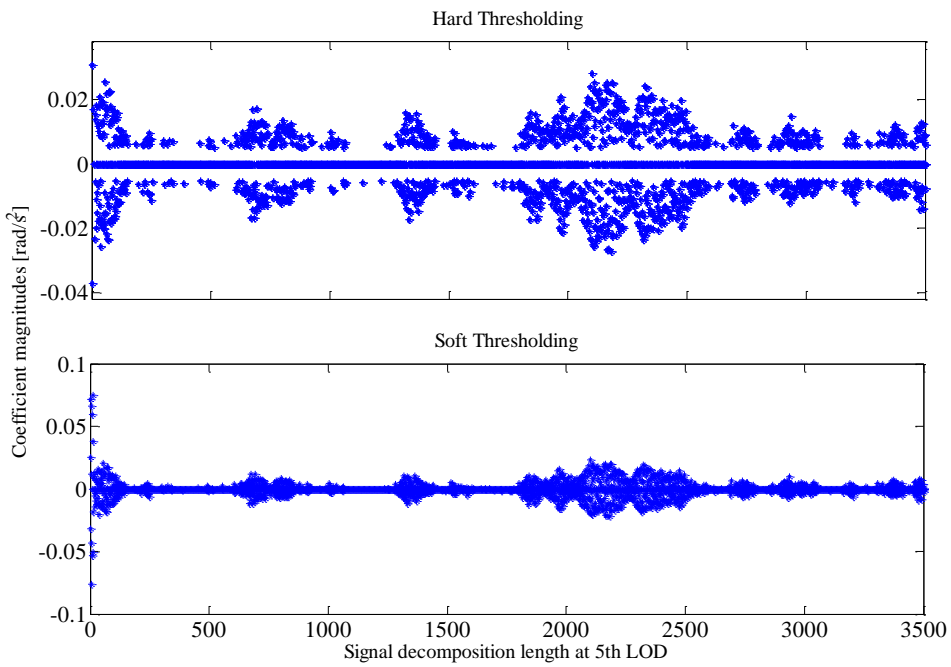


Figure A-8: Detail coefficients at the 5th LOD after applying hard and soft thresholding on the x angular acceleration

It is worth mentioning that soft thresholding is what is commonly used in signal de-noising (El-Ghazouly 2013). For example, by assuming the threshold magnitude equal to 0.0052, both hard and soft thresholding are applied to the detail coefficients at the 5th LOD for the x angular acceleration. Original coefficients and the assumed threshold are depicted in Figure A-7. Original coefficients after applying the hard and soft thresholding are shown in Figure A-8. By comparing the original details in Figure A-7 with shrunk details in Figure A-8, it is obvious how harshly the coefficients less than the threshold magnitude are set to zero for hard thresholding case and how coefficients were shrunk to the threshold magnitude by soft thresholding.

A.2.2 Noise estimation procedure ($\hat{\sigma}$)

Noise level can be estimated by using the following relation that is called as the robust median absolute deviation (El-Ghazouly 2013, Donoho and Johnstone 1995):

$$\hat{\sigma}_j = \frac{\text{median}(|d_j|)}{0.6745} \quad (\text{A-14})$$

d_j is detail coefficient at the j th level of decomposition.

By having the noise level, rescaling the threshold magnitude is done with Equation (A-11). In general, there are three approaches for rescaling the thresholds (Fodor and Kamath 2001):

- 1- **Unit noise variance assumption** ($\hat{\sigma} = 1$): In this approach, the noise level is totally ignored
- 2- **White noise assumption**: The noise level $\hat{\sigma}$ is computed with Equation (A-14) by using only the detail coefficient at first level of decomposition (essentially noise coefficients). This approach is known as the global noise estimation approach.
- 3- **Non-white noise assumption**: The noise level $\hat{\sigma}$ is computed with Equation (A-14) by using coefficients from all decomposition levels. Thus, a level-dependent noise level is estimated in this approach.

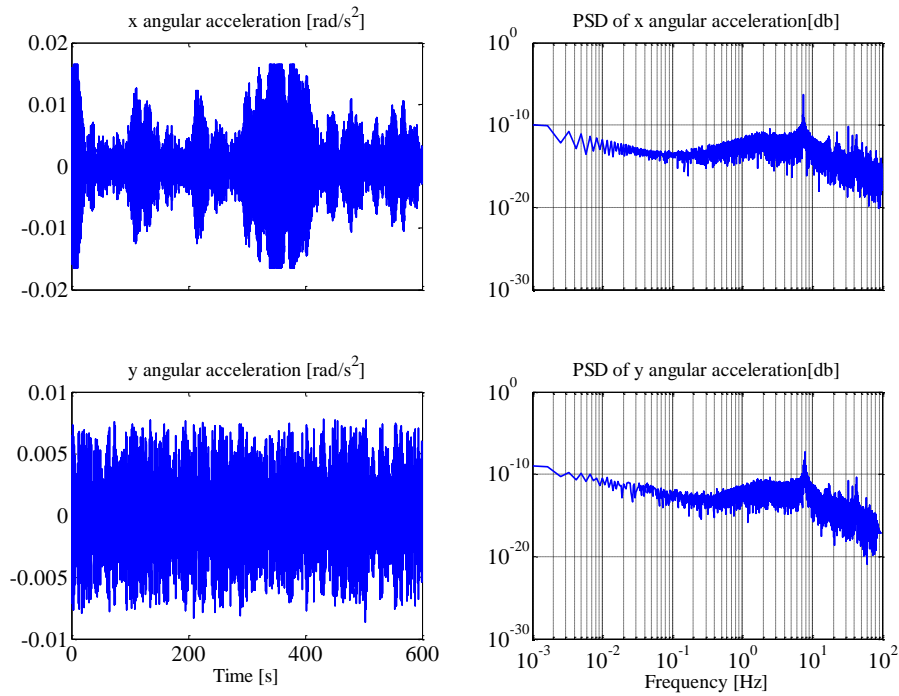


Figure A-9: The x and y angular accelerations in time and frequency domains

In this thesis, thresholds are rescaled using the second and third approaches. As can be seen from the Fourier PSD of the x and y angular accelerations in Figure A-9, the noise encountered in the data is correlated (non-white noise) as the power is increasing by decreasing the frequency (a behavior close to pink and red noise structure) rather than the white noise that has a flat spectrum. More details about the white and non-white noises were explored in Chapter 5.

A.2.3 Threshold selection rules (λ)

There are different threshold rules, which help calculate the threshold magnitudes. In this research, four common threshold estimators are implemented and are listed below (Fodor and Kamath 2001, Misiti et al., 2014, El-Ghazouly 2013)

- 1- **Stein's Unbiased Risk Estimation (SURE) threshold:** For this method, the thresholds are derived by minimizing the estimated risk for a particular threshold value.
- 2- **Median threshold:** A fix form of the threshold value that is calculated by $\lambda = \sigma \sqrt{2 \log N}$ where N is the signal length.
- 3- **Heuristic threshold:** This threshold estimator is a mix of the two previous methods. If the signal to noise ratio is very small, the fixed form of threshold is calculated. Otherwise, the SURE threshold method will be used.
- 4- **Minimum maximum (Minimax) threshold:** As the name implies, the threshold is calculated based on the minimum of the maximum mean square error performance against an ideal procedure.

Mathematical expressions for these threshold estimators can be found in Fodor and Kamath (2001). Figure A-10 shows reconstructed signal with detail coefficients at the 5th LOD.

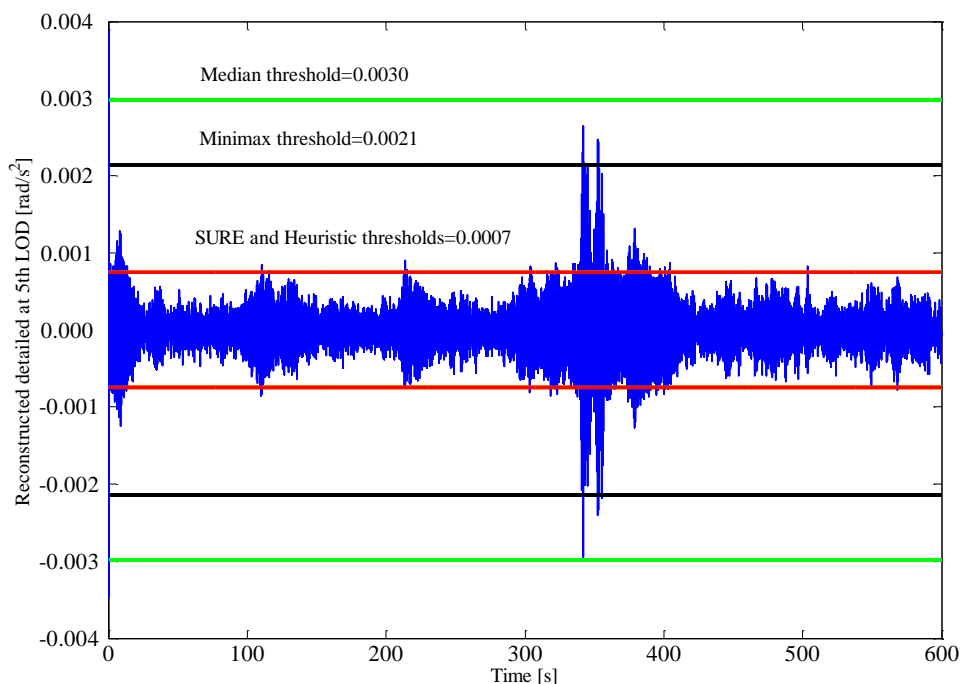


Figure A-10: Thresholds magnitudes computed by four different threshold estimators: Median (green line), Minimax (black line) and both SURE and Heuristic (red line)

All above threshold estimators were used to compute the threshold magnitudes. Threshold magnitudes were rescaled by a non-white noise assumption. Solid green, black and red lines show the Median, Minimax, and both SURE and Heuristic thresholds in this figure. As can be seen in case of Median threshold, almost all the coefficient magnitudes are less than the threshold magnitude and therefore all of them will be shrunk for the purpose of de-noising. The basic wavelet de-noising includes signal decomposition, detail coefficients thresholding, and signal reconstruction with original approximation and modified detail coefficients at predetermined LOD.

A couple of parameters have to be selected for the wavelet de-noising of angular accelerations. All possible combinations were investigated for this research to find out the wavelet efficiency when applied to the x angular acceleration data in Chapter 4. Then the same procedure is applied to the y angular acceleration data as well as the gradiometer output.

A.3 Wavelet de-trending

The low frequency error in the superconducting angular accelerometers is another important affected in this work that has to be removed. This low frequency noise, as was stated in Chapters 2 and 3, is mainly due to the sensitivity of the accelerometers to translational accelerations of the platform and the temperature fluctuations of the environment during the system operation. Wavelets have been shown to have an ability to model such long term trends (Andreas and Trevino 1996). Using an MRA approach, by increasing the LOD, the unknown trend can be detected. Here in this study, approximation coefficients after the 7th LOD are considered as trend. As an example, Figure A-11 shows different trends at the 8th, 9th, and 10th LODs.

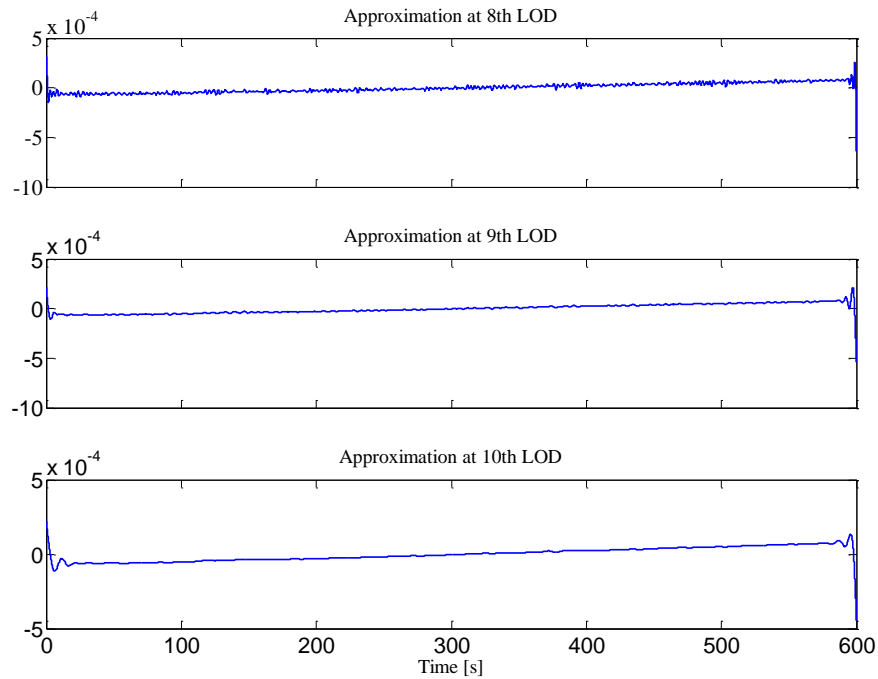


Figure A-11: Different trends computed for the x angular acceleration at the 8th, 9th, and 10th LODs with Coif5 wavelet

A.4 Wiener low pass filtering

In this section a frequency domain filter known as Wiener low pass filtering will be introduced. It will be used to mitigate the high frequency errors of the angular accelerations. The general principle is presented in this appendix and the results were presented in Chapter 4. The purpose of a Wiener filtering, as other filters, is to separate the noise $\epsilon(t)$ from the true signal $x(t)$; see Figure A-12.

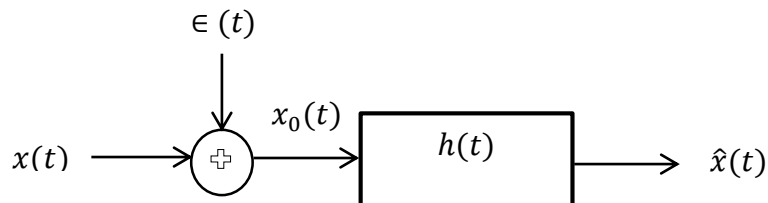


Figure A-12: Principle of Wiener filtering

The Wiener filter has been designed with the following assumptions (Brown 1983)

- 1- The true signal and noise are both random processes with known auto and cross correlation functions.
- 2- There is no non-stationary parameter in the system and the system is linear.
- 3- Optimum frequency response $h(t)$ is computed by using the minimum mean square error criterion between the true signal and the estimated signal $\hat{x}(t)$

The error that is going to be minimized in the least-squares sense is the difference between the desired $x(t)$ and filtered $\hat{x}(t)$ signals as below:

$$MSE = E[e^2(t)] = E[(\hat{x}(t) - x(t))^2] \quad (A-15)$$

For brevity, the mathematical proofs for estimating the filter's frequency response are omitted. Interested readers are referred to Brown (1983) and Wu (1996). Optimum frequency response is (Wu 1996):

$$H(f) = \frac{P_{x_0x}}{P_{x_0x_0}} \quad (A-16)$$

P_{x_0x} is the cross power spectral density between the measurement and the true signal and $P_{x_0x_0}$ is the power spectral density of the measurements. P_{x_0x} and $P_{x_0x_0}$ can be written in the following form (Bendat and Piersol 1985):

$$P_{x_0x} = P_{\epsilon x} + P_{xx} \quad (A-17)$$

$$P_{x_0x_0} = P_{xx} + P_{\epsilon\epsilon} + P_{\epsilon x} + P_{x\epsilon} \quad (A-18)$$

By assuming that there is no correlation between the true signal and input noise (i.e., $P_{\epsilon x} = P_{x\epsilon} = 0$), Equation (A-16) take the following form:

$$H(f) = \frac{P_{xx}}{P_{xx} + P_{\epsilon\epsilon}} \quad (A-19)$$

Or in another form as follows:

$$H(f) = \frac{P_{x_0x_0} - P_{\epsilon\epsilon}}{P_{x_0x_0}} = 1 - \frac{P_{\epsilon\epsilon}}{P_{x_0x_0}} \quad (A-20)$$

Either Equation (A-19) or Equation (A-20) can be used to determine the Wiener frequency response for filtering. The Equation (A-19) is used for computing the filter's frequency response in this research.

The filter kernel can be applied to the noisy data through the following convolution integral in time domain:

$$y(t) = \int_{-\infty}^{\infty} h(\tau)x(t - \tau)d\tau = h * x \quad (\text{A-21})$$

Or by a simple multiplication in frequency domain as below:

$$Y(f) = X(f)H(f) \quad (\text{A-22})$$

Appendix B: Bandpass filtering of x angular acceleration

This appendix will show how to design a bandpass filter, which can be suitable to model both low frequency trends and high frequency errors from the output of the superconductive instruments. The aim of any filtering procedure is to separate the signal (bandwidth of interest) from other interferences (noise). To be consistent with the analysis has been done for the static data in this thesis (Chapter 4), the bandwidth of interest in both the output of the superconductive angular accelerometers and gradiometer is assumed to be 0.53 to 1.01 Hz (corresponds to the 8-7 LODs in wavelet analysis). However, only the result of the static x angular acceleration is presented in this appendix.

B.1 Bandpass filtering

Digital filters are classified in two groups; the first one is called Infinite Impulse Response (IIR), which they use a recursive methodology to create an infinite number of filter coefficients. The second group is called Finite Impulse Response (FIR), which convolution is used to create finite number of the filter coefficients (Smith 1999). The FIR filters are tested here for the error analysis of the superconductive instruments, where they have shown a great potential in the post processing of data series. The IIR filters like Butterworth are more suitable for real time applications (Skaloud 1999).

The convolution is used to define an FIR filter input-output equation is as follows (Skaloud 1999):

$$y_k = \sum_{n=0}^{L-1} h_n x_{k-n} \quad (\text{B-1})$$

where,

L : Filter length (order)

y_k : Filter output

x_{k-n} : Filter input

$h_{n=0,\dots,L}$: Filter kernel in time domain (frequency response in frequency domain)

The filter kernel describes how a filter will shape an input signal to create the desired output signal. It defines if a filter is low pass, high pass, and/or bandpass. Since a bandpass filter is the one selected to be designed, the definition of the bandpass filter is the one explained here. A bandpass filter is defined as a filter that permits the frequency band of interest to pass while attenuating the signals at other frequencies. The basic structure of a bandpass filter is illustrated in Figure B-1.

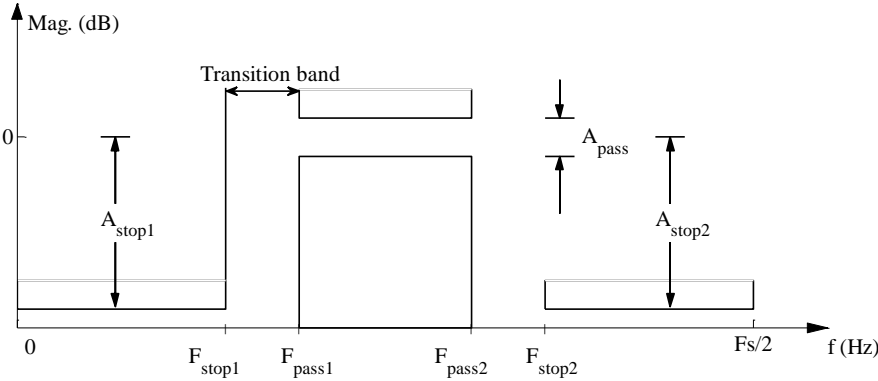


Figure B-1: Basic structure of a bandpass filter

where in Figure B-1,

$A_{stop1,2}$: End of the first and second stopband

A_{pass} : Passband ripple

$F_{stop1,2}$: First and second stopband attenuation

$F_{pass1,2}$: The beginning of the first and second passband

F_s : Sampling frequency

An ideal passband filter in frequency domain should have the following parameters (Smith 1999):

- 1- Minimize transition band (fast roll-off)
- 2- Minimize passband ripple
- 3- Minimize filter order (good stopband attenuation)

You can compare bad and good filter parameters in Figure B-2. However, the ideal filter is a trade-off between all of these parameters. The passband ripple for the available data in this thesis is assumed as 0.1 dB and the transition band is assumed as 0.05 Hz. The filter order is defined empirically by trial and error for the available data set. For example, in the order of 900-1600 yields for the minimum RMS value in the noise reduction of the superconductive x angular acceleration. Results regarding the bandpass filtering will be given in the next sub-section.

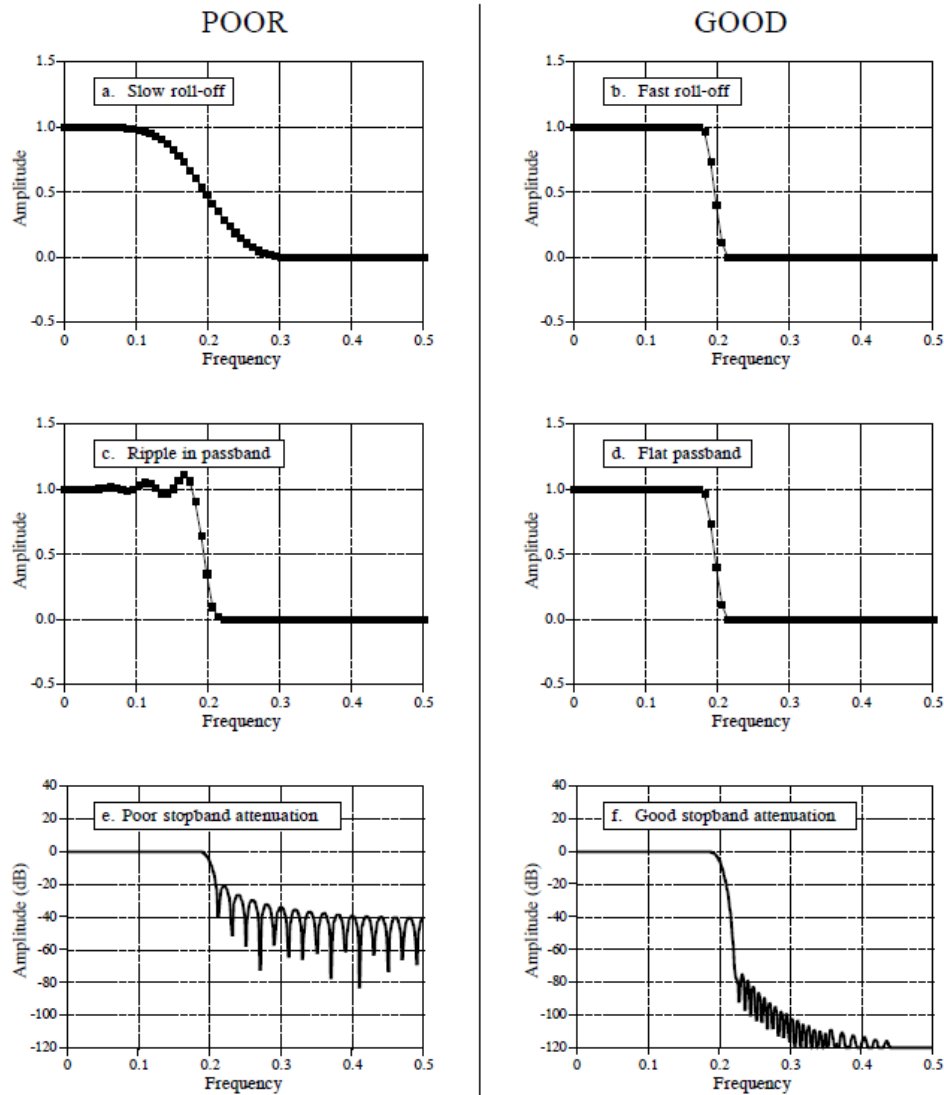


Figure B-2: Frequency responses of a low pass filter showing good and poor filter parameters (Smith 1999)

There are two common approaches in literature to build a filter with good stopband attenuation: adding window functions to the filters and adding a minimum least-squares criterion to the filter design procedures. There are a number of complicated filter design constraints and techniques which interested readers are suggested to see in Parks and McClellna (1972) and Skaloud (1999). The results regarding the two popular FIR filter designs are given in the next sub-sections.

B. 1. 1 Bandpass filtering of x angular acceleration using window design functions

In window design methodology, an ideal filter kernel is multiplied by a predefined window in order to truncate smoothly from the filter’s coefficients. An ideal window is designed as a trade-off between main lobe width and side lobe amplitude. A smoother window has decreased side lobes with increased main lobe width, which makes the filter have small oscillatory parts in both passband and stopband. Bartlett, Hann, Hamming, and Blackman are four popular window functions used in digital filtering, which are applied to the x angular acceleration in this section.

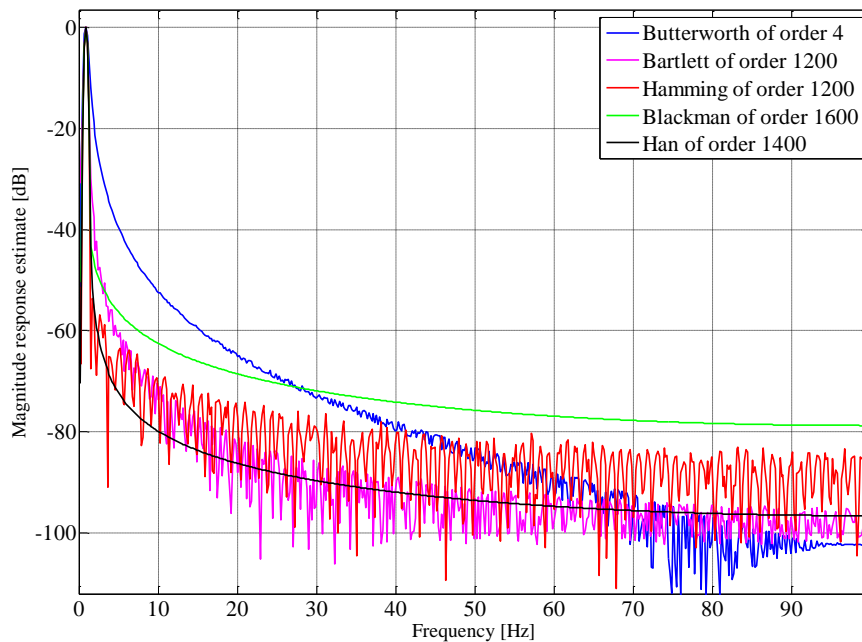


Figure B-3: Frequency response of an FIR bandpass filter with four popular windowing functions in comparison to the frequency response of an IIR Butterworth bandpass filter

Figure B-3 shows the frequency response of the four popular windowing functions in comparison to the frequency response of an IIR Butterworth bandpass filter. The mathematical derivations of all these window functions is presented in Oppenheim and Schaffer (1989). Therefore, they are not repeated here.

The filter order of 10 to 2000 has been selected for the FIR bandpass filter. However, Table B-1 shows only the results with the minimum RMS values achieved for the filtered x angular acceleration. The reason for selecting the order of 4 for the IIR Butterworth bandpass filtering is that this order corresponds to the Butterworth low pass filtering that Gedex has applied to the data.

Table B-1: Comparison of bandpass FIR filtering methods, bandpass IIR filtering, and wavelet de-trending and de-noising applied to the x angular acceleration (Bandpass of interest is 0.53-1.01 Hz)

Filter name	Filter type	Filter order	RMS (rad/s^2)	Improvement w.r.t original signal (%)
Wavelet de-trending & de-noising	-	-	3.08e-05	99.44
Butterworth	IIR	4	5.42e-05	99.01
Bartlett	FIR	1200	3.78e-05	99.31
Blackman	FIR	1600	3.74e-05	99.31
Hamming	FIR	1200	3.73e-05	99.31
Han	FIR	1400	3.70e-05	99.32

It is obvious from Table B-1 that still the results of the wavelet de-trending and de-noising creates more improvement in reducing the noise level. The IIR Butterworth bandpass filtering creates the worst result.

PSD of the raw and filtered x angular acceleration after applying the wavelet, Butterworth, and Bartlett methods is depicted in Figure B-4, and the PSD of the raw and the filtered x angular acceleration after applying the Blackman, Hamming, and Han methods is depicted in Figure B-5.

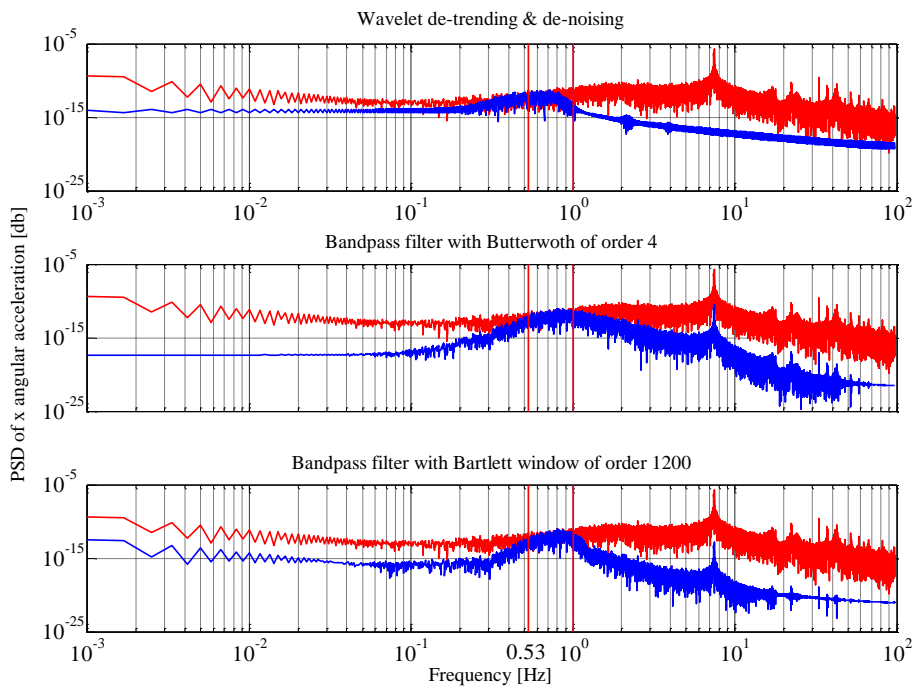


Figure B-4: PSDs of the raw and filtered x angular acceleration after wavelet, Butterworth, and Bartlett filtering methods

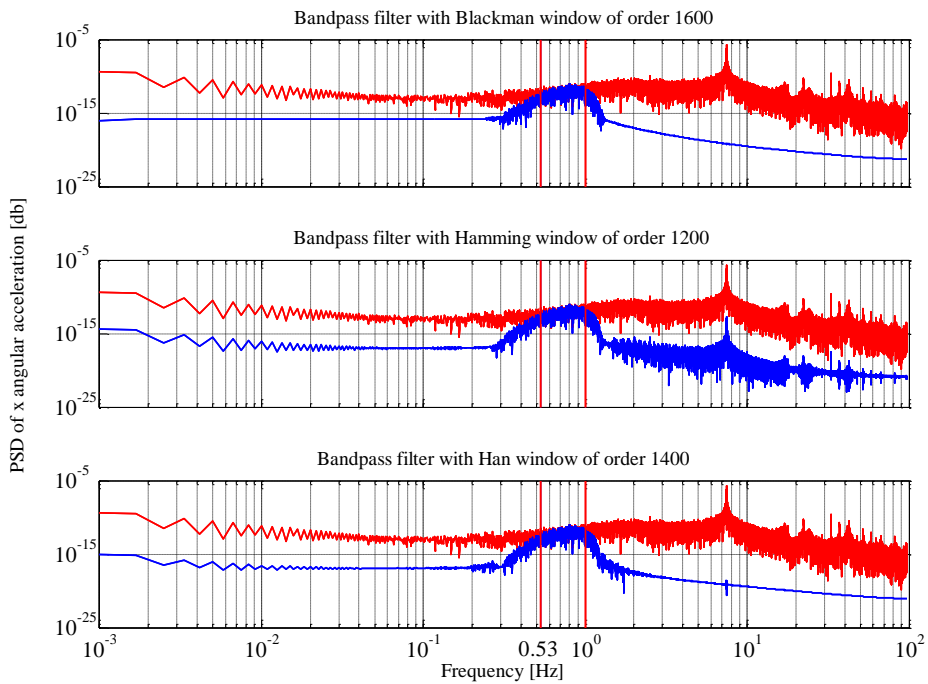


Figure B-5: PSDs of the raw and filtered x angular acceleration after Blackman, Hamming, and Han filtering methods

B. 1. 2 Bandpass filtering of x angular acceleration using minimum least-squares error criterion

Using the windowing design methods in FIR filtering will not create an optimal result. Therefore, an optimal FIR filter is highly recommended. One way to build the optimal FIR filter is by adding the minimum least-squares criterion to the filter design procedure. The squared error that is going to be minimized is defined as (Selesnick 2013):

$$\varepsilon = \int_0^{\pi} W(\omega)(A(\omega) - D(\omega))^2 d\omega \quad (\text{B-2})$$

where,

$A(\omega)$: The actual amplitude response

$D(\omega)$: The ideal amplitude response

$W(\omega)$: The non-negative weighting function

The solution of the defined equation is written in terms of a linear system of equations, which the mathematical expressions can be found in many references such as Selesnick (2013) and Karam et al., (1999) therefore they are not shown here. The weighting function is used to put more or less emphasis on minimizing the integral squared error in certain parts of the frequency response.

Table B-2: The RMS values achieved for the x angular acceleration after applying the least-squared bandpass filtering of order 900

First and second stopband weight	RMS (rad/s^2)	Improvement w.r.t original signal (%)
1	4.57e-05	99.16
10	4.10e-05	99.25
20	4.02e-05	99.26
30	3.96e-05	99.27
40	3.90e-05	99.29
50	3.84e-05	99.30
70	3.73e-05	99.32
90	3.62e-05	99.34
100	3.57e-05	99.35
150	3.35e-05	99.39

A least-squares FIR filter of order 900 with different stopband weights and passband weight of 1 is applied to the x angular acceleration. A filter order of 900 yields the minimum RMS values in comparison to the filter orders from 10 to 1500. That is why the results related to the order of 900 is shown in Table B-2. One can compare the frequency responses of the worst and best the bandpass least-squares filter in Figure B-6. In the worst case both bandpass and stopband weights are assumed 1 while for the best case result the passband weight is assumed 1 and the stopband weight is 150. The green plot in Figure B-6 shows a good stopband attenuation in comparison to the blue plot. Additionally, the PSDs of the best and worst results are depicted in Figure B-7.

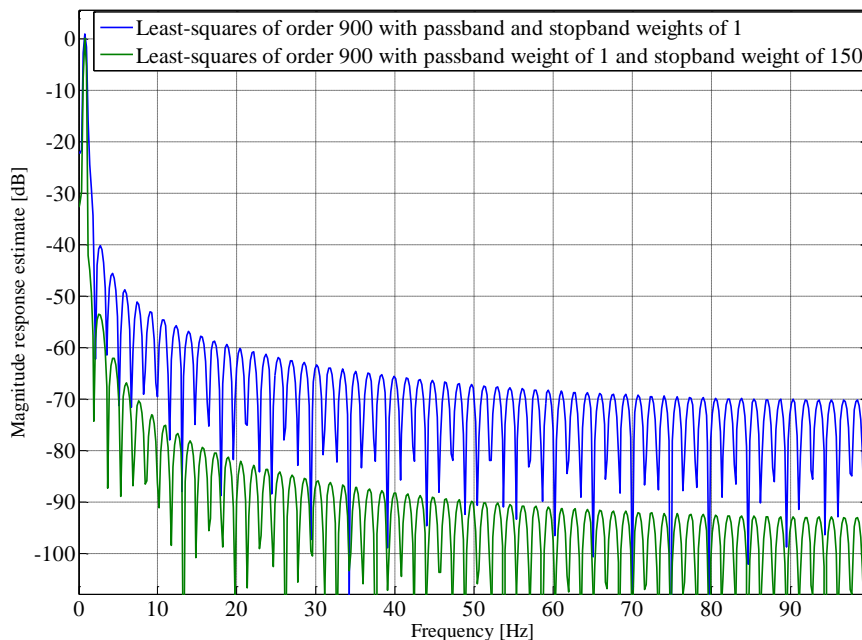


Figure B-6: Worst (blue line) and best (green line) frequency responses of the bandpass least-squares

The best result achieved in least-squares method (shown in blue in Table B-2) shows some improvement in reducing the noise level in comparison to the window bandpass filtering results. However, the wavelet de-trending and de-noising still shows the minimum RMS value for the noise reduction. It seems that designing an optimum bandpass digital filtering is not an easy task; however, its implementation is much simpler than wavelet de-trending and de-noising technique.

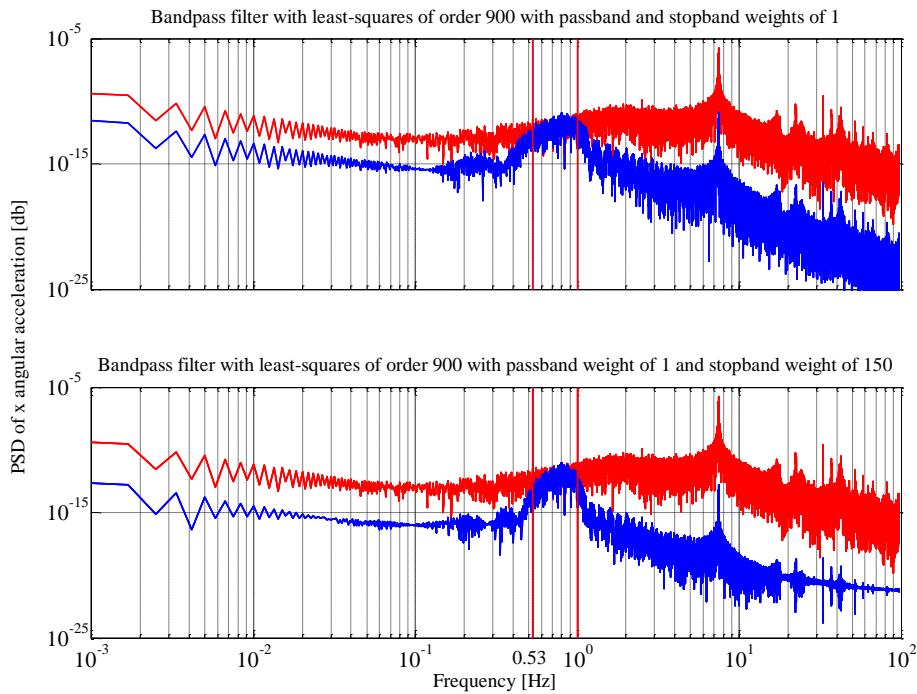


Figure B-7: PSDs of the best case (bottom plot) and worst case (top plot) results for the least-squares bandpass filtering

Even though the performance of the best bandpass filter is marginally (i.e., 0.05%) worse than that of the best wavelet, it is worth mentioning that it was only tested with the static data and the noise structure may well change under dynamic conditions. In such a scenario the stopband may contain more noise than in the static case, but with bandpass filtering this would have no residual effect (i.e., all noise in stopband would be suppressed).